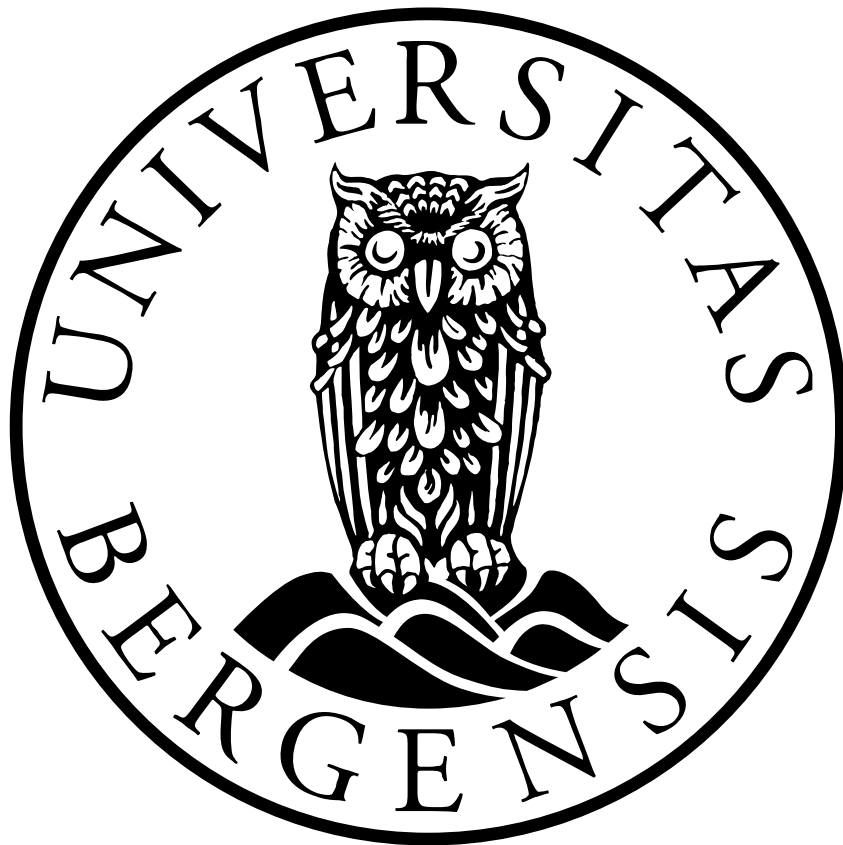# Influence of fault geometry on seismic registrations

MASTER THESIS

BASIN AND RESERVOIR STUDIES

Olea Synnøve Hofshagen

UNIVERSITY OF BERGEN

DEPARTMENT OF EARTH SCIENCE

June, 2019

Abstract

One of the main objectives of seismic interpretation is the identification and positioning of structural discontinuities, e.g. faults, fractures, pinch-outs and karsts. Seismic diffractions encode the seismic response from such small-scale events and may thus provide valuable information about the geometry of structural discontinuities which are small compared to the seismic wavelength. As such, this information may lead to seismic super-resolution, i.e. recovery of sub-wavelength size details. Despite the many advantages of utilising the diffracted wavefield, seismic diffractions are typically considered as noise and are intentionally suppressed during conventional seismic processing. If we could utilise the properties of diffracted seismic waves for the estimation of the velocity model, seismic imaging will have a potential for improvement. In order to carry out such a process, a reliable method for detecting diffractions is essential. In this study, a method for detecting diffracted waves on pre-stack offset gathers, using a diffraction detection algorithm, is proposed. This algorithm is tested on synthetic and real seismic data, processed in the pre-stack domain. To facilitate diffraction detection, a reflection focusing technique is applied to separate diffractions from specular reflections. The novelty of my approach is to incorporate semblance calculations as a quantitative measure of detection capability. Here I show that by generating semblance plots and comparing them to pre-stack depth migrated sections - where regions where diffractions are likely to occur are identified – I am able to quantify the extent of diffraction detectability. Furthermore, the results demonstrate how the diffraction detection algorithm successfully detects diffractions, despite variations in seismic velocities and amounts of coherent and incoherent noise. Consequently, the findings of this study may be of importance in the process of recovering structural details smaller than the seismic wavelength, which could significantly assist seismic interpreters and lead to major geological discoveries.

Acknowledgements

Olea Synnøve Hofshagen

Olea Synnøve Hofshagen

Bergen, June 2019

Contents

1 Introduction

Identifying and positioning small-scale geological structures in seismic exploration is crucial when performing seismic interpretation, as these may strongly affect reservoir flow properties (Moser & Howard, 2008). Discontinuities, e.g. faults, are in conventional seismic processing identified by using the reflected wavefield to interpret reflector displacements, as fault planes are generally poor reflectors. This method is usually successful, as reflected waves carry most of the information about the subsurface. Reflection imaging is however limited by the seismic resolution and may not resolve displacements comparable to the seismic wavelength. The reliability of interpreting discontinuities by using reflection imaging is thus limited, as no definite answers can be given as to location, geometry and connectivity of scattering objects below the *Rayleigh limit* (Iacopini et al., 2016); a criterion defining the minimum size of resolvable details. However, seismic diffractions are increasingly gaining attention (Landa, 2012), as they encode the seismic response from small-scale subsurface events such as faults, fractures, pinch-outs and karsts, in general small-size scattering objects which are small compared to the seismic wavelength (Khaidukov et al., 2004; Moser & Howard, 2008). Diffractions are controlled by the impedance contrasts between e.g. the fault zone content and the surrounding beds, and not by the magnitude of fault displacement, theoretically implying that we can identify faults and fractures with zero displacements by studying the diffracted wavefield (Moser & Howard, 2008). As a consequence, diffracted waves are of great interest and may be used as a reliable source of information about the geometry of structural discontinuities in the subsurface, even when fault displacements are low (e.g. Landa et al., 1987; Belfer et al., 1998; Moser & Howard, 2008).

The significance of diffracted waves has been recognised for many years (Krey, 1952; Hagedoorn, 1954; Kunz, 1960). However, despite the many advantages of utilising the diffracted wavefield, it is not routinely used in interpretation and are generally viewed upon as noise in conventional processing (e.g. Belfer et al., 1998; Bansal & Imhof, 2005; Moser & Howard, 2008; Ogiesoba & Klokov, 2016). Khaidukov et al. (2004) even go as far as claiming that diffractions are the "abandoned stepchildren" of traditional seismic processing and imaging, and that the value of these waves should not be underestimated. In conventional processing, the diffraction events are attenuated and smoothed out during migration, thus they are best studied and analysed prior to migration, in the pre-stack domain (Khaidukov et al., 2004).

The quality of seismic images is highly dependent on the associated seismic velocity model. This model has to be known prior to seismic imaging. Moreover, seismic imaging is inherently utilising the properties of reflected as well as diffracted waves. However, in the process of estimating the velocity model it is common to use, with few exceptions, only observations of reflected waves. If we could also utilise diffracted waves in this process, seismic imaging will have a potential for improvement. Seismic diffraction energy is typically weak compared to reflection energy and also to noise of different kinds, making diffraction analysis a challenging process. Consequently, if our intention is to use diffractions explicitly for estimating the velocity model, it will be of high importance to have available a robust procedure for detecting and verifying diffraction events in the recorded seismic. The main objective of this thesis is thus to provide such a procedure.

Previous work has found that diffraction detection is made possible by separating diffraction energy from specular reflections. This process becomes essential due to the normally low level of the seismic diffraction energy. The idea of separating diffractions from reflections before analysis was suggested by Harlan et al. (1984) and later studied by a variety of authors (e.g. Khaidukov et al., 2004; Landa et al., 2008). Different techniques have been researched in order to achieve separation, e.g. the plane-wave destruction method (e.g. Fomel, 2002; Taner et al., 2006; Klokov et al., 2012; Decker & Klokov, 2014; Ogiesoba & Klokov, 2016) and reflection focusing (Khaidukov et al., 2004; Moser & Howard, 2008). The latter technique is followed in this study. The novelty of my approach is to incorporate semblance calculations (e.g. Taner & Koehler, 1969; Fomel, 2009) as a quantitative measure of detection capability.

The main objective of this thesis is threefold: 1) Use seismic images in the pre-stack domain, processed in time or depth, to identify regions where diffractions are likely to occur, e.g. in fault zones, for layers terminating toward salt bodies and in other cases where layers terminate (e.g. pinch-outs). 2) Simulate diffracted waves from such regions. 3) Quantify the extent to which one finds consistency with recorded seismic data. Synthetic data generated from the Gullfaks Field (northern North Sea) and real seismic data from the Frøya High (mid-Norwegian continental margin) are used in the steps above. Both the synthetic and real seismic data depicts numerous normal faults, where diffracted energy is expected to be found.

2   Geological framework

This MSc thesis concerns the study of both synthetic and real seismic data, acquired from the Norwegian continental margin, more specifically from the Gullfaks field in the northern North Sea and from the Frøya High on the mid-Norwegian continental margin (Figure 2.1). In order to better understand the origin of the fault zones subject to this diffraction detection study, a review of the study areas and the regional tectonic environment of the Norwegian continental margin is provided.

2.1   Study area

The Norwegian continental margin (55° - 81°N) is characterised as a rifted passive continental margin which encompasses three main provinces; the North Sea, the mid-Norwegian continental margin and the Western Barents Sea (Faleide et al., 2010).

The synthetic seismic dataset is generated from a 3D model from the Gullfaks field, located on the western flank of the Viking Graben in the northern North Sea. The Gullfaks field covers the eastern half of a 10-25 km wide NNE-SSW-trending fault block, named the Gullfaks fault block, which is only one of many large faults blocks across the North Sea (Fossen & Hesthammer, 1998). Three structurally contrasting segments make up the field. The western segment comprises a domino-style, rotated fault block geometry with N-S striking normal faults (Figure 2.2), while the eastern segment forms a deeply eroded horst complex of steep faults and elevated sub-horizontal layers (e.g. Petterson et al., 1990; Fossen & Hesthammer, 1998). These segments are divided by a third segment; a complex accommodation zone, characterised by folding structures.
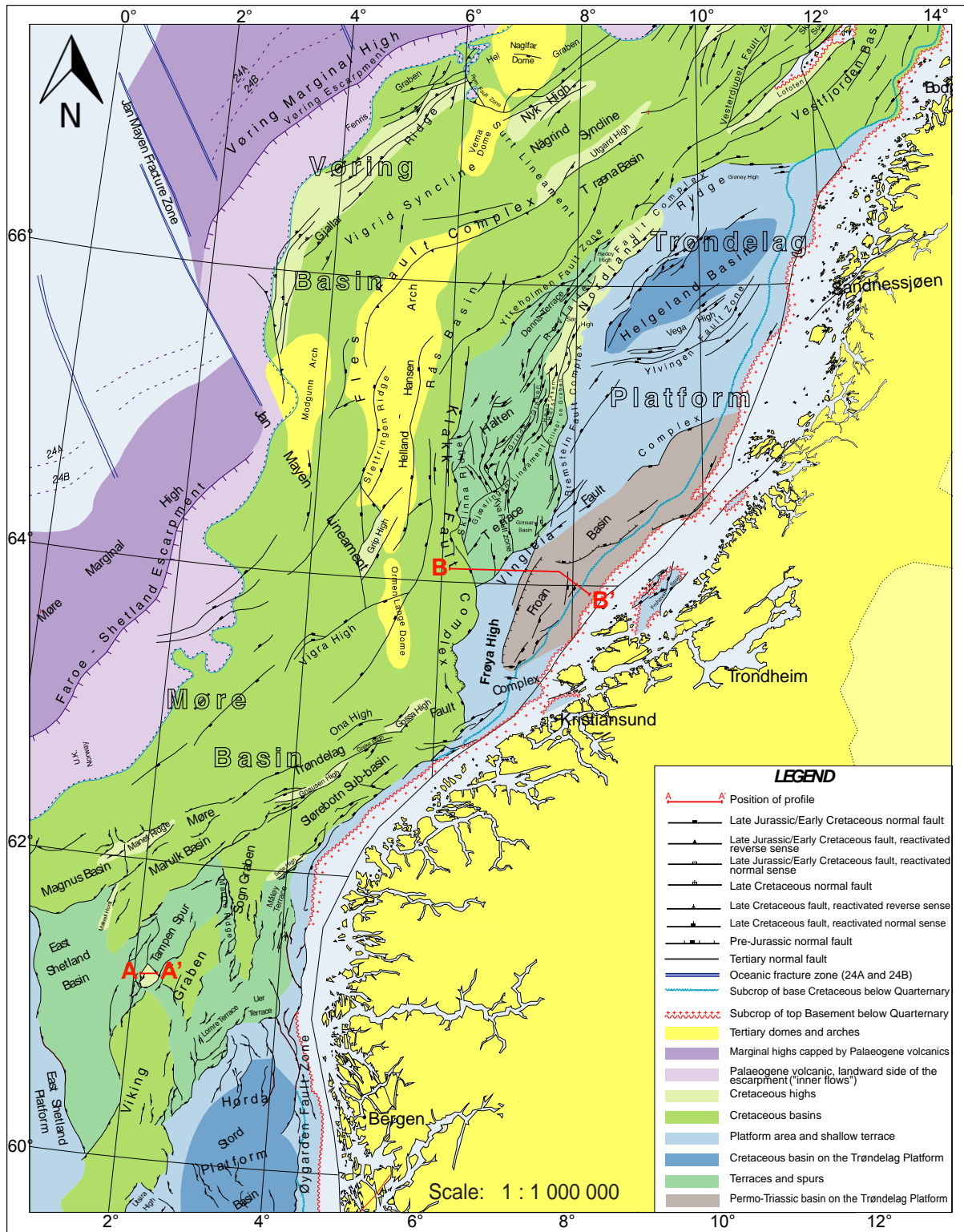
Figure 2.1: Main structural elements of the northern North Sea and the mid-Norwegian continental shelf. The synthetic seismic dataset is acquired from the Gullfaks field, marked by profile A-A' (Figure 2.2). The real seismic profile (MB-23-84) that is used throughout this thesis is acquired from the Frøya High, marked in bold slightly south of profile B-B' (Figure 2.3). Modified after Brekke et al. (1995).
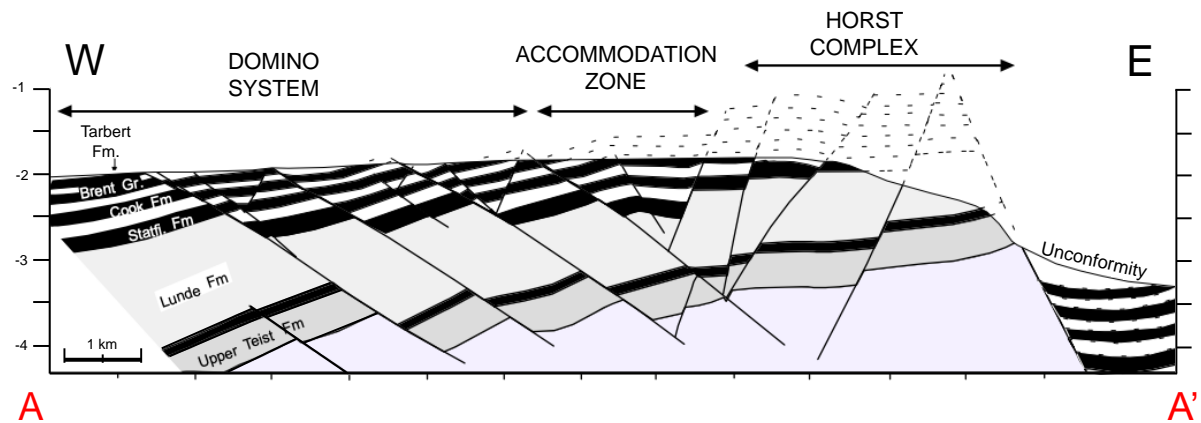
Figure 2.2: Structural cross section of the Gullfaks Field. A deeply eroded horst complex in east is divided from a domino-area in west by an accommodation zone. Slightly modified after Agustsson et al. (1999).

The real synthetic dataset is acquired on the mid-Norwegian continental margin, more specifically in the south westernmost part of the Trøndelag platform, referred to as the Frøya High. The Frøya High, as first defined by Gabrielsen et al. (1984), is an offshore area extending between 63°N - 64° 30'N and 6°30'E - 7°20'E, about 50 kilometres west for the island of Frøya on the coast of Sør-Trøndelag (Figure 2.1). The high outlines a N-S oriented horst about 30-40 km wide and 120 km long, of which the summit is a flat, smooth, composite Late Jurassic-Early Cretaceous unconformity surface dipping gently towards WNW (Figure 2.3) (Blystad et al., 1995). The horst structure is bounded by the Klakk and Vingleia fault complexes in southwest and northwest respectively (Blystad et al., 1995; Brekke, 2000), separating the high from the Cretaceous Møre basin in southwest and the Halten Terrace in northwest. The eastern flank of horst is the boundary fault of the adjacent Froan Basin.
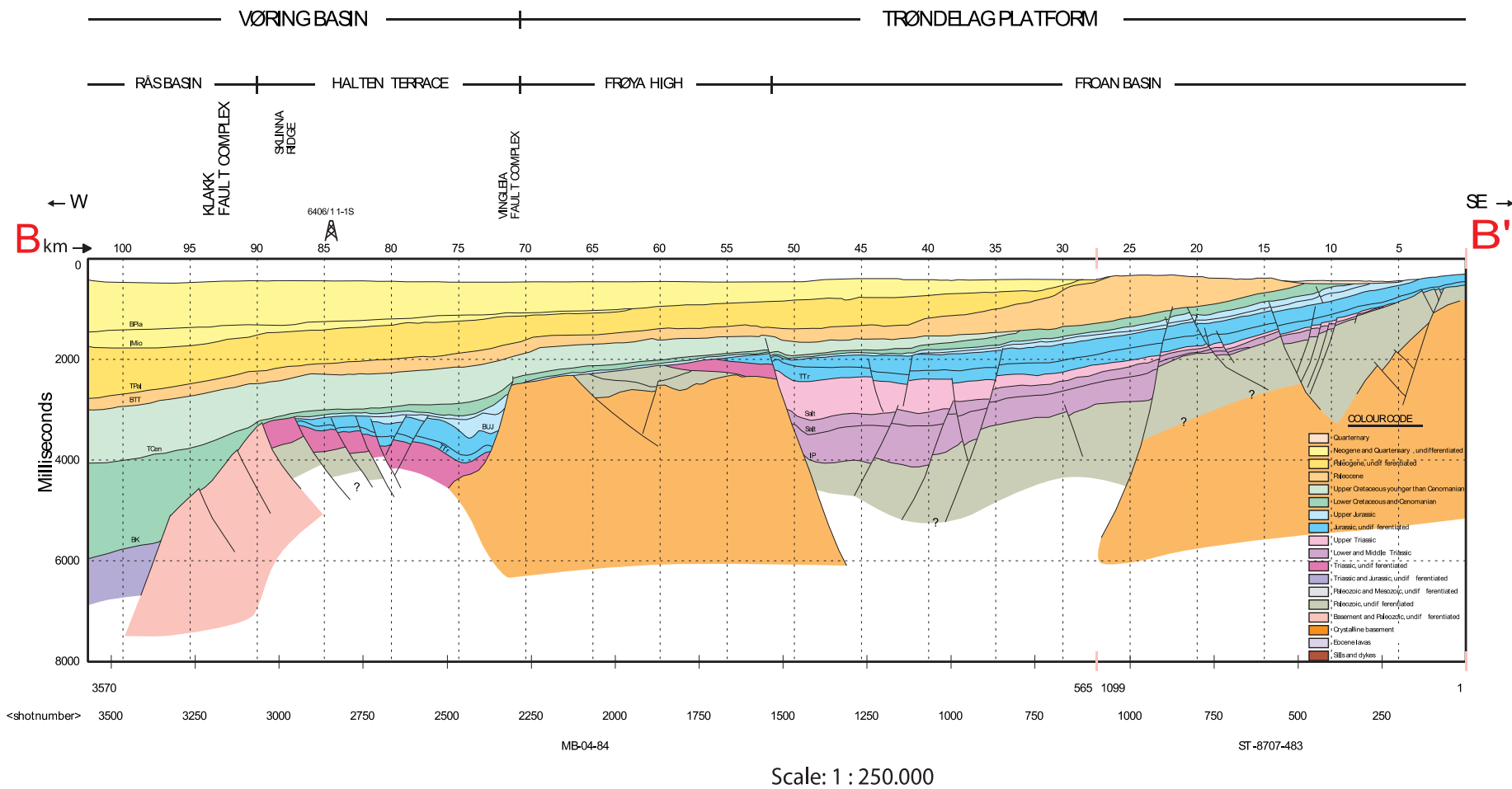
Figure 2.3: Cross section illustrating the Vøring Basin and Trøndelag Platform. The Frøya High is positioned in the centre. The summit of the high is a Late Jurassic-Early Cretaceous unconformity surface dipping towards WNW, bound by the Vingleia Fault Complex in southwest (Blystad et al., 1995). Slightly modified after Blystad et al. (1995).

2.2   Regional tectonic development

The Norwegian continental margin (55° - 81°N) has been subject to a long and complex tectonic history. Its structural configuration is a product of multiple episodes dating back to the closure of the Iapetus Ocean with the culmination of the Caledonian orogeny in the Late Silurian – Early Devonian, followed by Early Devonian extensional collapse of the orogen (e.g. Pitman & Talwani, 1972; Gabrielsen et al., 1984; Braathen et al., 2000; Skilbrei et al., 2002; Marsh et al., 2010). This episode was succeeded by numerous extensional deformation episodes throughout Mesozoic–Cenozoic times, which culminated with the progressive northward opening of the North Atlantic Ocean at the Palaeocene-Eocene transition (e.g. Pitman & Talwani, 1972; Doré et al., 1999; Marsh et al., 2010).

Despite some differences during Cretaceous–Cenozoic times, there are many similarities in the tectonic development of the North Sea and the mid-Norwegian continental margin (Faleide et al., 2010). Multiple regional extensional events have influenced the structural development of the continental margin and reactivated basement structures from the Caledonian Orogeny (e.g. Blystad et al., 1995; Doré et al., 1997; Brekke, 2000; Marsh et al., 2010). This includes: Early to Middle Devonian, Carboniferous, Late Permian to Early Triassic, late Middle Jurassic to Early Cretaceous and finally Late Cretaceous to Early Eocene.

Early to Middle Devonian

The closure of the Iapetus Ocean and the subsequent Silurian-Devonian collision between Laurentia and Baltica gave rise to the Scandinavian Caledonides (e.g. Bukovics & Ziegler, 1985; Braathen et al., 2000). Orogen-parallel extensional movement of the hinterland initiated in the Early Devonian as a consequence of gravitational collapse of the orogen (e.g. Skilbrei et al., 2002). Thus, the tectonic regime altered from being a compressional to an extensional system. Major sinistral movements gave rise to crustal thinning and rapid subsidence, accompanied by extensive intrusive and extrusive igneous activity along the western coast of Norway (Ziegler, 1989; Gabrielsen et al., 1999).

Carboniferous

The region of the present North Atlantic was in Early Carboniferous through Late Permian times part of the Pangean supercontinent (e.g. Brekke et al., 2001). Regional crustal extension

related to continental rifting persisted through the Carboniferous, resulting in a central rift system between present-day Greenland and Norway. The rift system was dominated by N-S to NE-SW-trending normal faults in addition to NW-SE-trending transfer faults (Gabrielsen et al., 1999; Brekke et al., 2001). A period with intense extensional block faulting occurred in this rift system from late Carboniferous to Early Permian times, which continued into the late Permian with less intensity (Surlyk, 1990). On the mid-Norwegian continental margin, the NE-SW-trending structural trend differs from a transverse NW-SE trend that probably reflects Precambrian lineaments (Brekke, 2000). The tectonic development of the Frøya high throughout the subsequent tectonic phases is controlled by these two structural trends (Brekke, 2000).

Late Permian to Early Triassic

The tectonic assemblage of Pangea was finalised during Permian times, followed by the onset of continental rifting (Brekke et al., 2001). Thus, the Permo-Triassic extensional phase represents the break-up of an uplifted and unstable Pangaea (e.g. Doré et al., 1999). Greenland and Norway were in the Triassic only separated by a 300-500 km wide lowland area, still under the impact of regional crustal extensional forces (Ramberg et al., 2013). Major rotated fault blocks with a general N-S to NNE-SSW trend originated in this phase, reflecting an E-W extension direction across the continental rift (Fossen & Hesthammer, 1998). These blocks initiated a complicated horst and half-graben system on the Norwegian margin (Brekke, 2000), establishing e.g. the Viking Graben in the northern North Sea (Fossen & Rørnes, 1996).

Latest Permian throughout Triassic times are characterised by fluctuations in marine sea level, with alternating transgressive and regressive periods. Evaporite intervals on the mid-Norwegian margin that were deposited during regressive periods under a fluvial sabkha environment, make up detachments levels for later extensional faulting (Halland et al., 2014).

Late Middle Jurassic to Early Cretaceous

Another tectonic period initiated in the Middle Jurassic and culminated in the Early Cretaceous, accompanied by upper crustal thinning, extension and normal faulting, (e.g. Halland et al., 2014). This event is associated with a northward propagation of the North East Atlantic. Crustal thinning induced high heat flow and the growth of a volcanic dome in the North Sea, centred between the Viking Graben, the Central Graben and the Moray Firth Basin

(Halland et al., 2014). The high heat flow caused tilting, uplift and erosion across the margin. The structural formation of the Gullfaks field originated during this period, resulting in a prominent N-S oriented fault system and block rotation in the western part of the structure, while the eastern part remained elevated as a horst structure (Petterson et al., 1990). At the same time, oscillating levels of alluvial plain sandstone and organic rich mudstone were deposited on the shelf as a result of the fluctuating sea level, high temperatures and high biological production (Ramberg et al., 2013).

On the mid-Norwegian continental margin, the accumulation of Jurassic deposits was accompanied by tensional faulting, leading to fault block rotations and reactivation of older faults in the Vingleia Fault Complex (Bukovics & Ziegler, 1985; Brekke, 2000). Uplift of the Frøya High and Nordland ridge initiated during this rifting episode, complemented by tilting and erosion (Blystad et al., 1995; Brekke, 2000). Crustal extension and thinning led to the development of major Cretaceous basins, such as the Møre and Vøring basins, which underwent rapid differential subsidence and segmentation into sub-basins and highs (Gabrielsen et al., 1984; Faleide et al., 2008). These tectonic events led to an accentuation of the horst and half-graben system that initiated in Triassic, now transforming into a complicated system of deep basins to the west and tectonic highs to the east (Brekke et al., 2001).

Late Cretaceous to Early Eocene
Following a period of oscillating sea level in the Jurassic and early Cretaceous, regional transgression initiated in the Aptian and persisted into the Late Cretaceous, resulting in an exceptionally thick basin fill of carbonates in large areas on the Norwegian margin (e.g. Brekke, 2000; Brekke et al., 2001). The Late Cretaceous to Pliocene rift phase is related to relative movements along plate boundaries (Brekke, 2000) prior to the opening of the North Atlantic and the onset of continental break-up. The effects of this extensional pulse are best observed in the Norwegian Sea, which includes faulting, regional uplift, accelerated basin subsidence and basinward tilting of the platform areas (Brekke et al., 2001).

Prior to continental break-up, Paleocene extension with upwelling of mantle material underneath the spreading ridges generated widespread uplift, erosion, and intrusion activity in areas up to 900-1000 km away from the spreading ridges, compromising the Trøndelag Platform and surrounding mainland (Doré et al., 1999; Brekke, 2000). Igneous sills intruded

the thick organic-rich Cretaceous deposits in the Møre and Vøring basins, leading to an explosion of greenhouse gases into the atmosphere (Faleide et al., 2008). These events culminated with the continental break-up, separating Greenland from Eurasia, at the Paleocene/Eocene transition at approximately 56 Ma. The northern North Sea, including the Gullfaks fault block, underwent extremely rapid subsidence in Early Eocene times, explained by Nadin and Kusznir (1995) as a consequence of cold asthenosphere diverting back from the distal parts of the uplifted regions. This led to a rapid decrease in the dynamic uplift away from the centre of the plume (Nadin & Kusznir, 1995; Brekke, 2000).

The opening of the North Atlantic Ocean at the Palaeocene-Eocene transition marked the culmination of an approximately 340 Ma history of extensional deformation and sedimentary basin formation on the Norwegian continental margin, that initiated with the extensional collapse of the Caledonian orogen in the Late Silurian to Devonian time (e.g. Doré et al., 1999; Braathen et al., 2002; Skilbrei et al., 2002; Marsh et al., 2010).

3 Theoretical background

To facilitate the discussion in forthcoming chapters, the principles concerning reflection and diffraction theory, seismic noise and resolution as well as seismic acquisition and processing are briefly reviewed in the current chapter. These are topics that are relevant in order to understand the process of diffraction detection. Only marine seismic surveys are reviewed in this thesis.

3.1 Basic seismic reflection theory

Seismic reflection surveying is the most widespread geophysical exploration method today. Air guns towed behind a seismic vessel are used to induce highly pressurised air into the water, which generates a spherical expanding wavefront that travels through the water and into the subsurface until it reaches an interface. When these energy pulses hit a lithological boundary, energy is both transmitted and reflected depending on the acoustic properties of the material on both sides of the discontinuity (Evans, 1997). Parts of this energy are thus reflected towards the acquisition surface, where seismic receivers record the strength of this energy and the time taken for the energy pulse to reach a given reflector and return to the receiver – creating the basis of reflection seismic. This elapsed time is called two-way traveltime (TWT).

In seismology and seismic exploration, compressional (P-) and shear (S-) waves, characterised as body waves (Yilmaz, 2001), are of particular interest as they propagate through the Earth's subsurface. Compressional waves propagate in the direction of wave travel by compression and dilatation, whereas shear waves propagate perpendicular to the direction of wave travel by pure shear strain (Kearey et al., 2002). A further look into density and velocity terms is necessary to understand the controls on acoustic impedance, i.e. the product of seismic velocity and density. Assuming that the waves propagate through an isotropic and homogenous medium, the P- and S-wave velocities are given by

$$V_P = \sqrt{\frac{K + \frac{4}{3}\mu}{\rho}} \qquad\qquad (\text{Eq. } 3.1)$$

and

$$V_S = \sqrt{\frac{\mu}{\rho}} \qquad \text{(Eq. 3.2)}$$

where K is the bulk modulus, ρ is the density and μ the shear modulus. Note that both the P- and S-wave velocities are inversely proportional to density ρ. The lower the rock density, the higher the wave velocity – which is the case for e.g. halite, which has a low density (1.8 gr/cm^3) and high P-wave velocity (4500 m/s) (Yilmaz, 2001). However, an increase in density is usually accompanied by an increase in the ability of the rock to resist compressional and shear stresses – thus resulting in an increase in bulk modulus and modulus of rigidity (Yilmaz, 2001). The shear modulus μ is zero in a liquid, causing V_S to be zero in the water column. As the velocity of the compressional P-wave depends upon the value of the bulk modulus as well as the shear modulus, V_P is not zero in a liquid, and is thus always faster than V_S (Mussett & Khan, 2000).

When an incident compressional wave propagates through media of different velocities, the energy is both transmitted and reflected according to Snell's law:

$$\frac{\sin \theta_1}{V_1} = \frac{\sin \theta_2}{V_2} \qquad \text{(Eq. 3.3)}$$

where V_1 and V_2 are the velocities of the incident and second medium, θ_1 is the angle of incidence and θ_2 is the angle of refraction (Figure 3.1). If the seismic wave is obliquely incident, both reflected and refracted P- and S-waves will be generated at an interface between two media (Mondol, 2010). The energy of the incident ray equals the total energy of the reflected and refracted rays (Kearey et al., 2002).

The reflection coefficient between two velocity layers define the ratio of the amplitude of the reflected wave to the amplitude of the incident ray (Kearey et al., 2002). This coefficient depends on the acoustic impedance, i.e. the product of seismic velocity and density, of the different layers. The reflections coefficient is expressed as

$$R = \frac{\rho_2 v_2 - \rho_1 v_1}{\rho_2 v_2 + \rho_1 v_1} \qquad \text{(Eq. 3.4)}$$

where ρ_1, v_1 and ρ_2, v_2 are the density and P-wave velocity values of the first and second layer respectively.
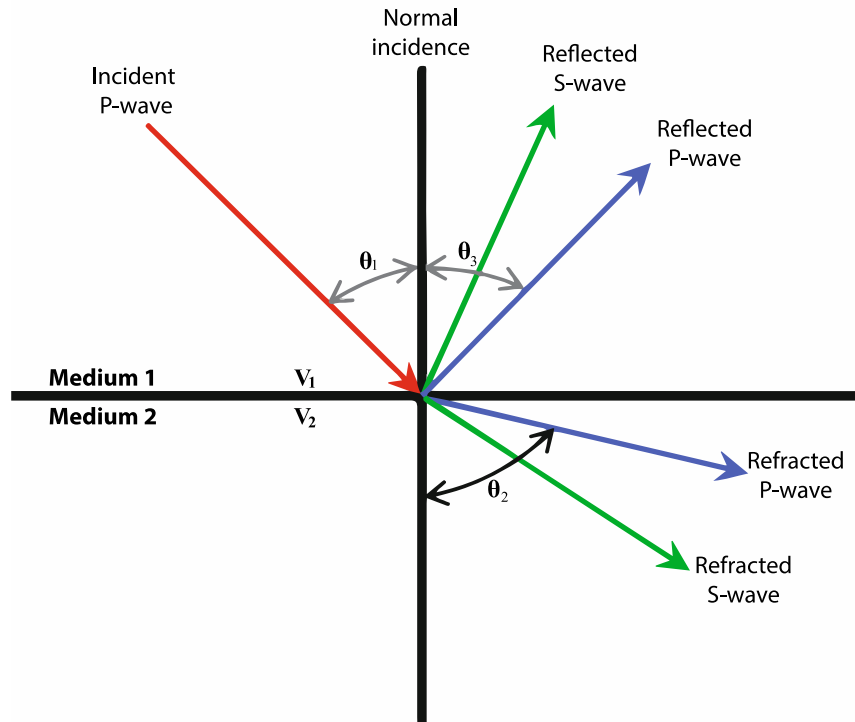
Figure 3.1: Incident P-wave generating reflected and refracted waves. The angle of incidence is represented by θ_1, which is the angle between the incident P-wave and the normal to the interface of two media (represented by Medium 1 and Medium 2). The angle of incidence is equal to the angle of reflection (θ_3) in isotropic media. The angle of refraction, θ_2, depends on the velocity (V_2) in Medium 2. Redrawn after Mondol (2010).

3.2   Seismic noise

Seismic noise is defined as unwanted recorded energy that inferes with the seismic data (Kumar & Ahmed, 2011). In general, we separate seismic noise into two categories: random and coherent noise. One of the main objectives of seismic processing is to separate noise from the seismic signal, in order to enhance the signal-to-noise ratio. Noise attenuation is however a challenging task, considering the various types of noise, and requires different processing sequences in order to efficiently attenuate the unwanted signals.

Random noise is usually caused by effects unconnected with the geophysical survey (Kearey et al., 2002), such as vibrations from wind, tidal waves, rain, production platforms or other boats. Such vibrations are generally characterised by an absence of continuity from one seismic trace to another (Onajite, 2014), a fact that is exploited during the attenuation process. Coherent noise, on the other hand, is often generated by the geophysical survey. We separate between linear- and non-linear coherent noise. Non-linear coherent noise comprises events such as multiples and ghost reflections, while linear coherent noise encompasses diffractions and refractions. Emitted energy from the marine survey sources may be reflected more than

once on its path to the receivers (Telford et al., 1990; Sheriff & Geldart, 1995). This gives rise to multiples (e.g. water bottom multiples; Figure 3.2b), which are false seismic events generated by strong impedance contrasts. We differentiate between short- and long-path multiples, depending on their time delay from the primary events with which they are associated (Onajite, 2014). Long-path multiples, which are further addressed in this study, appear as separate events while short-path multiples arrives shortly after the primary reflections and thus lengthen the wavelet (Sheriff & Geldart, 1995). A ghost reflection (Figure 3.2c) is a short-path multiple that arises when the emitted energy reverberates upward from the shallow position of the source and reflects at the sea surface, subsequently following the similar path of the direct ray towards the receiver. Refractions and diffractions are discussed in section 3.1 and 3.3 respectively.
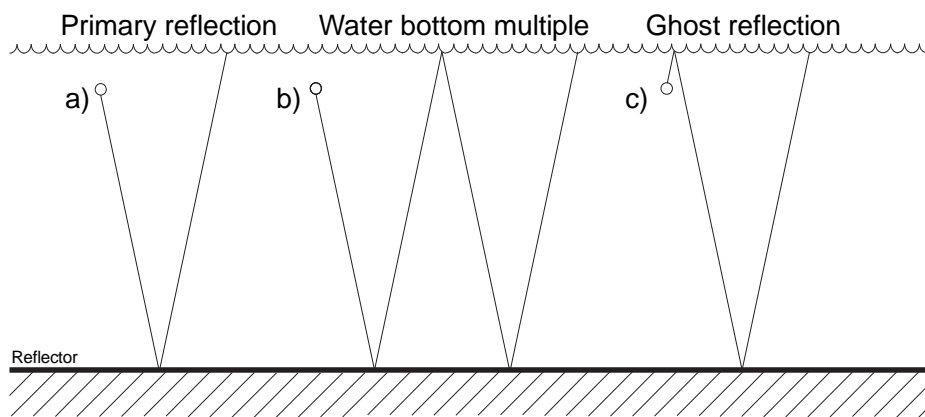
Figure 3.2: Ray paths illustrating possible routes for a) primary reflectors b) water bottom multiples and c) ghost reflectors.

3.3   Diffractions

When discussing reflection and refraction theory, it is assumed that the interfaces between the different media are relatively continuous and planar - which is a mere simplification. As reflectors are often terminated by faults, unconformities, pinch-outs etc., the laws or reflection and refraction are no longer adequate. When a seismic wave hits an interface discontinuity such as a fault surface, it becomes diffracted due to scattering of energy of the propagating wave (Figure 3.3). As mentioned in the introduction, diffractions are controlled by impedance contrasts, and not by the magnitude of fault displacement, theoretically implying that we can identify faults and fractures with zero displacements by studying the diffracted wavefield (Moser & Howard, 2008). The difference between a point reflector and a stepped reflector is presented in Figure 3.4. Figure 3.4b depicts the diffracted response of a stepped reflector, where the crest of the diffraction curve locates the discontinuity if velocity complications are absent (Telford et al., 1990).
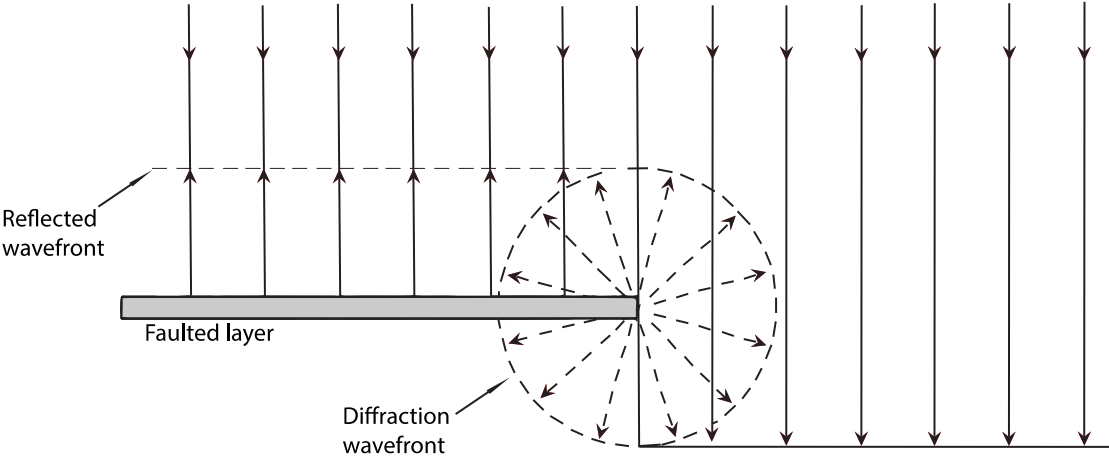
Figure 3.3: Diffracted wavefront caused by the truncated end of a faulted layer. Redrawn after Kearey et al. (2002)
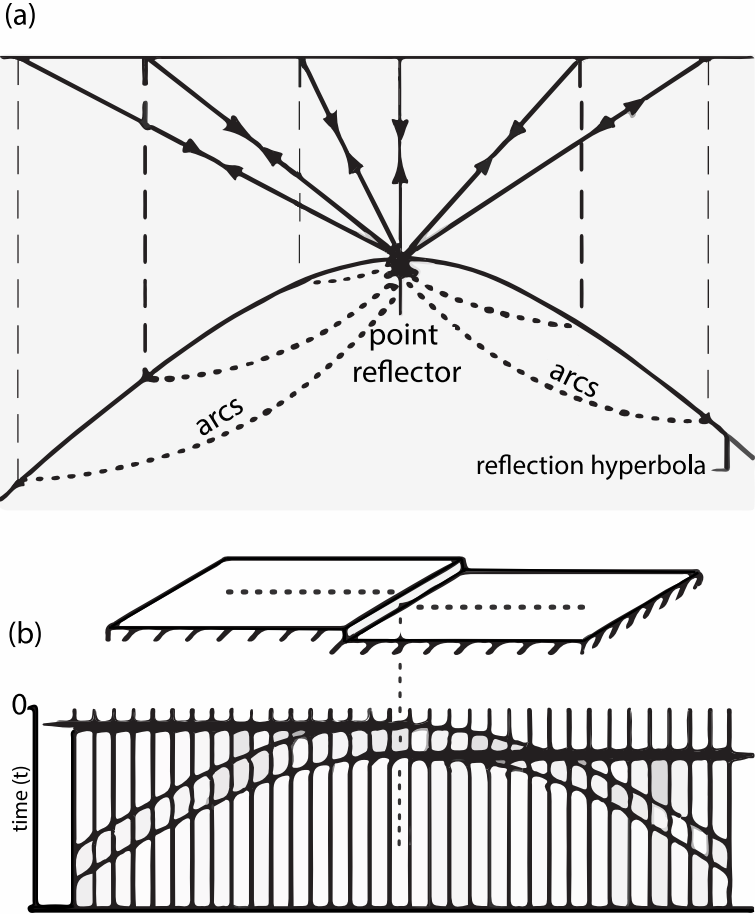
Figure 3.4: a) Reflected waves from a point reflector. b) Stepped reflector resulting in a diffraction hyperbola. Modified after Mussett and Khan (2000).

15

Diffractions are thus the wavefield phenomenon associated with energy that propagates outward from a sharp discontinuity in the subsurface (Yilmaz, 2001). They appear as hyperbolic events on seismic profiles and can be difficult to distinguish from reflected waves as the amplitudes of diffracted waves are much weaker than those of reflections. The amplitude of the hyperbolic events also decreases away from its apex, as a result of increasing distance from the reflector (Mussett & Khan, 2000). The curvature and asymmetry of the diffraction hyperbola depend on velocity variations across the discontinuity (Landa et al., 2008; Bashir et al., 2016a), whereas lateral velocity variations contribute to the generation of asymmetric diffraction hyperbolas and vertical velocity variations affect the slope of the curvatures. Bashir et al. (2015) reviews the effect of vertical velocity variations and demonstrates how diffraction hyperbolas spread out more and have less curvatures with increasing velocities - as a result of increasing depths.

Diffractions and reflections from a discontinuity at the same depth differ in moveout properties. In a case where the source is directly above the diffraction point (Figure 3.5), the diffraction curve has twice the normal moveout of a reflection (Telford et al., 1990). This difference is exploited at a later stage in this study, when trying to separate diffractions from specular reflections.
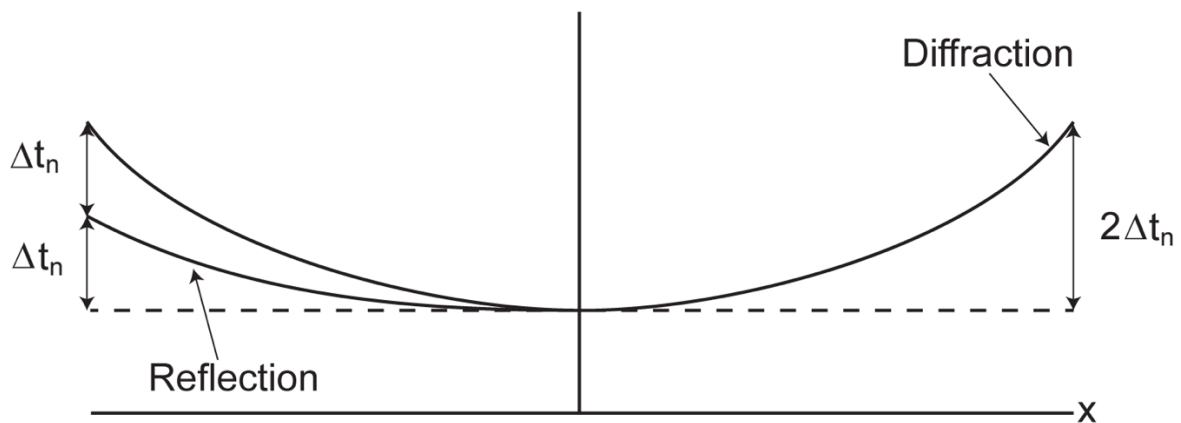
Figure 3.5: Common-source arrivals for diffraction and reflection: Δt_n represents the reflection normal moveout. Redrawn after Sheriff and Geldart (1995).

Diffraction events are usually treated as noise in conventional processing and is subsequently filtered during stacking and migration in a manner that collapses the diffraction events and enhances the reflection events. Hence, diffractions are best analysed and identified in the pre-stack domain, prior to migration.

3.4   Seismic resolution

Seismic resolution is a measure of how close two events can be, yet still be distinguished separately. and becomes an important factor when mapping small structural features such as minor faults. Vertical resolution derives from the dominating wavelength, given by

$$\lambda = \frac{v}{f}$$

(Eq. 3.5)

where v is velocity and f is the dominant frequency. The seismic velocity of the subsea is fixed, but by increasing the temporal frequency and thus reducing the wavelength, one can improve both vertical and horizontal resolution (Lines & Newrick, 2004). However, very short pulses are attenuated more quickly by absorption, so a compromise between resolution and depth of penetration is necessary. Based on the wavelength from the originating source, layers can be detected when their thickness is less than ¼ wavelength, defining the Rayleigh Criterion; $\lambda/4$. The minimum distance between two events that both are visualised is known as the *tuning thickness*. Vertical resolution decreases as a function of depth, as deeper-travelling waves tend to have a lower dominant frequency and higher velocity due to sediment compaction (Kearey et al., 2002). As the resolution is dependent on the wavelength, deep features must be thicker than shallow features in order to be resolvable (Yilmaz, 2001).

Horizontal resolution is described by how close two lateral displaced features can be, while still being distinguishable as two separate points on seismic data. Horizontal resolution is dependent on the Fresnel zone, which Kearey et al. (2002) describes as the part of the interface from which energy is returned to a receiver within half a wavelength of the initial reflected arrival. This implies that events within the Fresnel zone cannot be distinguished as separate events in seismic sections. Consequently, the horizontal resolution is dependent on the temporal frequency and the receiver spacing, in which a decrease in receiver spacing will result in a narrower Fresnel zone width that implies an increase of lateral resolution (Figure 3.6).
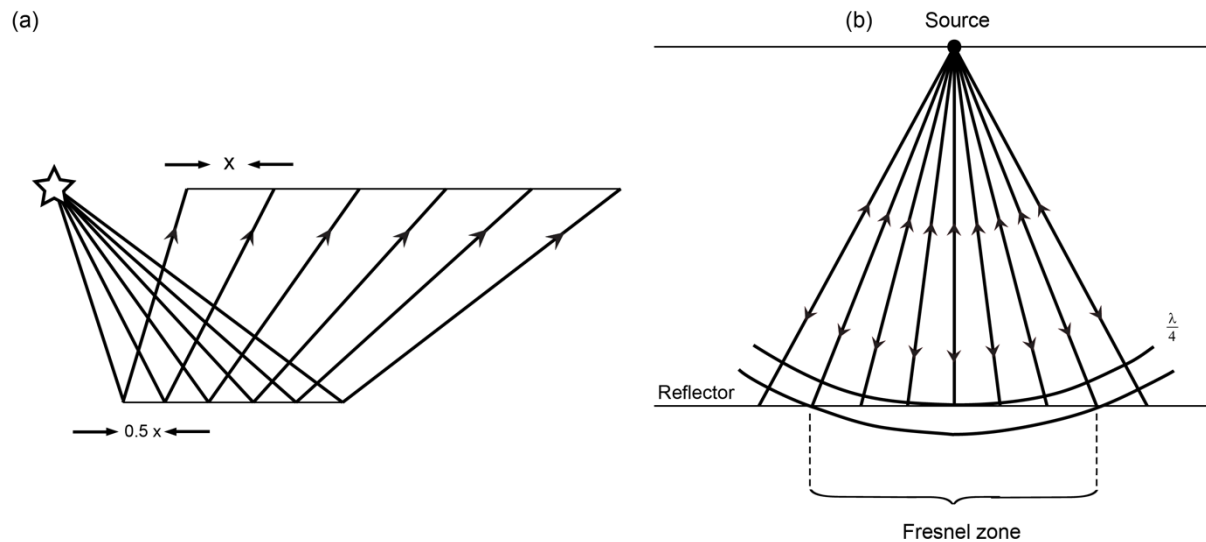
Figure 3.6: a) The horizontal sampling of a seismic reflection survey is half the detector spacing (Kearey et al., 2002). b) Energy from all points of a reflector is returned to the source. The Fresnel zone is defined as the part of the reflector from which energy returns within half a wavelength of the initial reflected arrival. Redrawn after Kearey et al. (2002).

3.5 Marine seismic data acquisition

The aim of seismic exploration is to map geological subsurface structures using reflected seismic waves, e.g. to explore for undiscovered hydrocarbon reserves. This process can be summarised into four essential steps: survey design and planning, seismic acquisition, seismic processing and seismic interpretation. After creating a survey design and performing the acquisition, raw data are obtained and further processed utilising advanced methods within wave-theory and signal processing. This yields an image of the subsurface that represents a vertical slice of a geological model, which is the input for succeeding seismic interpretation. Whether a seismic survey becomes a success or not, is not determinable until the final stage of interpretation, thus it is of great importance that all aspects of the survey are performed correctly the first time (Evans, 1997).

3.5.1 Marine survey sources

The preferred source for generating acoustic energy in the marine realm is the airgun (Figure 3.7 a), a device that discharges pressurised air into the water. Pressures up to 10 000 psi (70 MPa) are used, but the most commonly used pressure is 2000 psi (14 MPa) (Sheriff & Geldart, 1995). An airgun can either be used alone or assembled in an array of air guns of different sizes and are towed behind the seismic vessel, usually at 5-15 metres depth.

When air is released from the chambers of the gun, an acoustic pulse is emitted in the form of a high-pressure bubble which transmits through the water. This effect is described by the bubble effect. If the gas bubble pressure exceeds the surrounding hydrostatic pressure, the net force accelerates the water outward (Sheriff & Geldart, 1995). After the collapse of the initial bubble, oscillatory expansion and collapsing of secondary gas bubbles causes a bubble pulse that increases the length of the seismic pulse (Kearey et al., 2002). The high pressure associated with each bubble collapse will generate seismic waves, and the cycle eventually breaks when the bubble emerges through the surface of the water. As a result of the bubble effect, the waveform emitted by a single air gun oscillates (Figure 3.7b). By operating multiple air guns with different chamber volumes, their initial impulses interfere constructively, while their subsequent bubble pulses interfere destructively (Sheriff & Geldart, 1995). This increases the amplitude of the generated pulse while reducing the bubble pulse (Figure 3.7c).
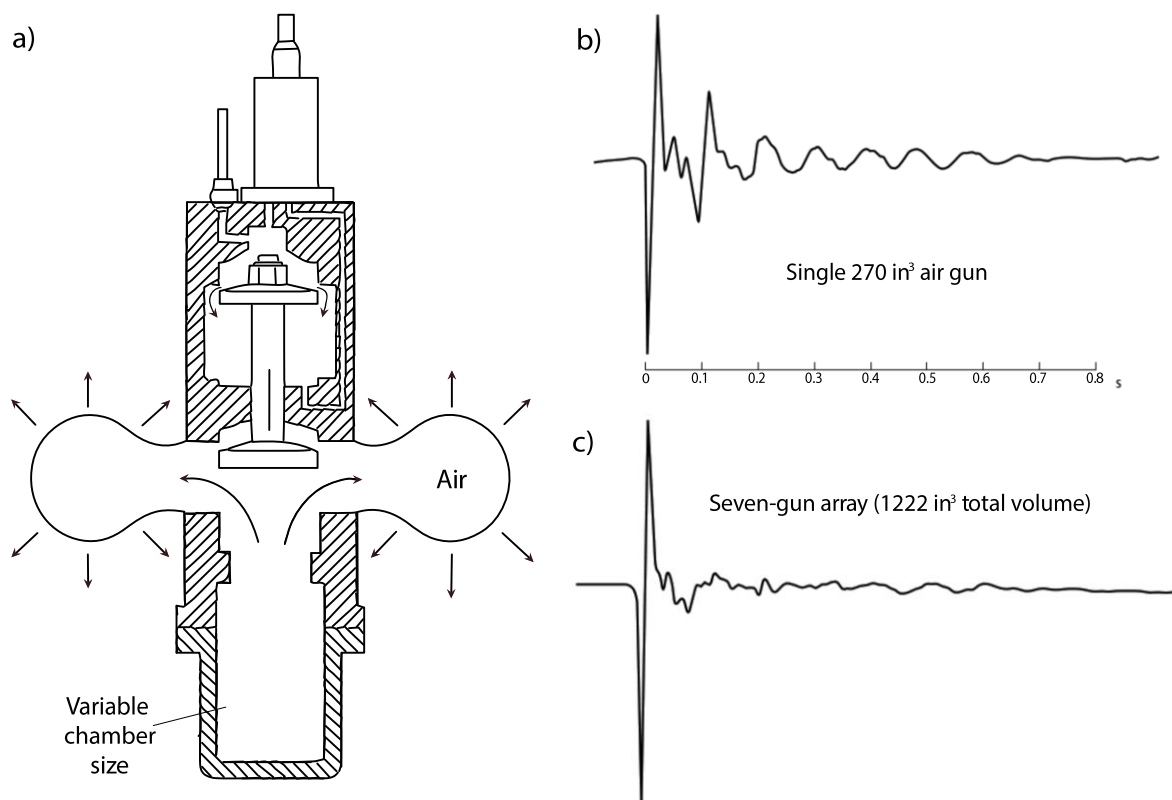
Figure 3.7: a) Cross section of a Bolt air gun. b) Source signature of a single air gun. Note the oscillating waveform as a result of the bubble effect. c) Source signature of a seven-gun array, in which the effect of the bubble pulse is reduced. Modified after Kearey et al. (2002).

3.5.2 Marine survey receivers

Hydrophones are used as receivers for detecting seismic signals, designed to detect pressure changes in water. Two piezoelectric elements of opposite polarity respond to the small pressure fluctuations generated by the arrival of reflected seismic pulses. This information is transmitted to the recording system on the vessel, where the information is stored on magnetic tapes. The hydrophones are mounted at regular intervals in a streamer; a plastic tube filled with oil to provide neutral buoyancy. The streamer is towed behind the seismic vessel at a fixed depth below the surface (Figure 3.8). A streamer is typically between 3 - 6 km long, where a single receiver section is made up of hydrophones grouped in arrays of a pre-defined length, mostly 12.5 or 25 m (Mondol, 2010). A single seismic streamer is towed behind the vessel along with a single source in 2D acquisition surveys, while the use of several parallel streamers and multiple sources are common in 3D surveys.
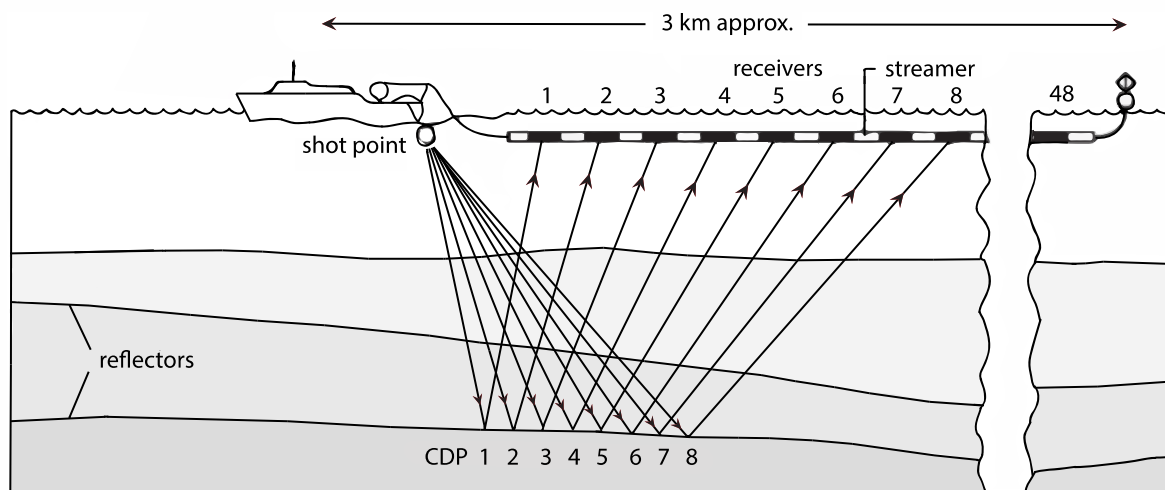
Figure 3.8: Seismic streamer for marine surveys. Modified after Mussett and Khan (2000).

3.6 General processing method

Following the seismic acquisition, the raw seismic data undergo a series of processing steps in order to enhance the seismic image. The aim of seismic processing can be described as follows:

- To display the seismic data in the form of a seismic section, in time or in depth, to obtain and interpret geological information about the subsurface.
- To enhance the signal-to-noise (S/N) ratio by suppressing noise and multiples.

The processing sequence will vary from data to data. This chapter will briefly examine the most common processing steps that define a basic 2D marine processing flow, as providing a complete overview of seismic data processing is not within the scope of this thesis. As diffractions are best analysed in the pre-stack domain, stacking and conventional time migration of the seismic datasets are not performed in this thesis, but are briefly introduced in order understand why these steps are skipped in the forthcoming specific processing method.

3.6.1   Pre-processing

A pre-processing sequence is usually carried out prior to stacking and migration, and may consist of the following steps:

Reformatting and trace editing: Reformatting converts the raw data from industry format into a format recognizable by the processing system, commonly the SEG-Y format, established by the Society of Exploration Geophysicist. Editing removes traces which have been damaged, or which contains considerable noise. Damaged traces should be removed as early as possible and be set to zero or be replaced by interpolated traces.

Filtering of noise: Most marine data are contaminated by different kinds of unwanted noise, such as linear (diffractions and refractions), non-linear (multiples) and ambient noise (rain, wind) (see section 3.2). Several frequency filtering techniques are specifically designed to attack different types of noise, and generally refers to the discrimination against certain frequencies relative to others (Sheriff & Geldart, 1995). Different types of frequency filtering techniques are FK-filtering, deconvolution, low-pass, high-pass and band-pass filters.

Amplitude recovery: The amplitude of seismic signals decreases with time due to e.g. spherical divergence, absorption and loss of transmission. Amplitude recovery is performed to compensate for this (Mjelde, 2011).

Trace muting: This step assigns values of zero to traces during a mute interval in order to remove noise preceding the first arrivals. Muting is an effective method for removing energy from the water layer, the direct wave and the refracted waves.

3.6.2   Common depth point (CDP) sorting

Seismic data are normally sorted after shot-receiver-coordinates (Figure 3.9a) which means that the traces will be sorted in groups where all traces belong to the same shot. When the vessel moves with constant velocity and shoots with set intervals, the same reflection point will be registered by several receivers. Traces with the same reflection point in the midpoint between source and receiver are grouped together in a common midpoint (CMP) gather (Figure 3.9b). The terms CMP and CDP (common depth point) are often used interchangeably, however, they are only equal when reflectors are horizontal. Sorting from common shot point to common midpoint is performed before deconvolution and stacking.
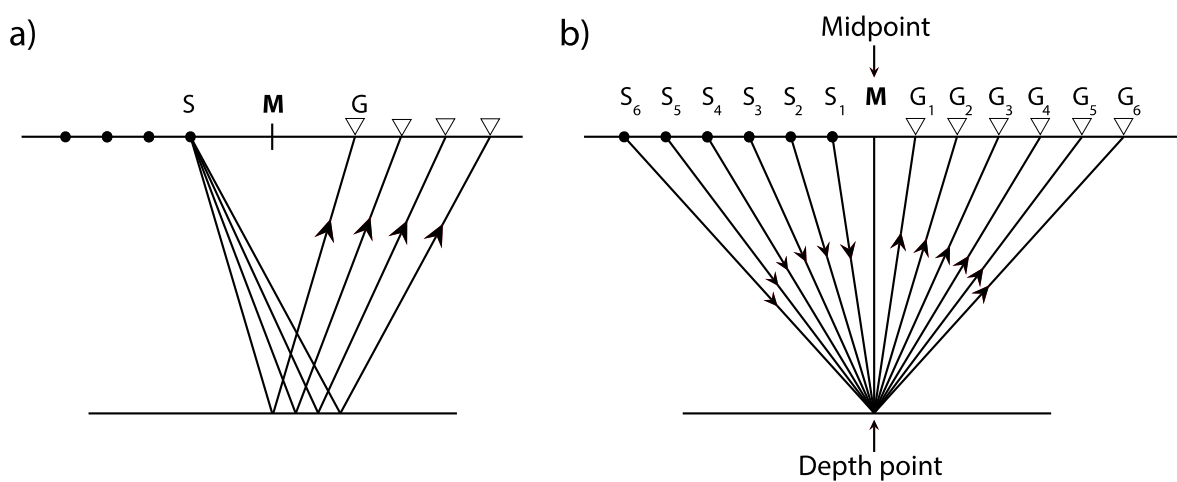
Figure 3.9: a) Shot-receiver gather b) CMP gather. The common midpoint (CMP) equals the common depth point (CDP) only if the reflector is horizontal. Redrawn after Yilmaz (2001).

3.6.3   Deconvolution (inverse filtering)

Multiples may lie within the equivalent frequency spectrum to those of primary reflections and can thus not be suppressed by applying frequency filters. Inverse filtering is thus applied in order to remove multiples from the seismic data. We separate between spiking and predictive deconvolution. Spiking deconvolution compresses the wavelet to a spike, which often increases the temporal resolution, while predictive convolution attempts to remove the multiple energy by predicting their arrival times, while the unpredictable parts, the primary events, are left untouched (Kearey et al., 2002).

3.6.4 Velocity analysis

A velocity analysis has to be carried out in order to apply the most accurate normal moveout correction. Accurate velocity estimations are also essential when depth migrating seismic sections (see section 3.6.7). A velocity spectrum (coherence plot) (Figure 3.10a) is derived from selected CMP gathers by fitting traveltime trajectories to the observed CMP-data (Jones, 2014). This spectrum indicates primary reflectors with high amplitudes, and the picked velocities from these areas are assumed to be the best stacking velocities. The hyperbolic effects from the central gather (Figure 3.10c) are removed in the NMO-corrected gather (Figure 3.10d) when accurately picking velocities from the coherence plot. The resulting event will consequently appear flat if the correct velocity is picked, alternatively "smile" or "frown" if the picked velocity is respectively too high or too low (e.g. Zhu et al., 1998; Yilmaz, 2001). A general assumption is that there is no drastic change in lateral velocity.
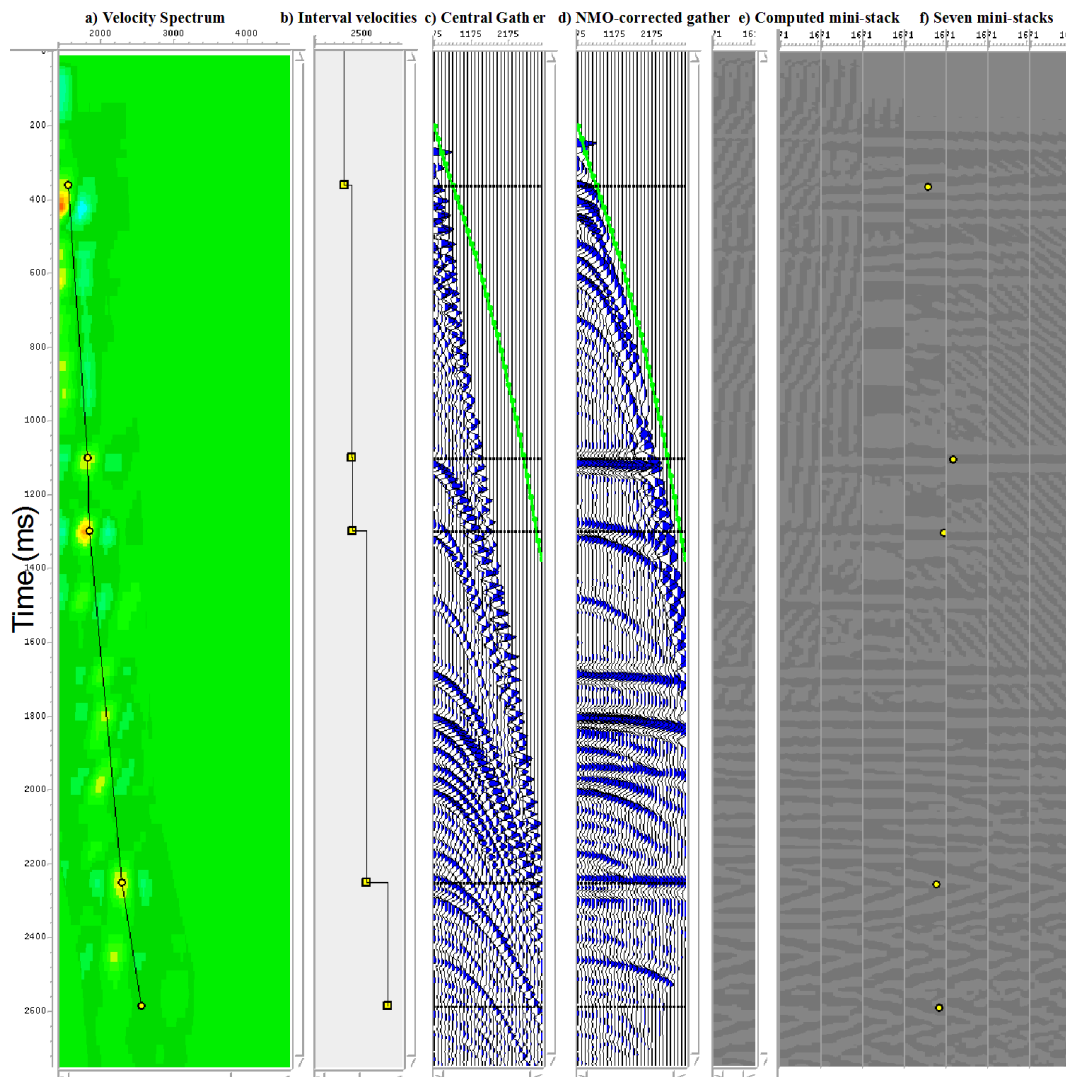
Figure 3.10: Velocity analysis viewer in Chronovista (sub-application of Geocluster). a) Velocity spectrum. b) Interval velocities. c) Central gather. d) NMO-corrected gather. e) Computed mini-stack. f) Seven mini-stacks.

3.6.5   NMO correction

The offset (distance between source and receiver) increases from trace to trace during acquisition, causing a systematic increase of the arrival time of an event. The difference between the traveltime for a certain offset (X) and the vertical (zero-offset) traveltime (T_0) is called normal moveout, and the effect of this difference is displayed as a hyperbolic time-distance curve (Figure 3.11) (Kearey et al., 2002). The moveout effect on traveltimes is removed by using the interpreted stacking velocities, resulting in a simulated zero-offset response, by applying the following formula:

$$T(X) = \sqrt{\left[T^2(0) + \left(\frac{X}{V}\right)^2\right]} \qquad \text{(Eq. 3.6)}$$

where T(X) is the two-way traveltime for a seismic event, X is the source-receiver offset distance, V is the NMO or stacking velocity for this reflection event and T(0) is the two-way traveltime for zero-offset (Kearey et al., 2002).
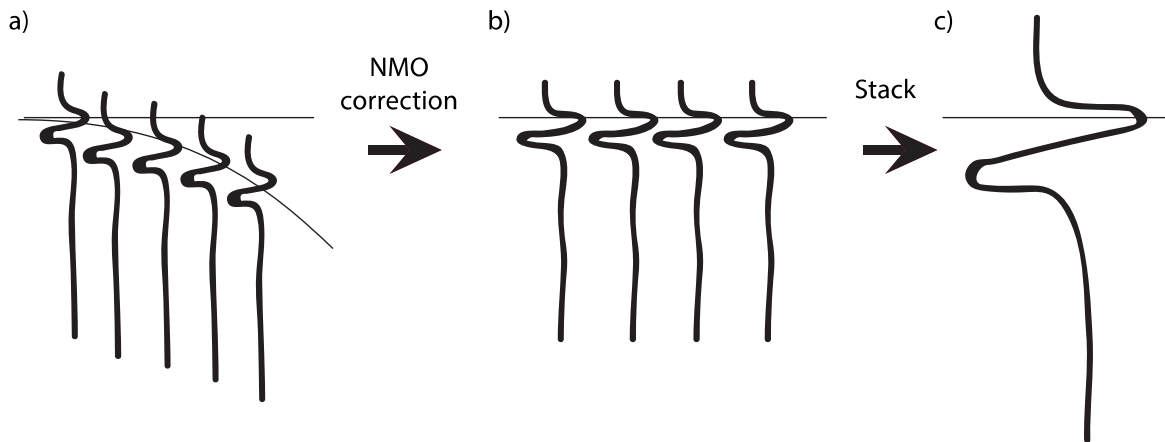
Figure 3.11: a) Hyperbolic time-distance curve as a result of increasing offsets. b) Traces corrected for the moveout effect. c) Stacked trace.

Diffractions have different moveout properties compared to reflections (see section 3.3), and are as a consequence filtered out in a standard NMO and stack procedure (Moser & Howard, 2008). Thus, to preserve diffraction energy, the data are investigated in the pre-stack domain prior to NMO-corrections, stacking and migration.

3.6.6   Stacking

Stacking is in conventional seismic processing performed after applying NMO-corrections on the seismic data, which is defined as a process of which all traces in each CMP gather are combined. This process will average out noise and increase the signal-to-noise ratio (Mousa & Al-Shuhail, 2011). Multiples are attenuated by using the stacking velocities obtained from the velocity analysis.

3.6.7   Migration

Migration is the usually the final step in seismic processing, which aims at placing the recorded data at their correct spatial location rather than their recorded location by using a known velocity model (Bacon et al., 2003). As such, the distorting effects of dipping reflections and diffractions are removed. Migration focuses energy spread over a Fresnel zone, which in order enhances the spatial resolution. Migration is performed both post-stack and pre-stack, the latter yielding better results but is more time consuming, as the traces are not reduced to an approximate zero offset section by stacking. The most commonly used pre-stack depth migration method is the Kirchhoff summation method, which sum amplitudes along a hyperbola or hyperboloid in respectively in 2D and 3D migration in order to collapse diffractions, by stacking each hyperbola at their apex (Figure 3.12) (e.g. Bacon et al., 2003; Bashir et al., 2016b).
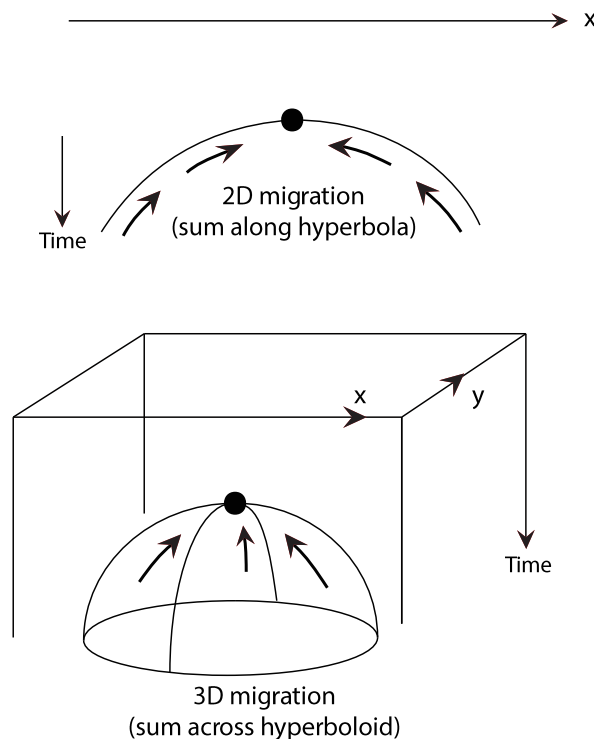
Figure 3.12: Kirchhoff migration in 2D and 3D. Redrawn after Bacon et al. (2003).

4   Data and methodology

This thesis implements processing of both synthetic and real seismic datasets in order to identify regions where diffractions are likely to occur. The acquired synthetic data is a 2D dataset generated from the Gullfaks field in the northern North Sea, while the real seismic dataset is acquired at the Frøya High on the mid-Norwegian continental margin. These datasets were selected due to the presence of structural discontinuities (fault zones) in both seismic sections. The seismic sections are processed in order to reduce unwanted noise and to enhance the diffracted signals, prior to testing a newly developed algorithm for detecting and verifying diffraction events in the recorded seismic. This chapter outlines the complete workflow and methods included in this thesis as well as the datasets used for this process.

4.1   Gullfaks synthetic seismic data

The Gullfaks synthetic dataset is generated from a 2D section cutting through a 3D model of the Gullfaks field. This process was performed by Bent Ole Ruud, senior engineer at the University of Bergen, using a 3D model provided by NORSAR (Figure 4.1). The section was created by an acoustic (P-waves only) finite difference method for 2D models, using a program module from Geocluster (see section 4.3.1) called FDMOD. This module requires a 2D model of P-wave velocities and densities, as well as simulation parameters consisting of layout geometry and the computation parameters. The acquisition parameters for the Gullfaks synthetic 2D survey are defined in Table 4.1.
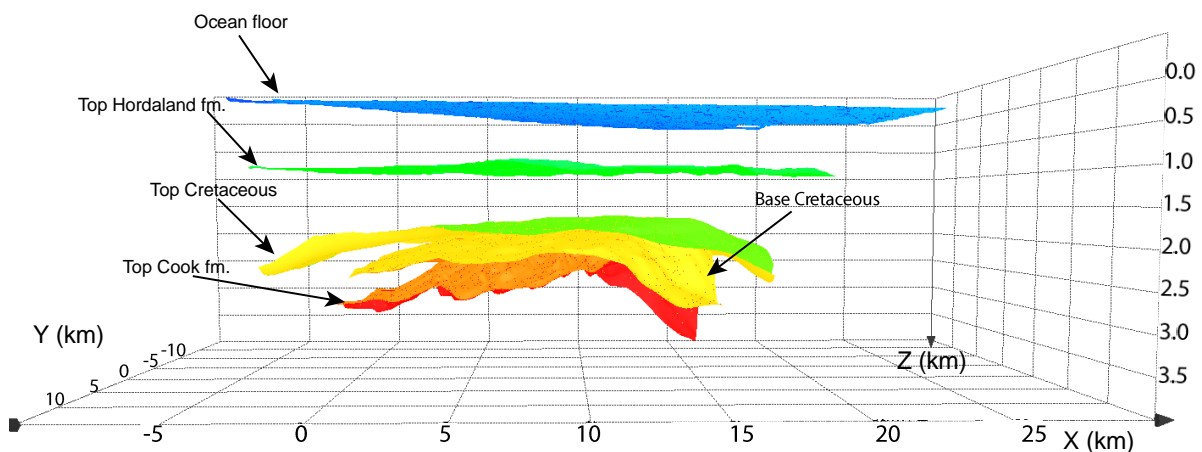
Figure 4.1: 3D model of the Gullfaks field, provided by NORSAR. This model was used in order to create the 2D synthetic section studied in this thesis. The main reflectors are indicated.

The Gullfaks 2D seismic section covers four approximately horizontal reflectors as well as an undulating reflector. The horizontal reflectors include the ocean floor, the Top Hordaland formation, the Top Cretaceous and the Base Cretaceous. The undulating reflector represents the Top Cook formation and is the seismic response of a domino-style fault block geometry. Fault zones between the fault blocks are of interest as diffracted energy is expected to be found in these regions.

Table 4.1: Acquisition parameters for the Gullfaks synthetic 2D survey.

GULLFAKS SYNTHETIC DATA	
Grid spacing	3.125 m
Time step (Ricker Source wavelet)	0.5 ms
Centre frequency	20 Hz
Output sampling rate	4 ms
Recording time	3.0 s
Number of shots	177
Distance between shots	50 m
Number of receiver groups	120
Distance between receiver groups	50 m
Least offset (recorded at channel #1)	100 m

4.2   Frøya High real seismic data

The real seismic data is acquired in the area of Frøya High, an offshore area about 50 kilometres west for the Frøya island in Trøndelag, Norway. The seismic dataset is obtained from the DISKOS database, a Norwegian national data repository of exploration and production data covering the Norwegian Continental Shelf. The dataset comprises two 2D lines, MB-23-84 and MB-24-84, where line MB-23-84 is used in this thesis. This seismic line has a horizontal extent of 52.2 km and starts approximately 20 km northwest of the Smøla Island, from 63°29'55.9" N, 7°26'05.8" E to 63°45'38.0" N, 6°36'55.0" E (Figure 4.2).
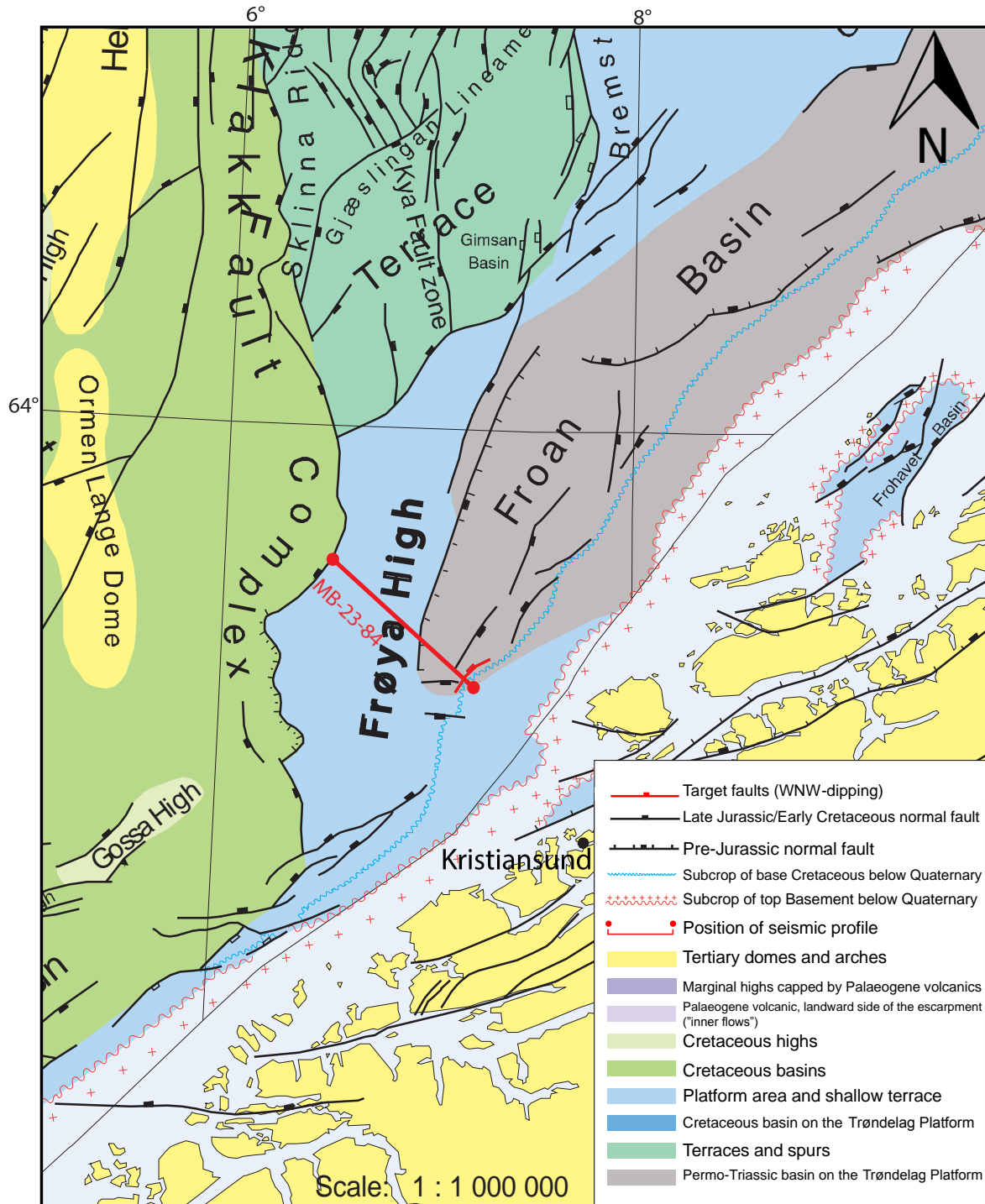
Figure 4.2: Overview of the study area on the mid-Norwegian continental shelf. Seismic line MB-23-84 is illustrated in red. It crosses late Jurassic/Early Cretaceous and Pre-Jurassic normal faults, crosses the Frøya High and terminates adjacent to the Klakk Fault Complex. WNW-trending faults, marked by a red normal fault-symbol in the Froan Basin, are subject for further investigation. Modified after Blystad et al. (1995).

Line MB-23-84 is subject to multiple WNW-trending normal faults, represented by a red normal fault-symbol in Figure 4.2. Diffracted energy is presumed to be detected around these normal faults. Raw pre-stack shot data is provided, originating from the seismic acquisition performed by Seismic Profilers, August 1984. All further processing of the real seismic data in this thesis is performed using the raw pre-stack data. Contrary to the synthetic data from Gullfaks, velocity models are provided for this dataset. Two text-files containing velocity-time pairs per shot point are provided together with the raw data, deriving from processing made by Merlin Profilers A/S and Veritas DGC. The stacked velocities provided by Veritas DGC covers a wider range of shot point numbers compared to data from Merlin Profilers A/S, as well as a higher sample ratio, and are thus favoured for further processing. Survey specifications for the 2D seismic survey are summarised in Table 4.2.

Table 4.2: Acquisition parameters for the 2D seismic survey performed at the Frøya High.

MB-23-84		
Source	Vessel	Nina profiler
	Vessel positioning	Primary Argo, Secondary Syledis G.P.S
	Recorded by	Seismic Profilers, Aug. 1984
	Source type	Airgun array
	Operation pressure	2000 psi
	Volume (per source)	5946 cubic inches
	Source depth	7.5 m
	Shooting direction	25 m
Cable	Cable type	Teledyne T1
	Cable length	3000 m
	Cable depth	7 m average
	Near offset	160 m
	Number of groups	120
	Group interval	25 m
Recording	CDP-spacing	12.5 m
	Fold	60
	Recording length y-axis	7000 ms (TWT)
	Sample rate	4 ms
	Recording length x-axis	52.21 km
	Low cut filter	5.3 Hz (18 dB/oct)
	High cut filter	90 Hz (72 dB/oct)

4.3   Workflow and specific seismic processing

As diffractions are best analysed and preserved in the pre-stack domain, a different approach to processing is required. Stacking and migration of the seismic datasets are not performed, as these methods suppress diffractions (see section 3.6.6 and 3.6.7). However, a Kirchhoff pre-stack depth migration (PSDM) process is performed in Geocluster, for the purpose of defining image areas. The seismic processing performed in this thesis is thus kept to a minimum, in order to preserve the energy from diffracted waves. The complete workflow and different processing steps of this study are presented in Figure 4.3. Descriptions of the processing steps are given in the following sections.
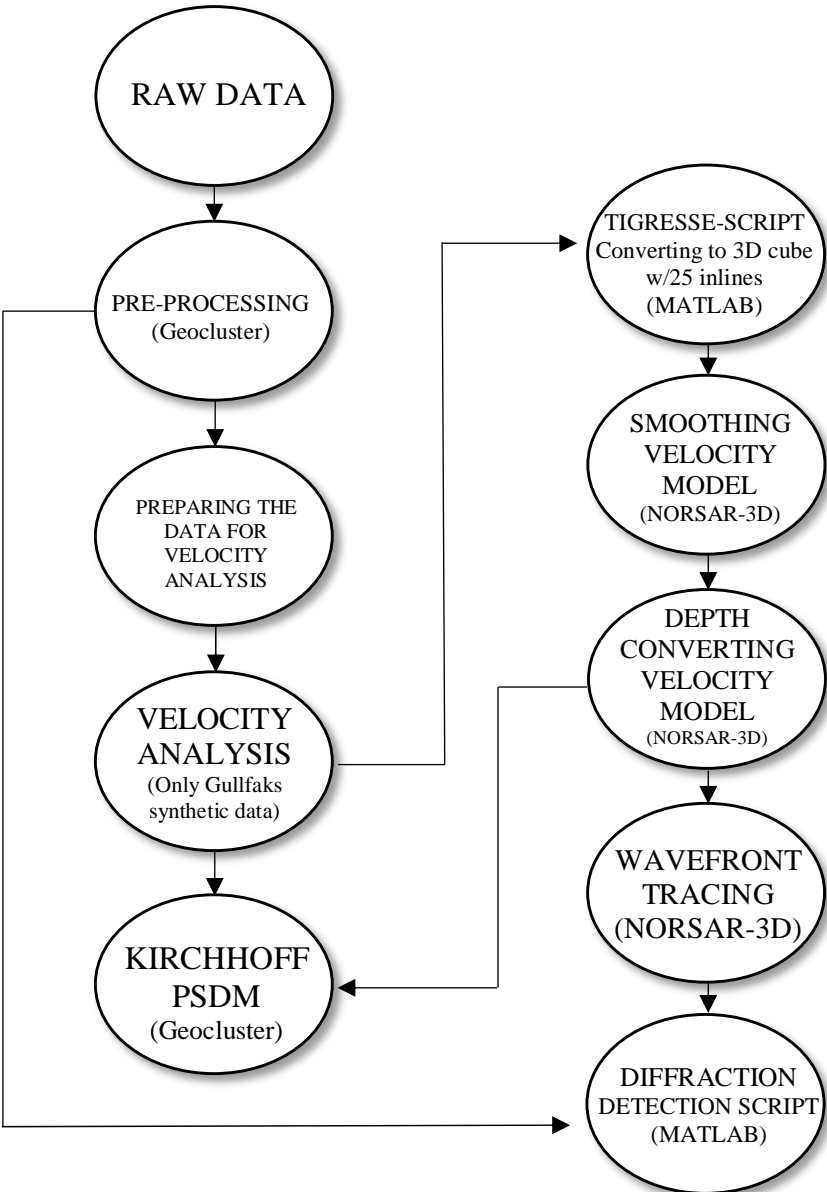
Figure 4.3: Workflow illustrating the different processing steps performed on the synthetic and real seismic data.

4.3.1   Software

Geocluster 5.0, a trademark of CGG, is a seismic processing software providing over 400 program modules to be used for processing 2D and 3D seismic, for both land and marine surveys. This software is used to process the acquired synthetic and real seismic data. The program modules are linked together using the interactive application XJOB, creating seismic workflows (Figure 4.4). Chronovista/Geovel (sub-applications of Geocluster) and NORSAR-3D are used to process the P-wave velocity models. The latter is also used in order to perform wavefront tracing. The workflow sequence terminates in MATLAB, using a script designed to image diffractions by creating semblance plots. Functions accessible from the SeisLab package, developed by Eike Rietsch (available for download at mathworks.com), are implemented in this processing sequence.
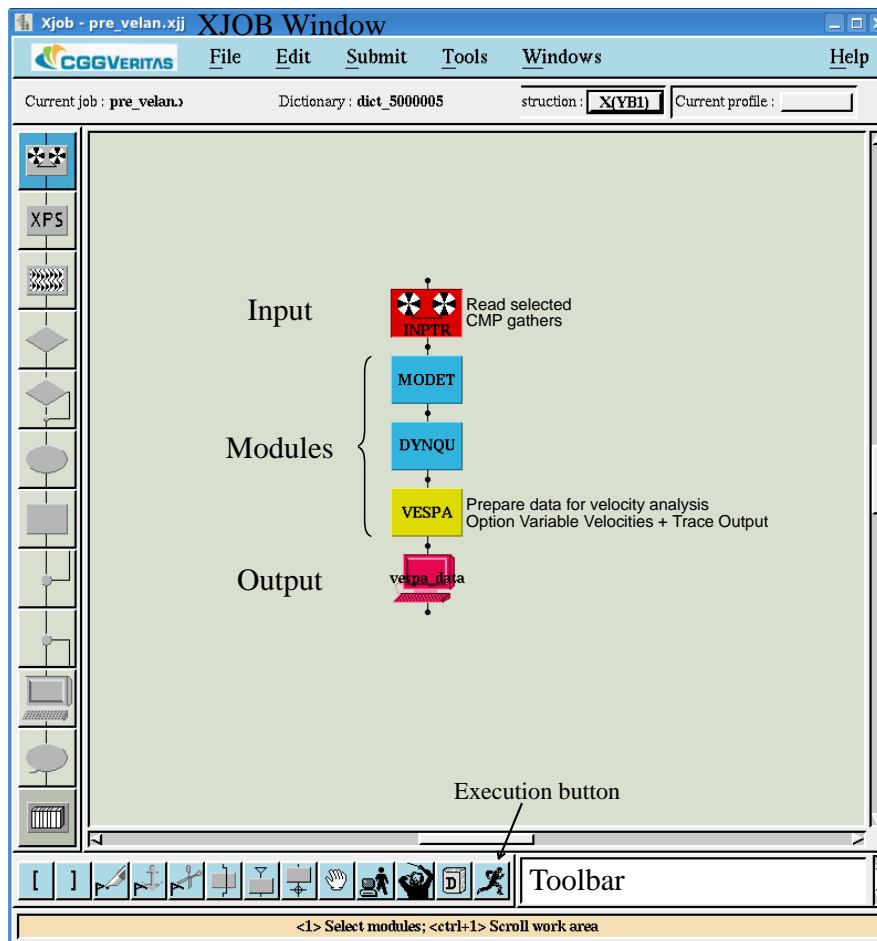
Figure 4.4: Illustration of a seismic workflow created in XJOB, a sub-application of Geocluster 5.0, which consists of different processing modules that are linked together and subsequently submitted for analysis and execution. The output can further be read, analysed and managed by other interactive applications. This is an example of a processing sequence that converts the input CMP gathers of a seismic section to an output file that is readable by the interactive velocity picking application Geovel.

4.3.2   Pre-processing

Pre-processing is essential in order to improve the signal-to-noise (S/N) ratio of the seismic sections prior to implementing them in a diffraction detection process. Noise greatly influences the diffraction analysis, as the S/N of diffractions separated from specular reflections is usually low (Lin et al., 2018). Noise reduction is thus targeted by using various processing modules.

Reformatting and trace editing: Reformatting and trace editing is only applied to the real seismic data, as the raw synthetic data from the Gullfaks field is already predefined in Geocluster. The raw data from the real dataset from the Frøya High is thus converted from SEG-Y format to CGG-format using the SEGIN-program module. The first 4 traces are removed, as they are damaged. Trace length is reduced from 7000 ms to 3004 ms, while a reduction from 52.2 km to 18 km length (from 1-4176 CDPs to 1-1441 CDPs) is applied in x-direction. This is performed in order to decrease computation times, as well as narrowing the seismic profile to the target areas.

Amplitude recovery: The REFOR module is used to make an amplitude correction to compensate for spherical divergence, absorption and loss of transmission.

Defining header words: Header words are defined using the module MODET, which modifies a trace header word by using mathematical functions. Some headers are already defined in the raw data, such as shot point number and channel number, while the CDP-numbers and offset numbers need to be defined. These header words are used throughout the subsequent processing; thus, it is of importance that the mathematical functions defining the words are listed correctly. The CDP-number is calculated from the shot and channel number using the formula

$$CDP = A \times SP + B \times CHN + C \qquad \text{(Eq. 4.1)}$$

where A, B and C are constants depending on the acquisition geometry, SP is the shot number and CHN is the channel number.

Sort to CDP gathers: After computing the CDP-numbers, the input traces are sorted from shot point gathers to CDP gathers using the module BSORT. Sorting from common shot point to common depth point is performed before deconvolution.

Mute: The purpose of the mute is to remove the direct wave and wide-angle reflections. Mute libraries are defined for the synthetic and real seismic data and applied in order to remove noise and energy from the direct wave.

Multiple attenuation: Multiple attenuation is achieved using different modules. The Gullfaks synthetic data is processed using predictive deconvolution module TRITA, while the real seismic data (MB-23-84) is processed using F-k multiple attenuation (FKMUL) and least-square multiple removal (LEMUR), as suggested by Bent Ole Ruud, senior engineer at the University of Bergen.

· *Predictive deconvolution:* The TRITA module performs a time variant predictive deconvolution. A water-bottom library created through Teamview (sub-application of Geocluster), is used as input. Predictive deconvolution is generally used to attenuate long period multiples (CGGVeritas, 2008). The result is presented in Figure 4.5.

· *F-k multiple attenuation:* The FKMUL module is used to eliminate multiples in a CDP gather within a given time window. This is accomplished through filtering in the F-k (frequency-wavenumber) domain, after a dynamic correction has been applied to traces (CGGVeritas, 2008). This module is performed on the real seismic data (line MB-23-84) and requires an input velocity model.

· *Least-square multiple removal*: The LEMUR module is designed to suppress long-period water-bottom multiples by predicting their arrival times and subtracting the estimated multiples from the data. Inputs are CMP-gathers prior to NMO correction.
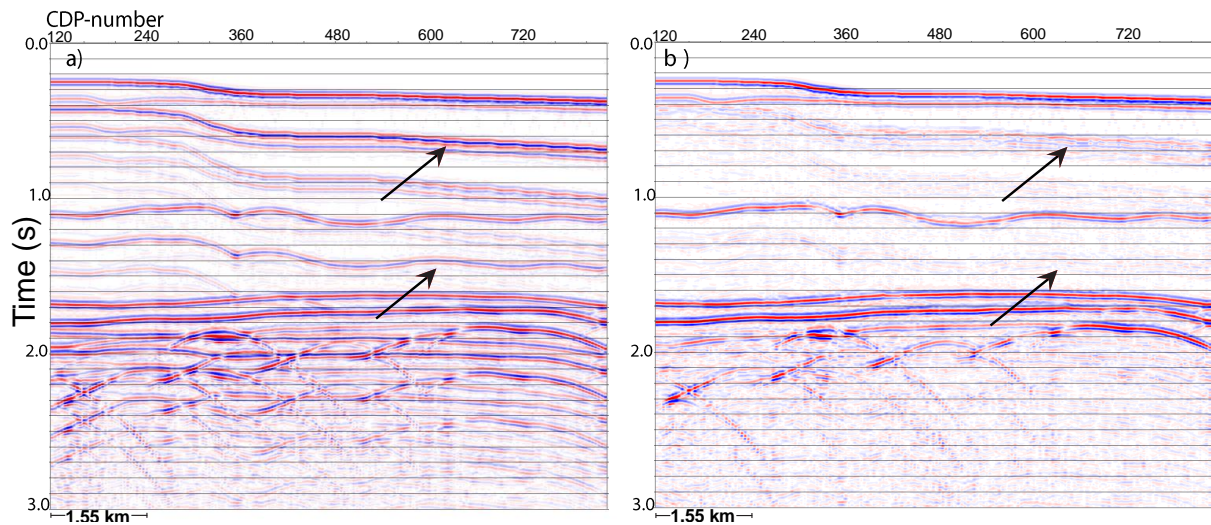
Figure 4.5: Gullfaks synthetic data before and after deconvolution. The datasets illustrate an offset gather processed in time, where the least offset (100 m) is visualised, where a) illustrates the seismic data prior to deconvolution and b) illustrates the seismic after deconvolution. Multiple energy is to a large extent removed after performing a time variant predictive deconvolution, as illustrated by arrows.

Sort to common offset gather: To preserve the diffracted energy, CDP stacking is avoided. However, in order to visualise the seismic sections, the data are sorted to offset gathers after performing multiple attenuation. A near-offset section is selected for output (as seen in Figure 4.5), which is used in further processing.

4.3.3   Velocity analysis

Unlike the real seismic dataset from the Frøya High, a velocity model is not provided for the Gullfaks synthetic dataset. Thus, an individual velocity analysis is performed in the Geocluster application Chronovista, in which velocities are picked for several CDPs and interpolated between these. More information on velocity analyses is given in chapter 3.6.4. Subsequently, the picked time-velocity pairs are exported as an ascii-file.

4.3.4   Tigress ascii file

In order to import the velocity models to the NORSAR-3D software, the geometry and property information is converted into a Tigress ascii-file. This is an ascii format for 3D grids, consisting of a simple header describing the geometry of the 3D grid, followed by data, one value at each line. NORSAR (2012) describes the format with an example:

```
Xmin, Ymin, Zmin (at location 1,1,1)        .000   .000   .000
DX, DY, DZ (distance in each direction)      .025   .500   .500
nz, nx, ny (order and number)                  11    201     11
  2.00
  2.00
  2.00
  2.00
  2.00
  ...
```
In which the data is ordered as follows:
```
  f(x1, y1, z1),   f(x1, y1, z2),   ..., f(x1, y1, zn),
  f(x2, y1, z1),   f(x2, y1, z2),   ..., f(x2, y1, zn),
                ...
  f(xk, y1, z1),   f(xk, y1, z2),   ..., f(xk, y1, zn),
  f(x1, y2, z1),   f(x1, y2, z2),   ..., f(x1, y2, zn),
                ...
  f(xk-1, ym, z1), f(xk-1, ym, z2), ..., f(xk-1, ym, zn),
  f(xk, ym, z1),   f(xk, ym, z2),   ..., f(xk, ym, zn),
```

These ascii-files are created using MATLAB (script provided by Einar Iversen, associate professor at the University of Bergen). As both P-wave velocity models used in this thesis are in 2D, an approximation to a 3D cube is made by placing a number of identical 2D lines after each other, defining a 2.5D model. The pre-stack depth migration process in Geocluster requires a velocity cube with minimum 25 lines, which is why a 3D cube approximation is made. The resulting models thus vary in the x-direction, but not in the y-direction. The nodes define the number of points within the 2.5D grid. In order to correctly execute the subsequent pre-stack depth migration process in Geocluster, it is important that the number of nodes in the x-direction is equal to, or higher than, the amount of CDP-numbers from the associated seismic profiles. The values of the 2.5D cubes for the synthetic and real velocity models are defined in Table 4.3.

Table 4.3: Properties of the 2.5D cubes defining P-wave velocities. The Gullfaks synthetic velocity cube to the left, and the Frøya High velocity cube to the right.

Gullfaks synthetic velocity cube			
Axes	X (km)	Y (km)	Z (km)
Low	0	4.5	0
High	12	5.5	3.36
Increment	0.0125	0.0417	0.005
# Nodes	961	25	673

Frøya High velocity cube			
Axes	X (km)	Y (km)	Z (km)
Low	0	0	0
High	18	1	3.04
Increment	0.0125	0.0417	0.004
# Nodes	1441	25	761

4.3.5   Velocity modifications

NORSAR-3D is used in order to modify the velocity libraries. This is performed by using the Model Builder function. The models are imported from Tigress ascii-files as properties in NORSAR-3D, and subsequently smoothed (both laterally and vertically), depth converted (Figure 4.6) and cropped in the Model Builder. As ray tracing (used in Kirchhoff migration) has difficulties dealing with abrupt velocity variations (Vinje et al., 2013), a smooth velocity model with no significant lateral or vertical variations is a prerequisite for obtaining reliable results from the subsequent wavefront tracing. Thus, the models are smoothed both laterally and vertically using a smoothing diameter of 0.1km (in both lateral and vertical direction). The smoothing option in NORSAR-3D uses a Hamming filter, which is defined as a spatial low-pass filter. Depth conversion is performed by using the "Stretch time $\longleftrightarrow$ depth" option in the Model Builder. The velocity models in time may stretch themselves by constructing a stretch function from the model itself before applying this function to the selected models - resulting in a vertical stretch from time to depth. The final depth converted velocity property (Figure 4.6c) is exported as a SEG-Y file to be used in pre-stack depth migration in Geocluster, described in the following section, as well as stored as a model ready for computing traveltimes by wavefront tracing in NORSAR-3D.
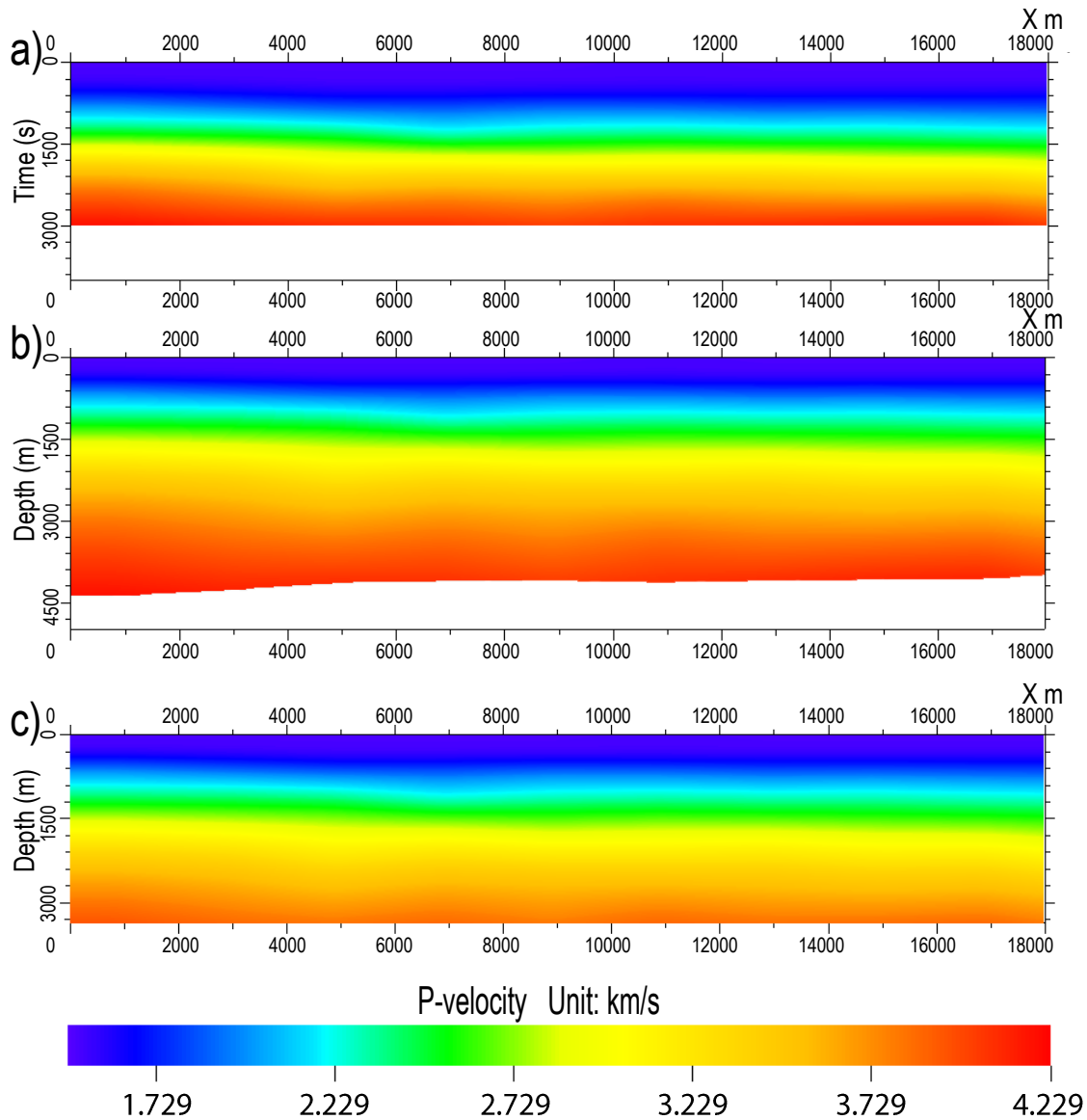
Figure 4.6: Velocity model associated with line MB-23-84 from the Frøya High, whereas a) is the smoothed P-wave velocity model in time, b) is the depth converted velocity model and c) presents the depth converted model, cropped to a vertical depth of 3365 m.

4.3.6 Pre-stack depth migration (PSDM)

Running the Kirchhoff 3D pre-stack depth migration (PSDM) program in Geocluster is by far the most challenging procedure in the processing flow, as it requires an enormous amount of input details, including a velocity cube with at least 25 inlines. The process is carried out with the sole purpose of defining image areas in depth for successive wavefront tracing in NORSAR-3D. The program in Geocluster consists of three different processes, performing different jobs. Numerous libraries are defined in all processes and must be identical in order to run the processing sequence.

KIMTR: Reads data from the pre-processing job, sorts them back to shot gathers, defines headers words and outputs a trace file and two trace header files suitable for subsequent processing in KIMIP.

WEIKO: Computes traveltimes between each source/receiver position at the surface and a set of target points in depth. Input is the velocity cube and anisotropic parameters.

KIMIP: Performs the 3D pre-stack Kirchhoff depth migration. The KIMIP Kirchhoff algorithm is a trace-by-trace migration. The appropriate traveltimes are interpolated from those computed by the WEIKO-process, then output and summed. The final depth migrated image (Figure 4.7) represents the sum of the contribution of each input trace and is used to define image areas in which there is a chance of discovering diffracted energy (e.g. in fault zones).

Figure 4.7: The Gullfaks synthetic seismic dataset after performing pre-stack depth migration. The output is used in order to define image areas in depth to be used in subsequent wavefront tracing in NORSAR-3D.

38

The output depth image from this process was initially intended to be used for selecting image areas in depth within both the synthetic and the real seismic dataset. However,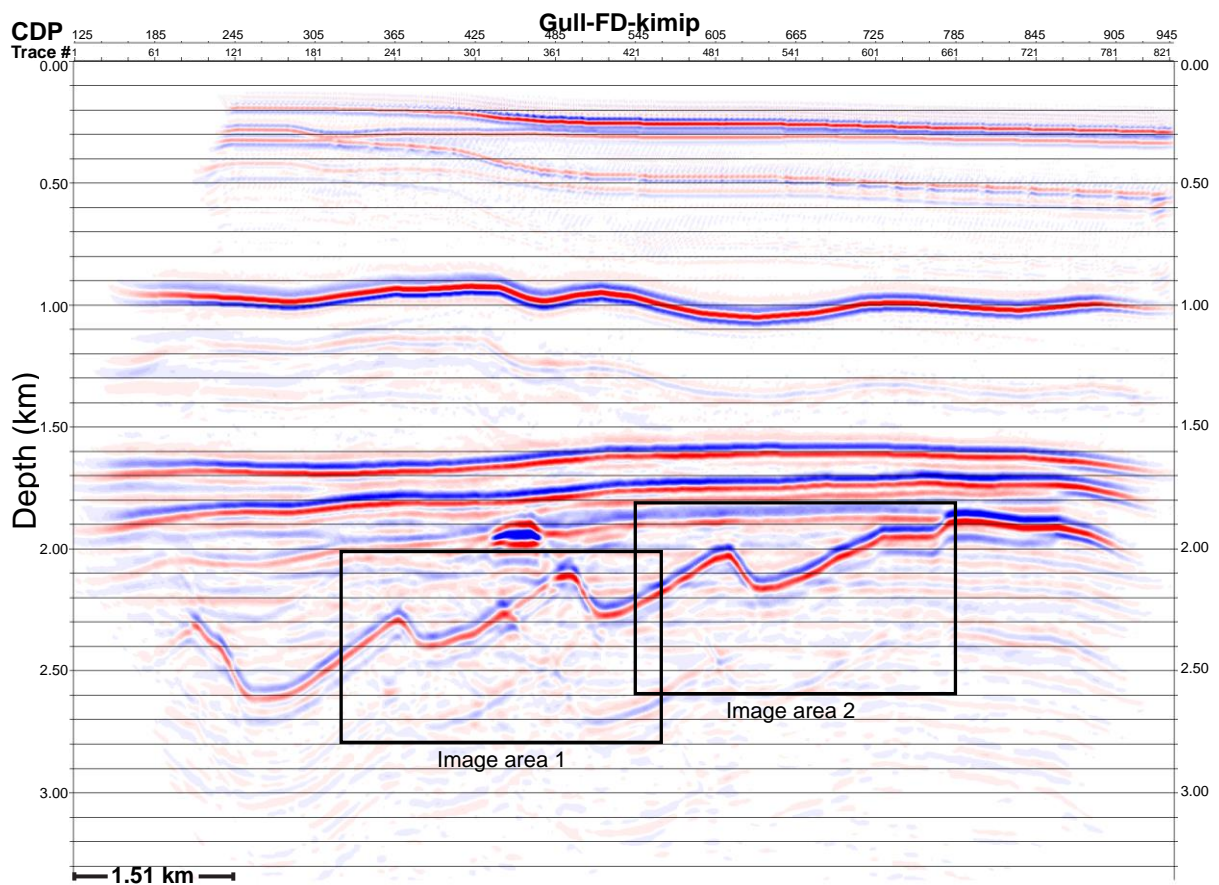 after carrying out this process on the synthetic dataset, it was recognised that the process is too time consuming and complex to account for the real seismic dataset. The Kirchhoff PSDM-process was however tested on the real seismic data, but the results were insufficient. This may indicate a flawed velocity model or errors within the numerous input libraries. After all, Kirchhoff pre-stack depth migration is pursued in the following MATLAB diffraction script, though within the specified image areas and not by using the full seismic section. Consequently, the Kirchhoff 3D PSDM-program in Geocluster is solely used for determining image areas within the synthetic seismic dataset.

4.3.7   Defining image areas

Let an *image area* refer to a spatial 2D cube of receivers, targeted around regions of interest and intended for subsequent wavefront tracing performed in NORSAR-3D. By using the PSDM output from the synthetic seismic dataset, image areas in depth are defined in prominent fault zone regions. As no sufficient PSDM-result is obtained for the real seismic data, the image area related to this dataset is determined by using the offset gather in the time-domain obtained after the pre-processing sequence. As the survey areas are depth dependent, the lateral and vertical range of the survey are set large enough to compensate for the displacement of reflectors during depth migration. This is done to ensure that target discontinuities are covered. The global spatial positions for the receivers are static in the sense that their positions are equal for all the shots (NORSAR, 2012). Shots are distributed in a single line close to the surface, with a shot spacing of 40. A receiver distance of 12.5 m in x-direction is defined in order to match the receiver positions with the CDP-numbering from the associated seismic profiles.

Table 4.4 presents a defined survey grid from the Gullfaks synthetic data, which is loaded into the succeeding NORSAR-3D Common Shot Wavefront Tracer. The other survey grids that are used in this thesis are presented in chapter 5. Despite running the wavefront tracer on 2.5D velocity models, traveltimes are calculated using a 2D receiver grid, where the shot-receiver grid consists of a single y-direction node. As the seismic profiles are two-dimensional, traveltimes exceeding this dimension are not required.

Table 4.4: Image area 1, associated with the Gullfaks synthetic data.

IMAGE AREA 1 – GULLFAKS SYNTHETIC DATA				
SHOTS:	**START**	**INCREMENT**	**NODES**	**UNIT**
X-DIR.:	1.0	0.040	151	km
Y-DIR.:	5.0	0.040	1	km
DEPTH:	0.010	0.040	1	km
RECEIVERS:	**START**	**INCREMENT**	**NODES**	**UNIT**
X-DIR.:	2.5	0.0125	241	km
Y-DIR.:	5.0	0.010	1	km
DEPTH:	2.0	0.005	161	km

4.3.8   Wavefront tracing

Traveltime computations are required in order to carry out the following pre-stack Kirchhoff depth migration sequence described in the following section. By using the Common Shot Wavefront Tracer function in NORSAR-3D, one-way traveltimes are calculated from a number of surface stations to a number of potential diffraction points (Figure 4.8) during wavefront tracing. This concept is based on standard dynamic ray tracing, but rather than tracing individual rays, the wavefront tracer propagates entire wavefronts time-step by time-step - creating a 'moving surface' that passes through the model (NORSAR, 2012). The wavefront is thus defined as a curve (in 2D) of constant traveltime which originates from the source and propagates towards the receivers (Vinje et al., 1993). The inputs to this process are the velocity models processed in depth and the defined image areas. The calculated traveltime data are sorted so that traveltimes belonging to each potential diffraction point is gathered. The reason for this is that the calculation method in NORSAR-3D is much more effective «top-down» than «down-up». For each «shot», the wavefront tracer will effectively calculate traveltimes, with interpolation, for a 3D grid with possibly millions of «receivers». The following event attributes are exported: shot and receiver topology indices, spatial positions (x-, y- and z-direction) of shots and receivers as well as first arrival traveltimes. These attributes are subsequently used as input to the algorithm described in the following section.
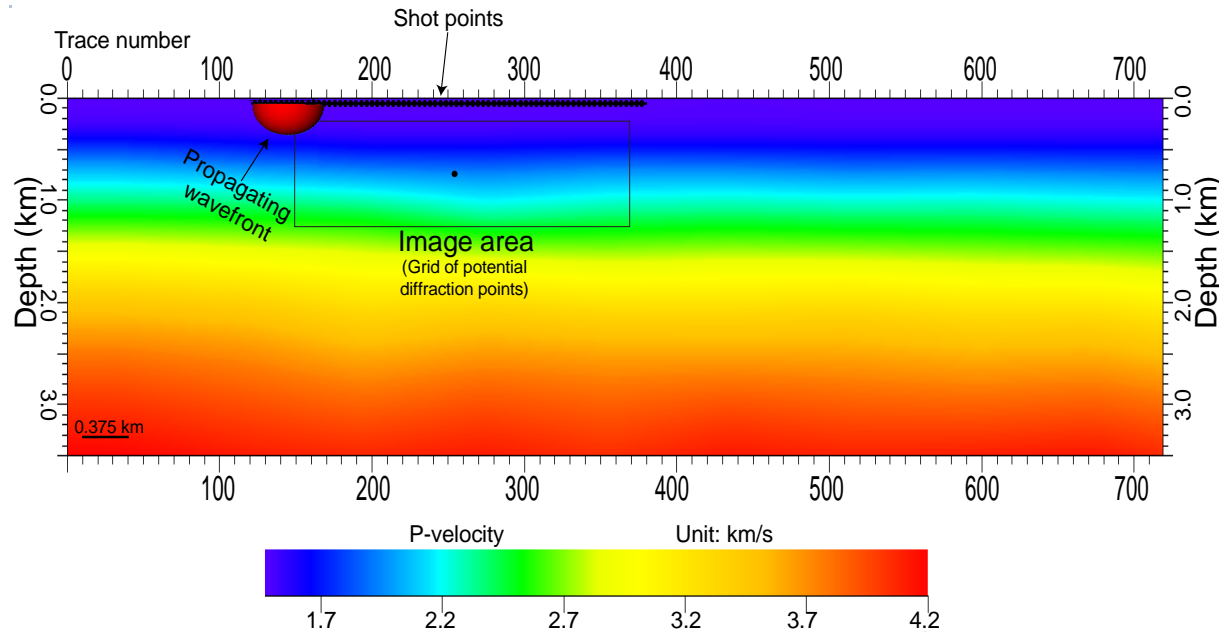
Figure 4.8: Illustration of the wavefront tracing process performed in NORSAR-3D, using the P-wave depth converted velocity model from the Frøya High dataset. One-way traveltimes are computed from a number of shot points to a number of potential diffraction points within the image area, using a propagating wavefront. A potential diffraction point is illuminated in the centre of the image area, which represents a 2D grid of potential diffraction points.

4.3.9 Diffraction detection algorithm

A diffraction detection algorithm based on the computation of semblance is used in this thesis. The algorithm is implemented as a MATLAB-script (developed by Einar Iversen, associate professor at the University of Bergen, spring of 2019). The script applies a classic diffraction stack on seismic input data processed in time, using conventional full-wave Kirchhoff pre-stack depth migration, as described by Moser and Howard (2008):

$$V(\mathbf{x}) = \int dt \, d\mathbf{s} \, d\mathbf{r} \, w(\mathbf{s}, \mathbf{x}, \mathbf{r}) \, U(t, \mathbf{s}, \mathbf{r}) \, \delta(t - t_d(\mathbf{s}, \mathbf{x}, \mathbf{r})) \qquad \text{(Eq. 4.2)}$$

which uses a stacking traveltime trajectory given by

$$t_d(\mathbf{s}, \mathbf{x}, \mathbf{r}) = T(\mathbf{s}, \mathbf{x}) + T(\mathbf{x}, \mathbf{r}) \qquad \text{(Eq. 4.3)}$$

where the reflectivity image is given by $V(\mathbf{x})$, depending on the subsurface image point $\mathbf{x}$, and $U(t, \mathbf{s}, \mathbf{r})$ represents the full-wave data, depending on time t and shot/receiver position $\mathbf{s}/\mathbf{r}$ and the Dirac delta function δ (Moser & Howard, 2008). $w(\mathbf{s}, \mathbf{x}, \mathbf{r})$ is a weighting function, chosen

equal to one. The stacking traveltime trajectory $t_d(\mathbf{s}, \mathbf{x}, \mathbf{r})$ represents the traveltime of an elementary diffraction from the image point $\mathbf{x}$, and T(s, x) is the traveltime from s to x (and similarly for T(x, r) (Moser & Howard, 2008). This process, as mentioned in section 3.6.7, focuses diffractions by stacking each hyperbola at their apex. The resulting Kirchhoff pre-stack depth migrated seismic image is available for output.

Specular reflections are then optionally suppressed from the full-wave Kirchhoff depth migrated offset gather by reflection focusing. This method was proposed in a study by Khaidukov et al. (2004), and further developed by Moser and Howard (2008). Due to the relatively weak energy of diffractions, a separation process is essential in order to accurately detect diffractions. Separation is made possible by exploiting the fact that reflections and diffractions from a discontinuity at the same depth differ in moveout properties (see section 3.3). Specular reflections can be identified in the reflection-focus gather as points with sharply focused energy, which can be found by a simple scanning algorithm that is used to define reflection suppression filters on the full-wave near-offset gathers (Moser & Howard, 2008). In other words, we regard the reflection traveltime curve as a diffraction traveltime curve, with a stacking traveltime trajectory given by

$$t_r(\mathbf{s}, \mathbf{x}, \mathbf{r}) = T(\mathbf{x}, \mathbf{r}) \qquad \text{(Eq. 4.4)}$$

which replaces t_d in Eq. 4.3 by t_r in Eq. 4.4 in the stack (Eq. 4.2), allowing to focus the reflected energy to its virtual source point (Moser & Howard, 2008). The reflection traveltime curves are found by ray tracing using NORSAR-3D. If the method is correctly performed, this leaves us only the diffracted energy including any noise that was not identified as a reflection signal (Decker et al., 2017). The resulting diffraction image will have a poor signal-to-noise ratio due to this appearance of noise, which is why semblance summation is carried out. For further review of the reflection focusing process, see Khaidukov et al. (2004) and Moser and Howard (2008).

Some adjustments have been made to this classic diffraction stack, however. During the summation process, semblance, a statistical parameter ranging between 0 and 1, may be calculated in a time window around the traveltimes obtained from NORSAR-3D (Figure 4.9). Semblance is used as an attribute to correlate between a reference section and a modified section, to measure the degree of similarity. High semblance peak values will thus indicate

detected diffraction points. The width of the applied time window corresponds to the dominant wave period, T, which relates to a dominant frequency $= \frac{1}{T}$. This frequency, f, can be entered into the MATLAB script. If this option is selected, the probability of detecting diffracted waves increase as semblance is calculated in a wider area than if not applying this option. A frequency of 20 Hz is used throughout this thesis, which yields quite wide and easily interpretable semblance peaks. Computation time is significantly increased when integrating the time-window option (e.g. from 1.5 hours to 17 hours using the real seismic dataset).
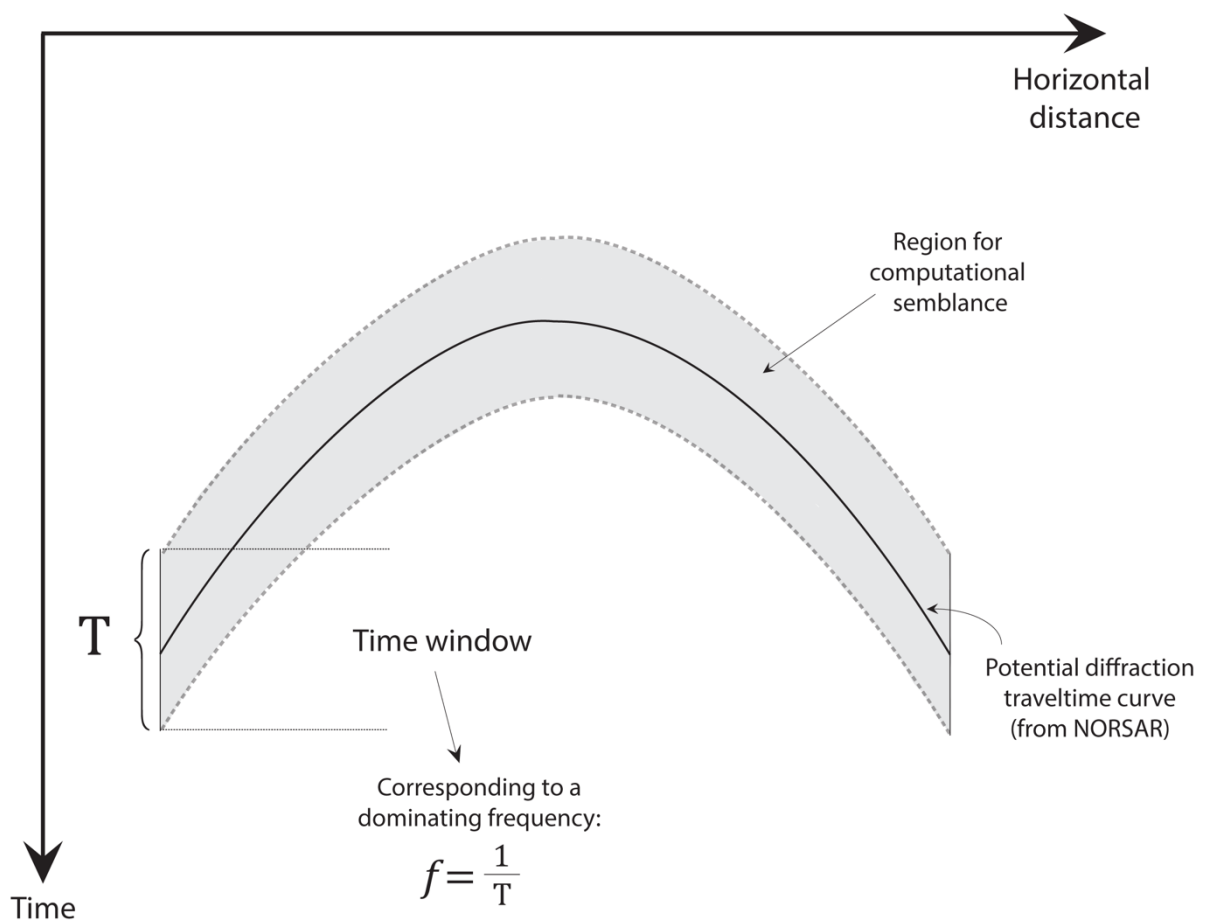
Figure 4.9: Optionally, semblance is computed in a time window around the potential diffraction traveltime curves obtained from NORSAR-3D. The width of the time window corresponds to a dominant wave period, relating to a dominating frequency, f, which is optionally used as input to the diffraction detection algorithm.

Another adjustment to the summation process has been made. The diffraction amplitudes go through a polarity shift at minimum traveltime, which needs to be accounted for. An algorithm is developed for correcting the semblance measurement for amplitude variations, optionally also for a specific time window. This algorithm is derived from a formula

presented by Fomel (2009), which is a modification of a traditional semblance formula in order to account for amplitude polarity shifts.

It is also worth mentioning that the preceding multiple attenuation process, executed during seismic processing, might also impact and possibly attenuate the diffracted energy. As the attenuation process is controlled by algorithms within the different Geocluster modules and is thus not under full control by the user – I use multiple-attenuated data as well as non-multiple-attenuated data as input to the algorithm. The idea is that I might be able to determine whether or not the multiple attenuation process has attenuated diffracted waves by comparing semblance plots deriving from both datasets.

To sum it up, the diffraction detection algorithm comprises the following inputs and optional parameters and results in the following outputs.

Input:

- Pre-stack near-offset gathers processed in time (SEG-Y file) (either before or after multiple attenuation).
- Event attributes, including one-way traveltimes, from wavefront tracing (txt-file).

Optional:

- Account for amplitude polarity shifts.
- Add random (white) noise.
- Calculate semblance in a time window corresponding to the dominant wave period around the traveltimes obtained from NORSAR-3D.
- Choose a type of stack to be performed: Semblance stack or plain diffraction stack.
- Choose a type of event to be enhanced in the stack: Diffractions or reflections.

Output:

- Semblance plot.
- Full-wave Kirchhoff pre-stack depth migrated seismic sections.

The detection process is summarised in Figure 4.10, which displays the P-wave velocity model representing the Gullfaks synthetic data with accompanying image areas (Figure 4.10), used for wavefront tracing, and the final pre-stack depth migrated image using the full-wave data. Semblance plots are presented in the following chapter.
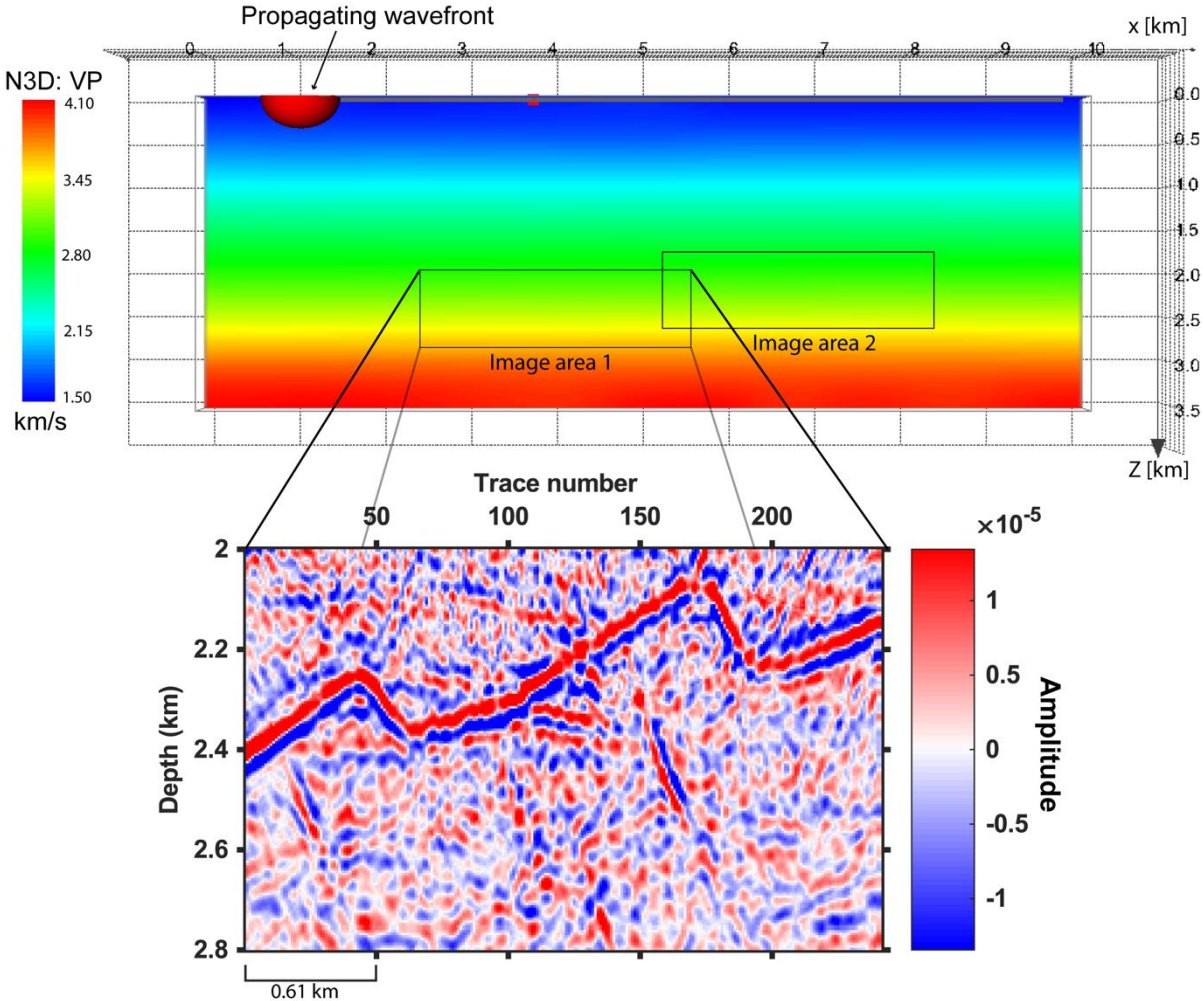
Figure 4.10: Gullfaks synthetic P-wave velocity model, with accompanying image areas, and the resulting full-wave pre-stack depth migrated section within image area 1, using the Gullfaks synthetic data.

5   Results

As described in the previous chapter, the workflows and methods are tested on the seismic datasets from the Gullfaks field and the Frøya High. This chapter is thus divided into sections concerning the various seismic datasets. Before presenting the results from the diffraction detection algorithm, the various input data are briefly examined. Uncertainties and potential causes of inaccuracies are described consecutively.

5.1   Gullfaks synthetic seismic data

As stated in section 2.1, the Gullfaks field is located on a NNE-SSW trending fault block in the Viking Graben in the northern North Sea. Two structurally contrasting segments make up the field; a deeply eroded horst complex of steep faults and elevated sub-horizontal layers in east and a domino-style fault block geometry in west (Fossen & Hesthammer, 1998). The synthetic dataset includes parts of this fault block geometry, which is studied with respect to diffraction detection. This section presents the seismic input data, the following areas (image area 1 and 2) and regions of interest and the results from running the diffraction detection algorithm.

5.1.1   Seismic input data

To be able to detect diffractions, it is essential to use data that has not been stacked nor migrated, i.e. pre-stack unmigrated seismic data. Pre-stack seismic data both before and after multiple attenuation is used as input to the diffraction detection algorithm (see section 4.3.9), in order to determine if the multiple attenuation process has a detrimental effect on the diffraction energy.

Figure 5.1 presents the Gullfaks pre-stack offset section prior to multiple attenuation. Distinctive diffraction events are observed from approximately 1.90 - 3.00 seconds (TWT). These hyperbola-like events typically originate where reflectors terminate.
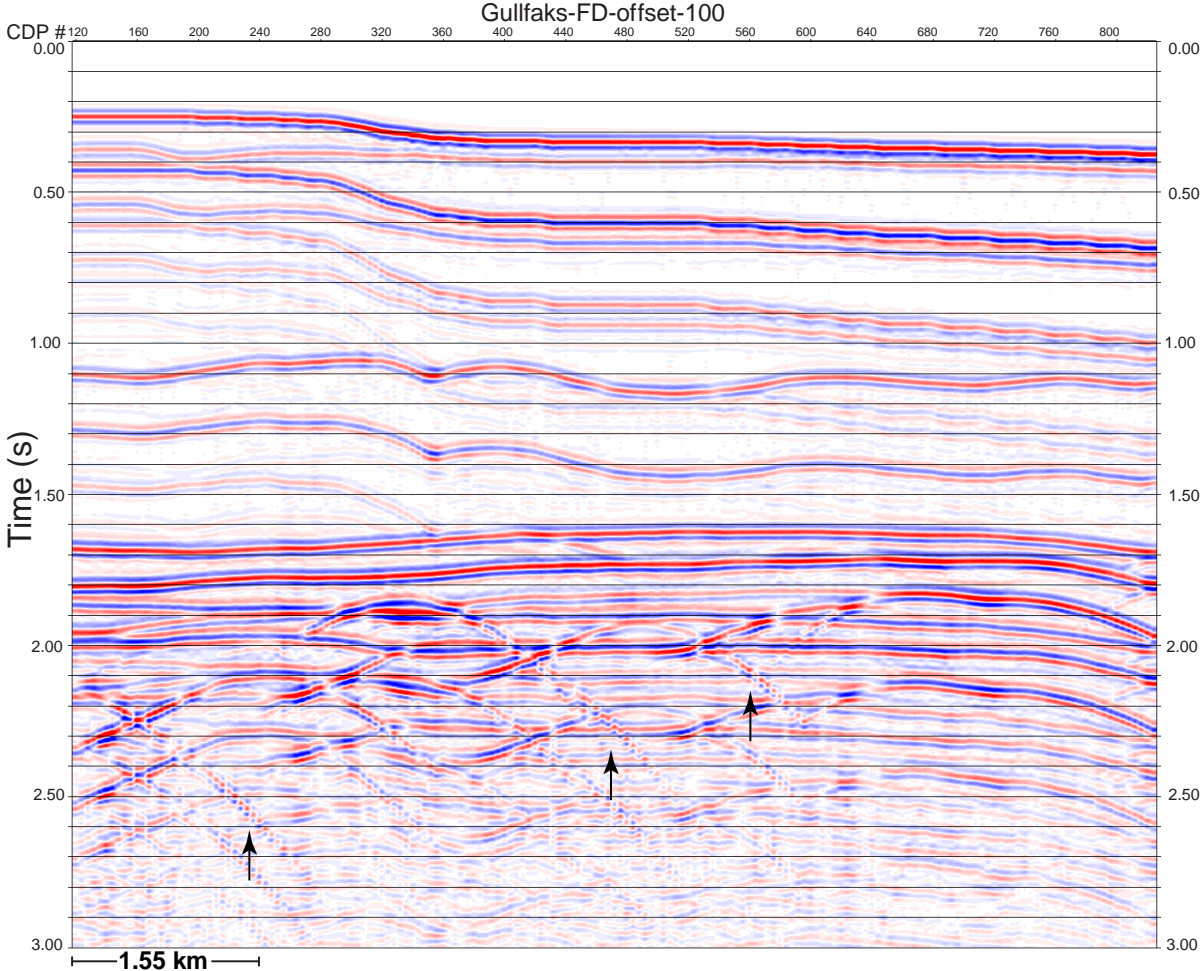
Figure 5.1: Gullfaks pre-stack synthetic input data, prior to multiple attenuation. This section depicts a near-offset section (100 m) in the time-domain. Multiple diffraction events dominate the section from approximately 1.90 - 3.00 seconds (TWT), some of which are marked by arrows.

Figure 5.2 presents the Gullfaks pre-stack offset section after performing a multiple attenuation process. The diffraction hyperbolas are still present in this section, however possibly weaker than those in the non-multiple-attenuated section (Figure 5.1). Both sections are used as input to the algorithm, in order to quantify to which extent diffractions appear in the seismic data.
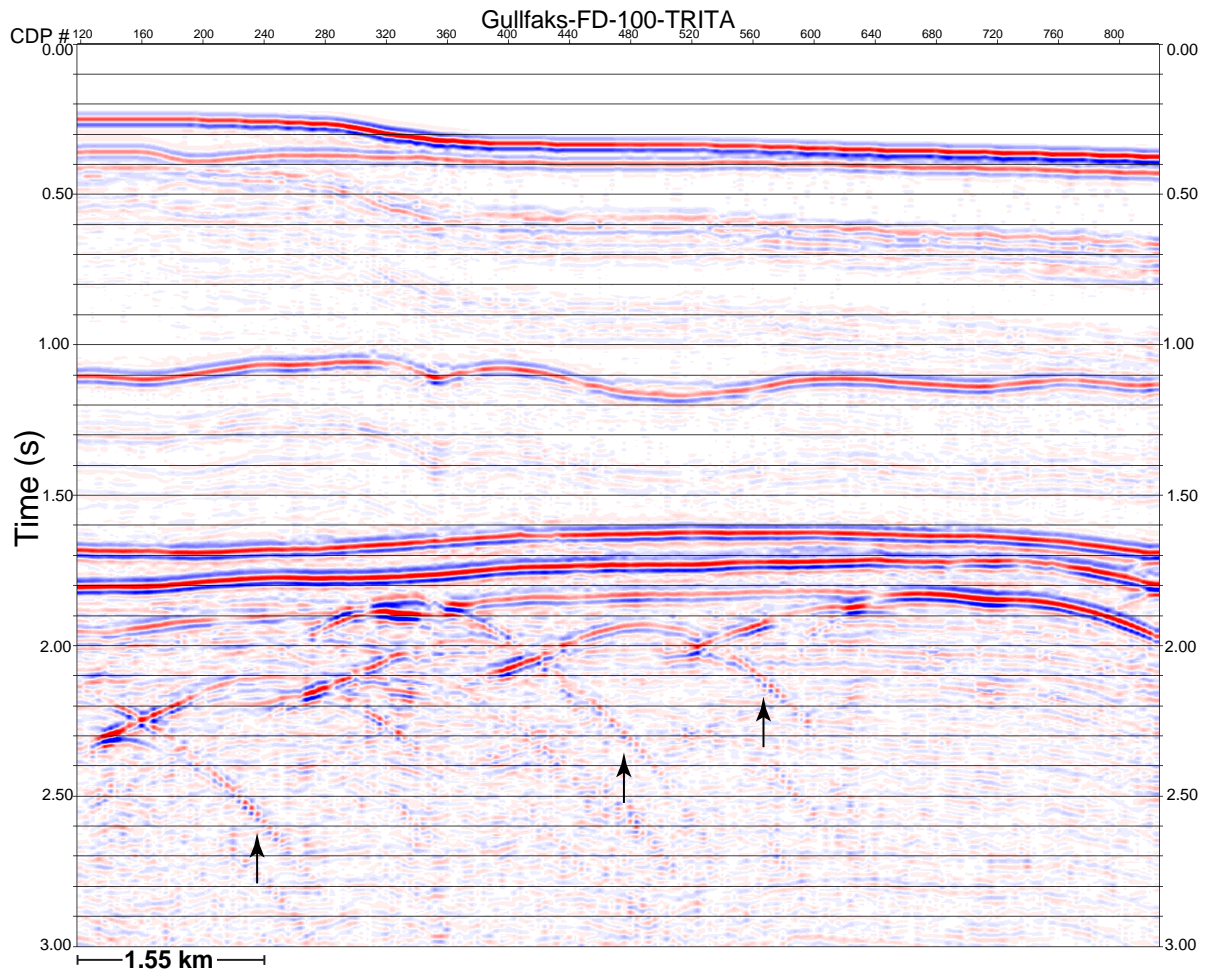
Figure 5.2: Gullfaks pre-stack synthetic input data, after performing multiple attenuation. This section depicts a near-offset section (100 m) in the time-domain. Diffraction events are clearly visible from approximately 1.90 - 3.00 seconds (TWT), some of which are marked by arrows.

5.1.2   Depth migrated section and image areas

Using the Gullfaks synthetic dataset, I have performed a 3D Kirchhoff pre-stack depth migration process in Geocluster. The result is presented in Figure 5.3. The undulating reflector, representing the Top Cook formation, is the seismic response of a domino-style fault block geometry which is representative of the Gullfaks field.
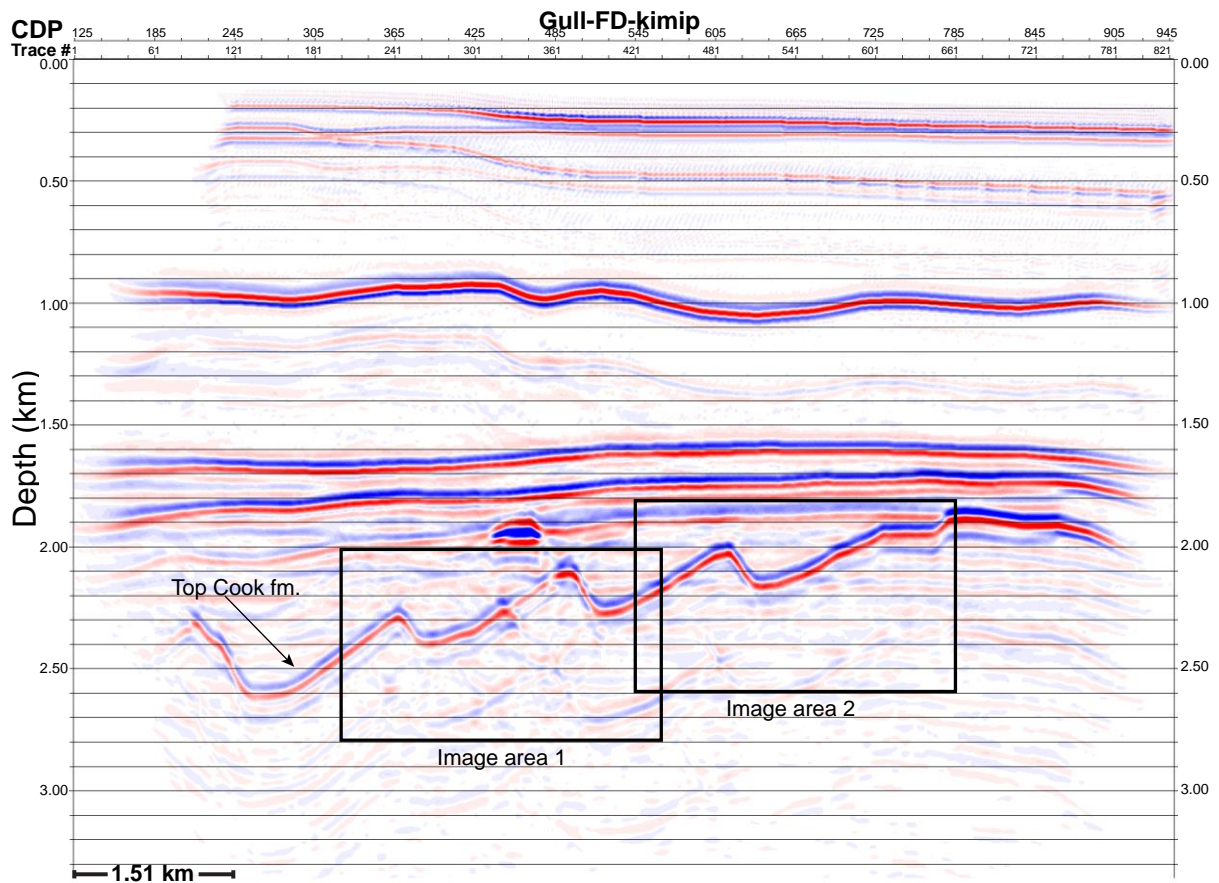
Figure 5.3: The Gullfaks synthetic seismic dataset after performing the 3D Kirchhoff pre-stack depth migration in Geocluster. The vertical axis represents subsurface depth in km (from 0-3.30 km), while the horizontal axis, with an approximate extent of 10 km, displays CDP and trace numbers. Image area 1 and 2 are marked within the rectangles, defining the receiver positions outlined in Table 5.1 and Table 5.2. The Top Cook formation is marked with an arrow.

As the diffracted energy emitted from the discontinuities in the subsurface is subject to further analysis, the image areas are naturally positioned around fault structures. Image area 1, as defined in Table 5.1, covers depths from 2-2.8 km with a horizontal extent of 3 km. The synthetic dataset in this area images part of three domino-style fault blocks, where diffracted energy is expected to be found adjacent to the structural discontinuities. Image area 2, defined in Table 5.2, covers depths from 1.8-2.6 km and has a horizontal extent of 3 km. This section includes parts of two fault blocks.

Table 5.1: Image area 1, associated with the Gullfaks synthetic data.

IMAGE AREA 1 – GULLFAKS SYNTHETIC DATA				
SHOTS:	**START**	**INCREMENT**	**NODES**	**UNIT**
X-DIR.:	1.0	0.040	151	km
Y-DIR.:	5.0	0.040	1	km
DEPTH:	0.010	0.040	1	km
RECEIVERS:	**START**	**INCREMENT**	**NODES**	**UNIT**
X-DIR.:	2.5	0.0125	241	km
Y-DIR.:	5.0	0.010	1	km
DEPTH:	2.0	0.005	161	km

Table 5.2: Image area 2, associated with the Gullfaks synthetic data.

IMAGE AREA 2 – GULLFAKS SYNTHETIC DATA				
SHOTS:	**START**	**INCREMENT**	**NODES**	**UNIT**
X-DIR.:	3.750	0.040	151	km
Y-DIR.:	5.0	0.040	1	km
DEPTH:	0.010	0.040	1	km
RECEIVERS:	**START**	**INCREMENT**	**NODES**	**UNIT**
X-DIR.:	5.250	0.0125	241	km
Y-DIR.:	5.0	0.010	1	km
DEPTH:	1.8	0.005	161	km

5.1.3   Identifying regions where diffractions are likely to occur

As mentioned in section 4.3.9, the multiple attenuation process executed during seismic processing may also influence and possibly attenuate the diffracted energy. Thus, both multiple-attenuated and non-multiple-attenuated pre-stack seismic data from the Gullfaks synthetic dataset are used as input to the diffraction detection algorithm in order to make sure that no vital information is lost during processing.

In order to interpret the results obtained from the semblance calculations, it is important to identify regions where diffractions are likely to occur. This allows to quantify to what extent diffractions appear in the recorded seismic data. Target discontinuities are selected by studying Kirchhoff pre-stack depth migration sections. The outputs from running the

Kirchhoff pre-stack depth migration option of the algorithm in image area 1, by using both non-multiple-attenuated and multiple-attenuated seismic data, are presented in Figure 5.4.

Figure 5.4: Kirchhoff PSDM-sections generated using image area 1 (Gullfaks synthetic dataset). (a) Depth migrated section obtained using seismic data not corrected for multiples. (b) Depth migrated section obtained using multiple-attenuated seismic data. The events marked "1" and "2" represent reflections from fault planes, while "3" and "4" represent the multiples from these reflections.

Figure 5.4a illustrates a depth-migrated section obtained using seismic data from the Gullfaks field that are not corrected for multiples, while Figure 5.4b depicts the corresponding depth-

migrated section obtained using multiple-attenuated data. By studying these full-wave depth-migrated sections, two fault planes, marked "1" and "2", stand out and are interpreted as major discontinuities. Notice how the multiples from these fault planes, marked "3" and "4", are visible in both depth-migrated sections. These multiples are translated horizontally, depending on the inclination of the fault plane. These steep-dip multiples have not been attenuated well enough during the multiple attenuation process and are thus also observed in the multiple-attenuated section (Figure 5.4b). As a result, there is a probability that diffractions can be found in these regions when running the semblance summation option of the algorithm.

The results from running the Kirchhoff pre-stack depth migration option for image area 2, using both non-multiple-attenuated and multiple-attenuated seismic data, are presented in Figure 5.5. The most prominent discontinuities are marked "5" and "7", respectively illustrating a fault zone between two adjacent fault blocks and a minor fault adjacent to the overlying Base Cretaceous layer. The region marked "6" represents a multiple from the overlying primary reflection of a fault plane (marked "5"). This multiple is prominent in the multiple-attenuated section (Figure 5.5b) as well, despite the multiple attenuation process the input seismic data has gone through. As with the multiples marked "3" and "4" in Figure 5.4, it is likely that semblance peak values are found around the multiple marked "6" when running the semblance calculation.
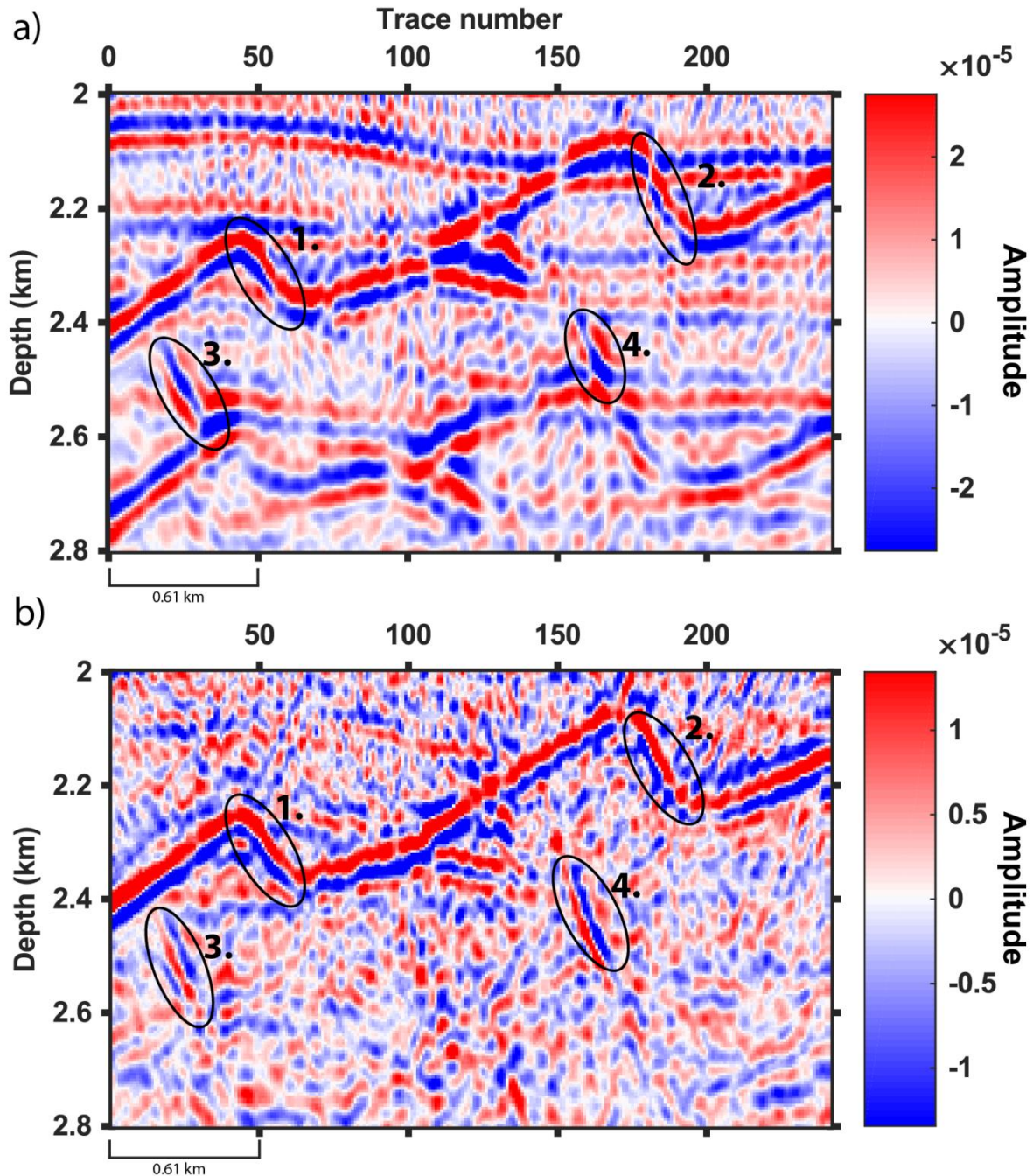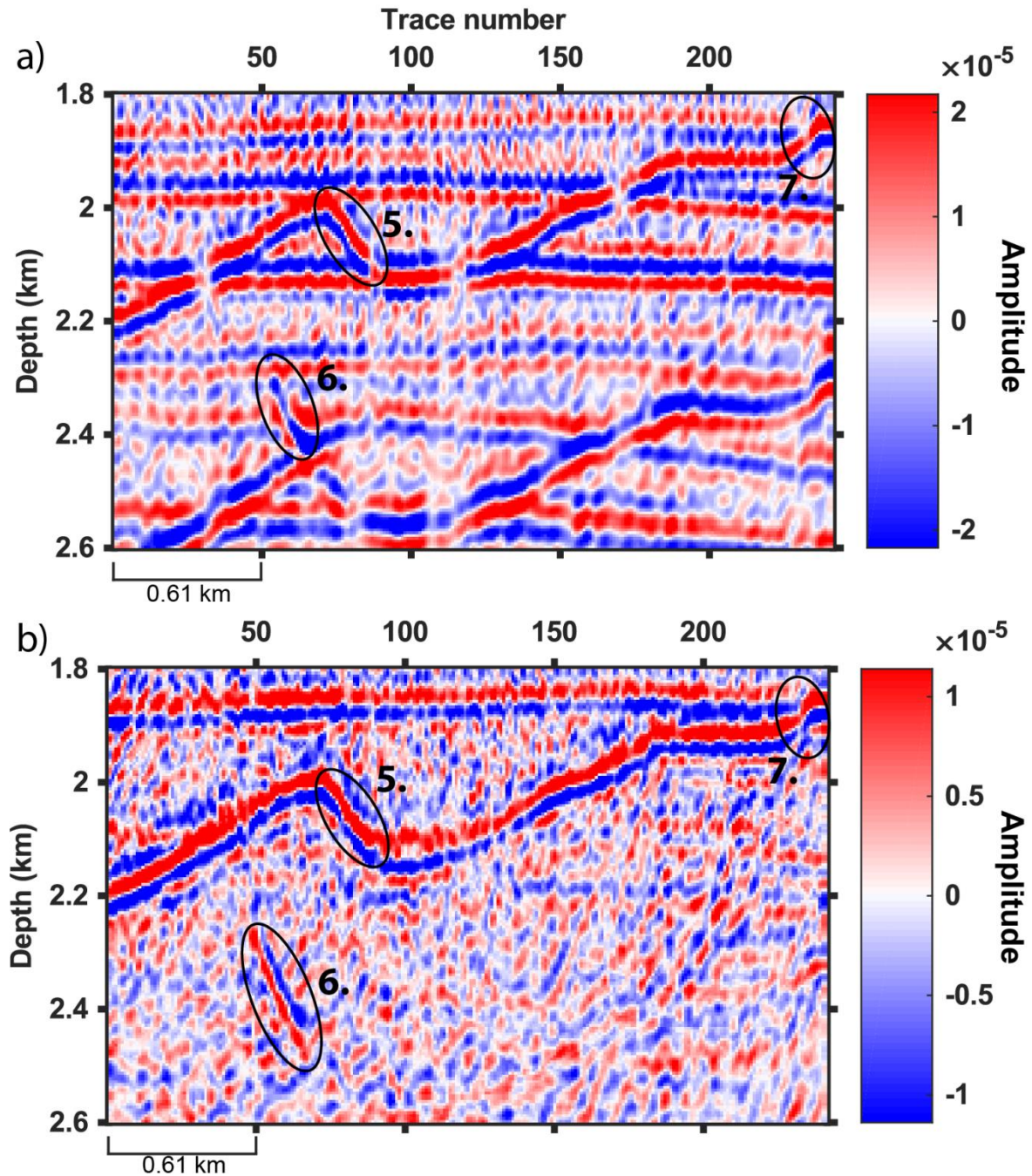
Figure 5.5: Kirchhoff PSDM-sections generated using image area 1 (Gullfaks synthetic dataset). (a) Depth-migrated section obtained using seismic data not corrected for multiples. (b) Depth-migrated section obtained using multiple-attenuated seismic data. The most prominent discontinuities are marked "5" and "7", where the multiple of "5" is marked "6".

By running the Kirchhoff pre-stack depth migration option of the algorithm on the synthetic seismic dataset within image area 1 and 2 (Figure 5.4 – 5.5), on both multiple-attenuated and non-multiple-attenuated seismic data, we observe that noise and multiples have successfully been removed. The exception is the appearance of multiples originating from fault planes.

After identifying regions where diffractions are likely to occur, semblance calculations are carried out on these sections in order to determine if the applied method works. However, as the multiple attenuation process may also attenuate diffracted energy, semblance calculations are generated from both the multiple-attenuated and non-multiple-attenuated seismic data from image area 1, in order to see if there are any distinguishable differences between the two. The results of this process are presented in Figure 5.6. Semblance is computed in a time window around the potential diffraction traveltime curves corresponding to a dominant frequency of 20 Hz, in order to increase the possibility of detecting a diffraction curve (see section 4.3.9). Arrows pointing upwards symbolises regions where the semblance peak value in the multiple-attenuated data (Figure 5.6b) is higher compared to in the non-multiple-attenuated data, while the arrow pointing downwards illustrates a zone where the magnitude of semblance has decreased after multiple attenuation. Moreover, the semblance plot obtained using the multiple-attenuated data within image area 1 (Figure 5.6b) is observed to have higher values overall than the plot obtained for the non-multiple-attenuated data. This possibly indicates that the multiple attenuation process does not attenuate the diffracted energy, but rather improves its detectability by improving the signal-to-noise ratio of diffractions. As no vital information about diffracted waves seems to be lost during multiple attenuation of the Gullfaks synthetic dataset, semblance calculation is only carried out on the multiple-attenuated data from image area 2.
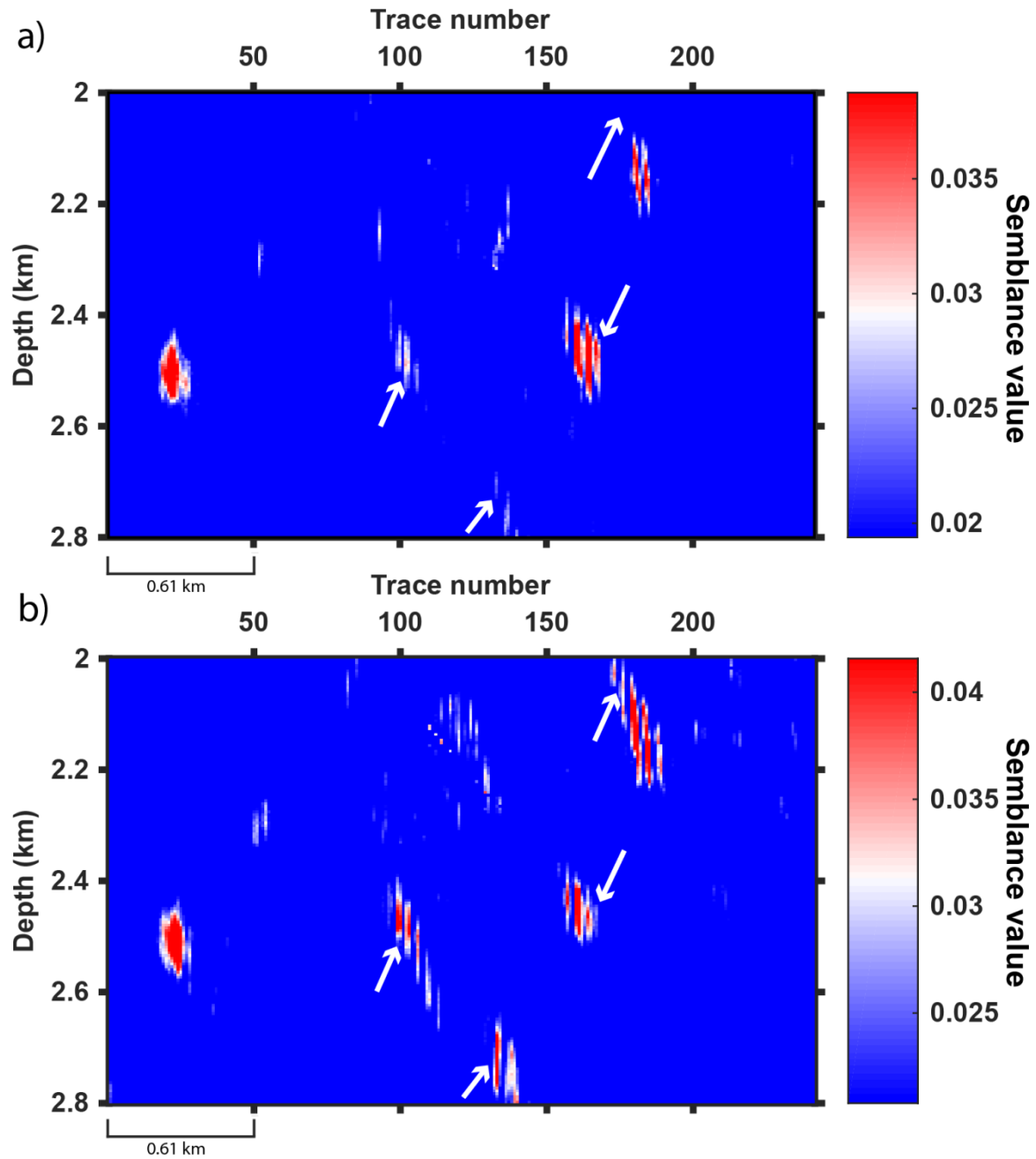
Figure 5.6: Semblance plots generated using image area 1 (Gullfaks synthetic dataset), using a) non-multiple-attenuated data and b) multiple-attenuated data. Semblance is computed in a time window around the potential diffraction traveltime curves corresponding to a dominant frequency of 20 Hz. Arrows are pointing to regions where the detected semblance peak values differ between the two datasets.

5.1.4   Comparing semblance plots to full-wave depth-migrated data

In order to fully understand the results obtained from running semblance calculations on the different image areas, a comparison between the semblance plots and the full-wave depth migrated data is made. By doing so, we might be able to determine from which structural

features the diffracted waves originate from. Furthermore, comparing the different plots might reveal whether the applied methods are successful, i.e., if diffracted energy is systematically detected in the predicted regions.

Image area 1

The results from running the different options of the algorithm using image area 1 are presented in Figure 5.7. The semblance plot is generated using a time window corresponding to a dominant frequency of 20 Hz.

In Figure 5.7, the most accentuated semblance peak values, marked 1-5 in the semblance plot (Figure 5.7a), are mapped to their equivalent positions within the full-wave depth migrated section (Figure 5.7b), marked 1'-5'. This facilitates the comparison of the result from the semblance plot to the associated geological features. Image area 1 contains parts of three fault blocks and consequently two fault planes. Thus, as described in section 5.1.3, semblance peak values are expected to be found adjacent to these fault planes and their multiples (see Figure 5.4). The arrows in Figure 5.7b point to these target regions. Looking at the semblance plot (Figure 5.7a), we observe that this expectation is fulfilled, as positive semblance peak values are found in these regions (marked 1', 4' and 5'). The exception is the fault zone marked 6', where only minor semblance peak values are observed in the semblance plot (marked with an arrow in Figure 5.7a). The semblance peak values around the multiple of this fault zone (marked 1) are in fact higher than around the primary reflection of the fault zone itself. Why a fault plane, such as the one marked 5', is surrounded by diffracted energy while another is not, is a subject for further discussion and might indicate uncertainties related to the quality of the input data and/or the quality of the applied methods.

Figure 5.7: Results obtained from image area 1 (Gullfaks synthetic data). a) Semblance plot obtained using a time window corresponding to a dominant frequency of 20 Hz. The most prominent semblance peak values are marked 1-5, while the arrow points to a region where higher semblance peak values were expected. b) Full-wave depth migrated section, whereas the results from the semblance plot (a) are mapped to their equivalent positions, marked 1'-5'. Arrows point to regions where diffracted waves are expected to be found (see Figure 5.4).

However, two prominent regions remain to be addressed, marked 2 and 3. When determining regions in image area 1 where diffractions are likely to occur, no anticipation was made

related to these regions – as there are no reflectors below the Top Cook reflector in the synthetic model. Even if the detected energy is extremely weak, the degree of semblance may be high as the semblance method only measures the degree of similarity and does not distinguish between weak or strong detected signals. This contributes to the uncertainty of using this method, as one might obtain values that are hard to explain using the geological models. However, region 3 appears equally laterally translated as the multiple of region 4' is with regards to the primary reflection of the fault plane marked 5'. This observation makes it likely that the detected diffraction energy in this region represents a third multiple originating from the fault marked 5'. No apparent discontinuity in this image area seems to clarify the origin of the detected diffraction energy in region 2'. A prominent flat spot is however observed right above the boundary of image area 1 (Figure 5.3), positioned approximately 600 m above region 2'. It is thus likely that the detected semblance peak values in region 2' originate from a multiple of this flat spot, as its edges or abrupt changes in seismic impedance contrasts may emit diffracted waves.

Nonetheless, the results obtained from image area 1 indicate that diffracted energy is indeed identified in regions where diffractions are likely to occur, however with some related uncertainties regarding the origin of some of the detected semblance peak values.

Image area 2

Further testing of the applied methods is performed, now using image area 2 from the synthetic Gullfaks dataset. The results from image area 2 are presented in Figure 5.8. The semblance plot is generated using a time window corresponding to a dominant frequency of 20 Hz. As with the results from image area 1 (Figure 5.7), the most prominent semblance peak values from the semblance plot (Figure 5.8a) are numbered and mapped to their equivalent positions within the full-wave depth migrated image (Figure 5.8b). This plot contains a higher number of semblance peak values compared to the semblance plot from image area 1 (Figure 5.7a), which indicates a greater number of detected diffracted waves in this image area.
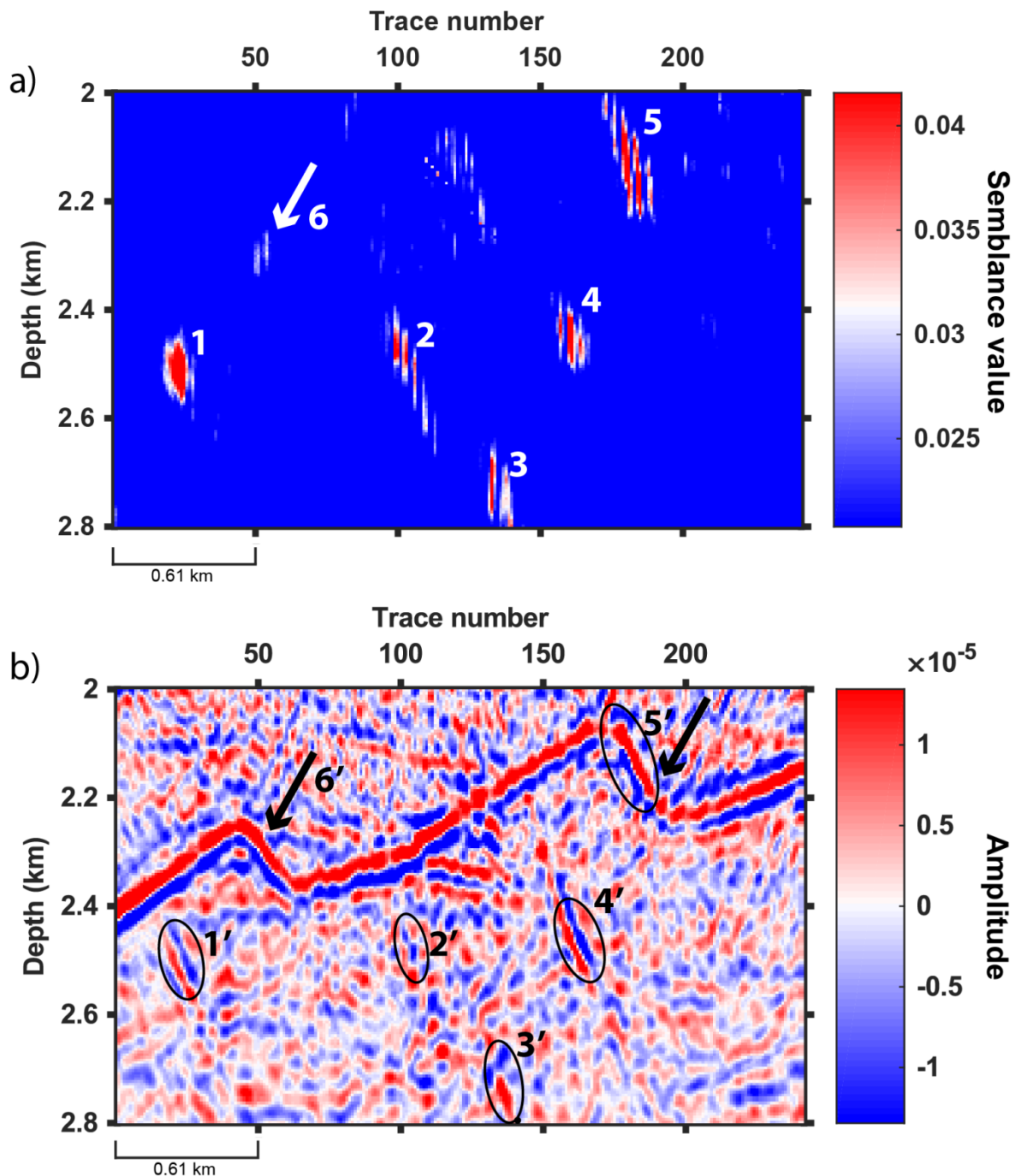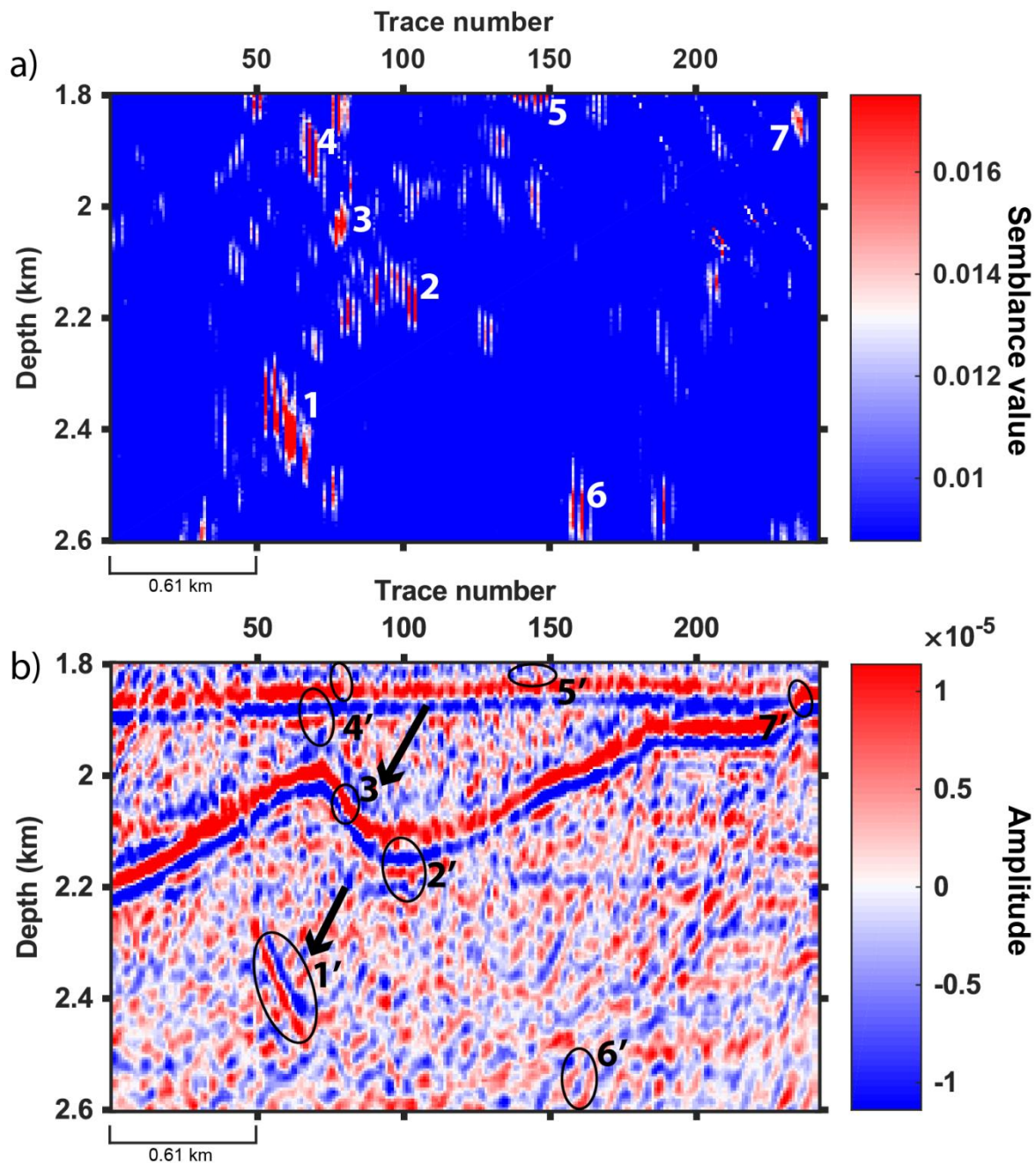
Figure 5.8: Results obtained from image area 2 (Gullfaks synthetic data). a) Semblance plot obtained using a time window corresponding to a dominant frequency of 20 Hz. The most prominent semblance peak values are marked by 1-7. b) Full-wave depth migrated section, whereas the results from the semblance plot (a) are mapped to their equivalent positions, marked by 1'-7'. Arrows point to regions where diffracted waves are expected to be found (see Figure 5.5).

The arrows in Figure 5.8b point to regions where diffracted waves are expected to be found, as discussed in section 5.1.3. Region 1 (Figure 5.8a) covers the densest semblance peak value distribution. This region correlates with the multiple of the overlying primary reflection of a fault plane. This fulfils the anticipation of detecting diffractions in the region around the

observed multiple. The semblance peak values represented by 2 and 3 are found in relation to the primary reflection of a fault plane. This fault plane was earlier identified as a region where diffractions are likely to be found. The semblance peak values in region 4 are however placed a few hundred metres above the target fault plane, indicating that these values are not related to the target fault plane. No structural discontinuities are observed in the regions marked 5' and 6' (Figure 5.8b), thus the interpretation of why those regions stand out on the semblance plot remain uncertain. Semblance peak values are detected in the region marked 7, which meets the expectation that results will be found around the minor fault in this region. Finally, semblance peak values are found in all three regions of interest in image area 2. The degree of semblance also seems to be higher in these regions compared to the uninterpretable semblance peak values in other regions.

5.2   Frøya High real seismic data

As mentioned in section 4.2, the seismic section from the Frøya High is subject to multiple WNW-trending normal faults. Diffracted energy is assumed to be found adjacent to these fault zones. This section presents the seismic input data, the following area of interest and the results from running the diffraction detection algorithm.

5.2.1   Seismic input data

As with the Gullfaks synthetic data, seismic data from the Frøya High both before and after multiple attenuation are used as input to the diffraction detection algorithm. Two output SEG-Y files (Figure 5.9 and Figure 5.10) are exported from Geocluster after completing pre-processing. The result from running the pre-processing process on the Frøya High raw seismic data without correcting for multiples is presented in Figure 5.9, while Figure 5.10 presents the multiple-attenuated section. Both sections display an offset section (240 m) from 0.00 - 3.00 seconds TWT. The horizontal axis shows CDP-numbers from 177 - 1441, which corresponds to a horizontal extent of 15.8 km. An area of interest is highlighted and enlarged for better visualisation of three prominent fault zones (i-iii) and a feature that appears to be a depression on the ocean floor (iv). These structural features are subject to further analysis. Notice the distinctive diffraction hyperbola, most noticeable in the multiple-attenuated section (Figure 5.10), that appears in relation to the ocean floor depression.
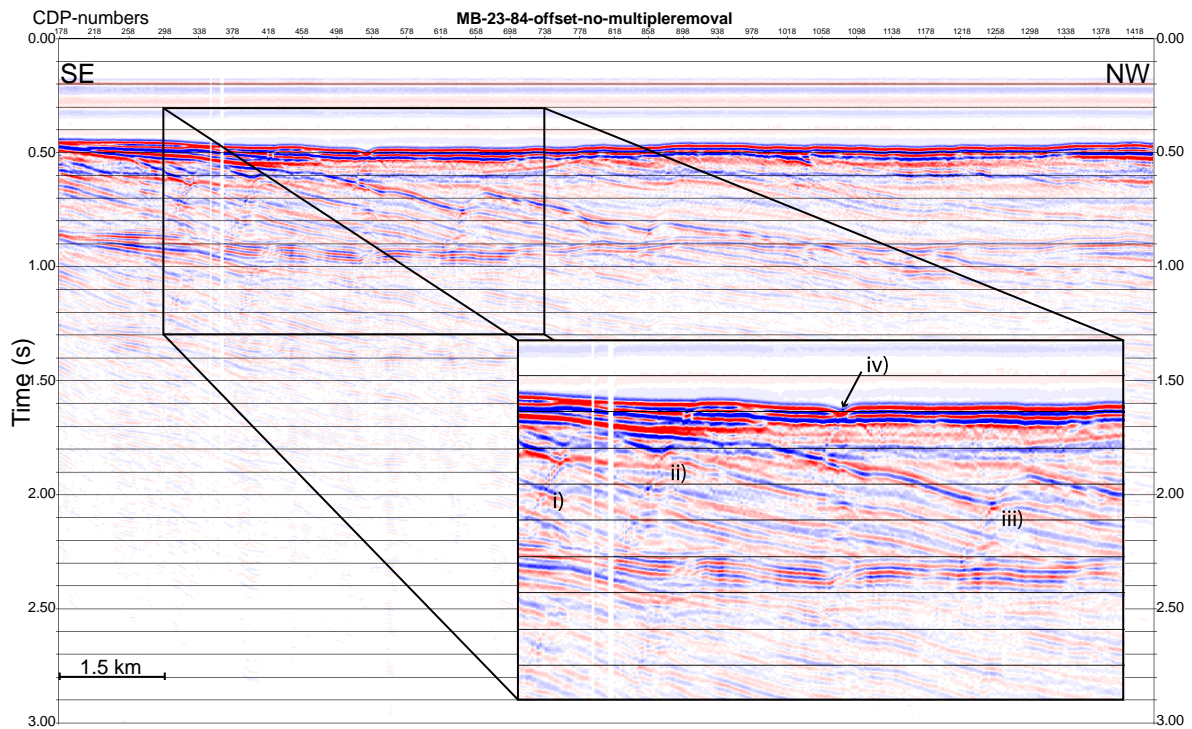
Figure 5.9: Frøya High pre-stack input data, prior to multiple attenuation. This section is processed in two-way time and depicts a near-offset (240 m) gather section. A target area for further analysis is highlighted and enlarged, illustrating three fault zones marked i), ii) and iii) respectively. A depression on the ocean floor is marked iv).

Figure 5.10: Frøya High pre-stack input data, after performing multiple attenuation. This section is processed in two-way time and depicts a near-offset (240 m) gather section. A target area for further analysis is highlighted and enlarged, illustrating three fault zones marked i), ii) and iii) respectively. A depres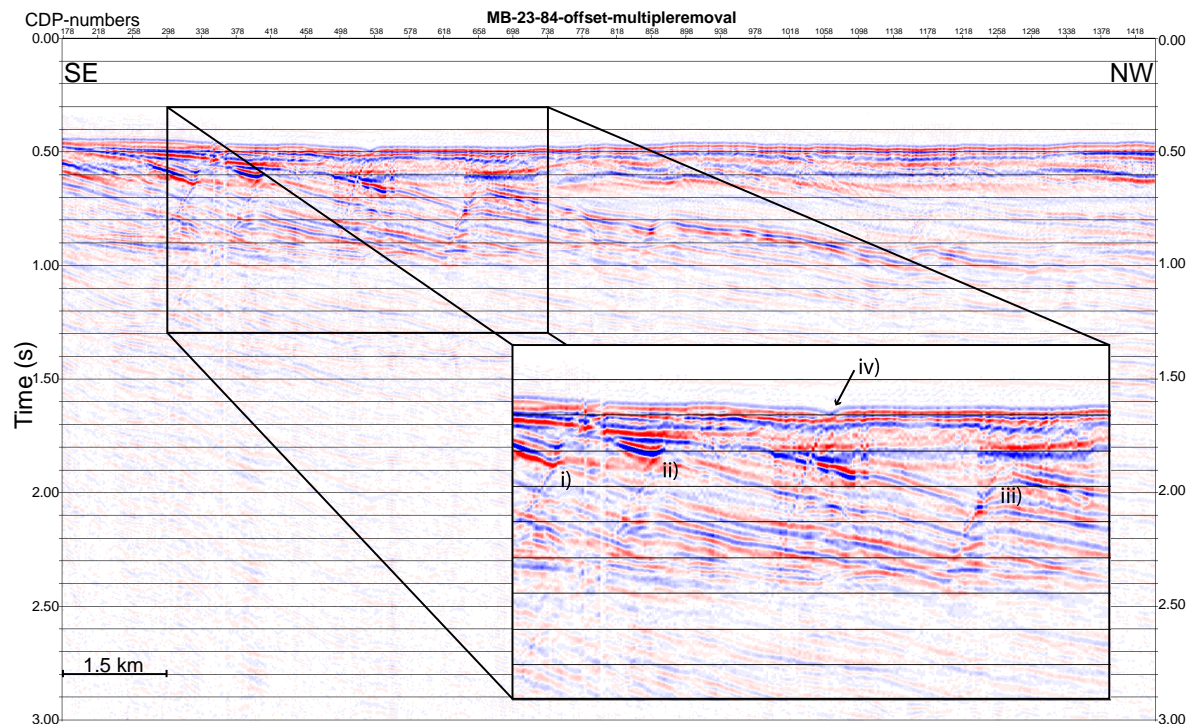sion on the ocean floor is marked iv). Notice the distinctive diffraction hyperbola originating from the ocean floor depression.

5.2.2   Image area

Image areas for diffraction analysis need to be defined prior to executing the diffraction detection algorithm. In this respect, it is noted that no sufficient result from depth migration in Geocluster was obtained for the real seismic data (see section 4.3.6 and 4.3.7). The reason is probably the lack of an accurate depth velocity model. As a consequence, the image area (Table 5.3) is defined by using the seismic section in the time-domain prior to depth migration (Figure 5.9). The lateral and vertical range of the image were thus set large enough to compensate for the displacement of reflectors during depth migration, to ensure that the target discontinuities were covered.

Image area 3, as defined in Table 5.3, covers depths from 0.250-1.250 km with a horizontal extent of 5.5 km. The real seismic data in this area images parts of four fault blocks (see Figure 5.9), where diffracted energy is expected to be found adjacent to the fault zones.

Table 5.3: Image area 3, associated with line MB-23-84 acquired from the Frøya High.

IMAGE AREA 3 – REAL SEISMIC DATA – LINE MB-23-84				
SHOTS:	**START**	**INCREMENT**	**NODES**	**UNIT**
X-DIR.:	3.125	0.040	157	km
Y-DIR.:	0.500	0.040	1	km
DEPTH:	0.001	0.040	1	km
RECEIVERS:	**START**	**INCREMENT**	**NODES**	**UNIT**
X-DIR.:	3.725	0.0125	441	km
Y-DIR.:	0.500	0.010	1	km
DEPTH:	0.250	0.005	201	km

5.2.3   Identifying regions where diffractions are likely to occur

Identifying regions where diffractions are likely to occur is vital in order to interpret the results obtained from the subsequent semblance calculations. As already stated, this allows us to quantify to what extent the results of the semblance analysis are consistent with recorded seismic data. The results of running the Kirchhoff pre-stack depth migrated process of the algorithm, using seismic data before and after multiple attenuation, are therefore examined. The results are presented in Figure 5.11.
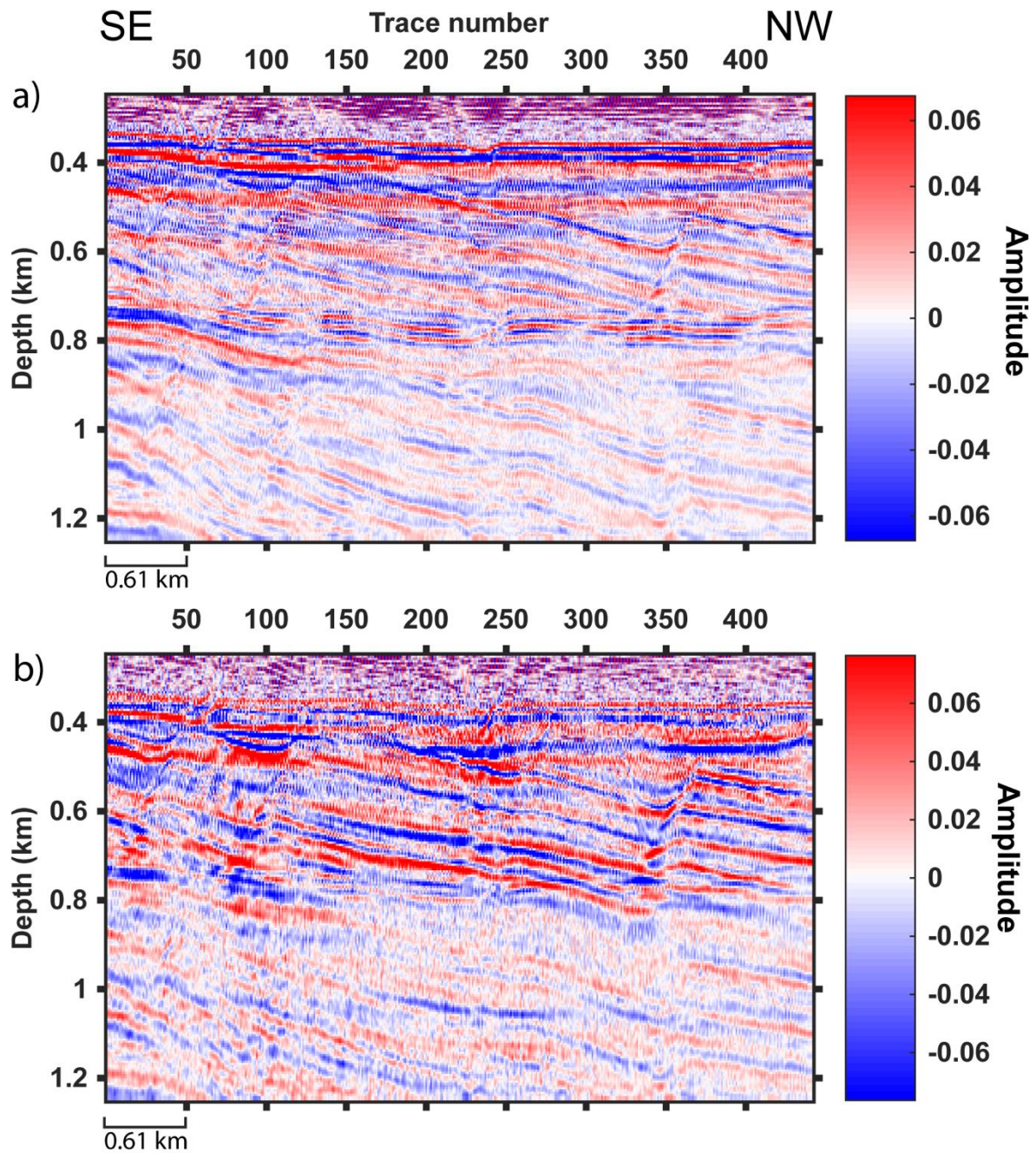
Figure 5.11: Kirchhoff pre-stack depth migrated sections of the Frøya High real seismic data within image area 3. (a) Depth migrated section obtained using seismic data that are not corrected for multiples. (b) Depth migrated section obtained using multiple-attenuated seismic data.

Figure 5.11a presents the depth migrated result using the seismic data within image area 3 prior to multiple attenuation, while Figure 5.11b displays the multiple-attenuated depth migrated result. Despite the multiples in Figure 5.11a, it is easier to grasp the structural configuration of the subsurface in this section, compared to the multiple-attenuated section in Figure 5.11b. Particularly the ocean floor depression between trace number 200-250, at approximately 0.35 km depth, is much more apparent in the section prior to multiple

63

attenuation (Figure 5.11a). Consequently, subsequent semblance calculations are carried out on the depth migration section prior to multiple attenuation (Figure 5.11a) – as its structural features are more easily perceived compared to the multiple-attenuated section.
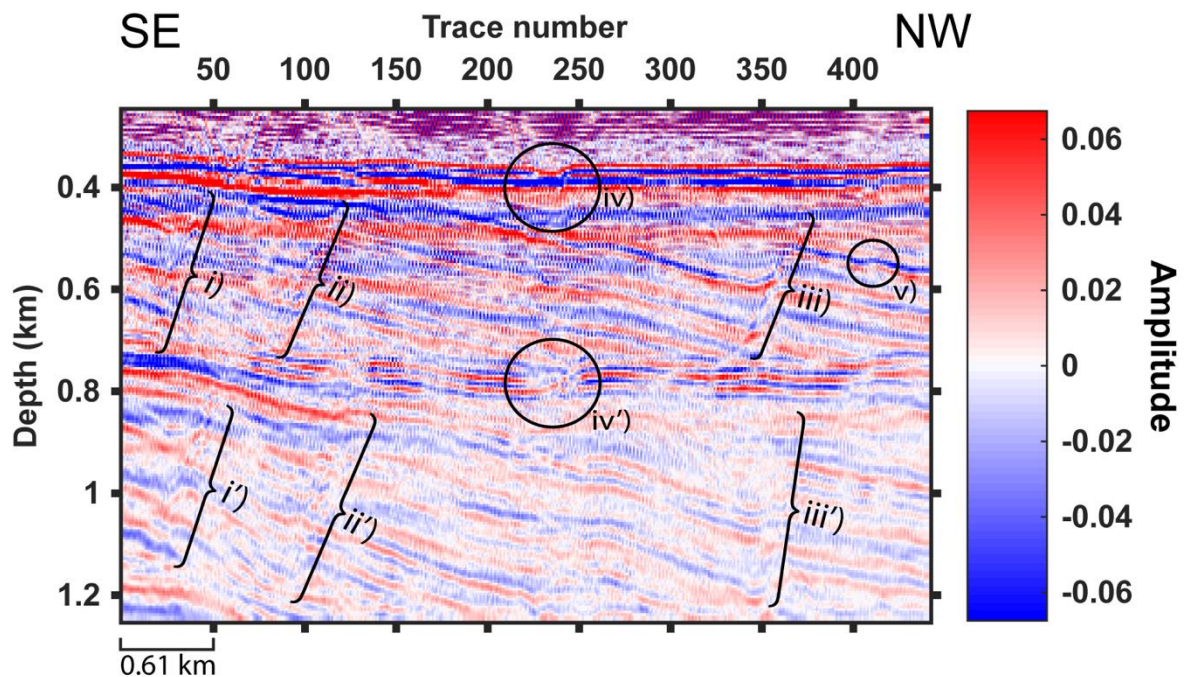
Figure 5.12: Regions of interest within image area 3 using the Frøya High depth migrated dataset prior to multiple attenuation. Fault zones are marked i), ii) and iii), with corresponding multiples marked i'), ii') and iii') respectively. A depression in the ocean floor and its corresponding multiple is marked iv) and iv') respectively. A minor fault is marked v).

Nevertheless, regions of interest must be identified prior to analysing the results obtained from semblance calculations. The seismic section of Figure 5.12 is equivalent to that of Figure 5.11a, however, this time illustrating regions of interest. Three WNW-trending normal faults, marked i-iii), including their multiples, marked i'-iii'), define the primary regions of interest as diffracted waves are expected to be found in relation to these. A feature that appears to be a depression in the ocean floor is included as a region of interest, marked iv). A rather distinctive diffraction hyperbola originating from this depression is observed prior to pre-stack depth migration (Figure 5.10), which makes it plausible that diffractions will be detected around this region in the subsequent semblance calculation procedure. The multiple of this ocean floor depression (iv') also qualifies as a region of interest. What appears to be a minor fault, marked v) in Figure 5.12, might be the source of diffracted energy and is thus also marked as a region of interest.

5.2.4   Comparing semblance plots to full-wave depth migrated data

A comparison is made between the semblance plot and the full-wave depth migrated section in order to fully understand the results obtained from running semblance calculations within image area. By doing so, we might reveal whether the applied methods are successful or not, i.e. if diffracted energy is systematically detected in the predicted regions. The comparison is presented in Figure 5.13.

More semblance peak values are scattered around the plot compared to those obtained from the Gullfaks synthetic dataset which were mainly focused around the main target regions. In order to interpret the results, the most prominent semblance peak values are marked with circles in Figure 5.13a, and mapped to their equivalent positions in the depth migrated section (Figure 5.13b). These regions are numbered i-vi). Semblance peak values detected above 0.3 km depth are ignored for now, as this area represents the water column. The presence of values in this area is further discussed in chapter 6. Ideally, no semblance peak values should be detected shallower than the depth of the ocean floor. Notice how almost no diffractions are detected below a depth of 0.8 km (Figure 5.13a), ruling out detections related to multiples.

Semblance peak values within region i), ii), iv) and v) are detected and observed adjacent to the three major normal faults within this image area (Figure 5.13b). As described in section 5.2.3, semblance peak values are expected to be found in or around these regions. The diffracted energy observed in region vi) might originate from the minor fault/fracture marked by v) in Figure 5.12. Interpreting the structural source of diffractions identified in region iii) and vii) is more difficult, as no prominent discontinuities are observed in the depth migrated section in these regions. A minor semblance peak value is observed in relation to the ocean floor depression, but the value is quite indistinct compared to the semblance peak values from fault zones.

An attempt to quality control the results obtained within image area 3 is made and discussed in the following chapter. This is performed in order to evaluate the functionality of the algorithm.
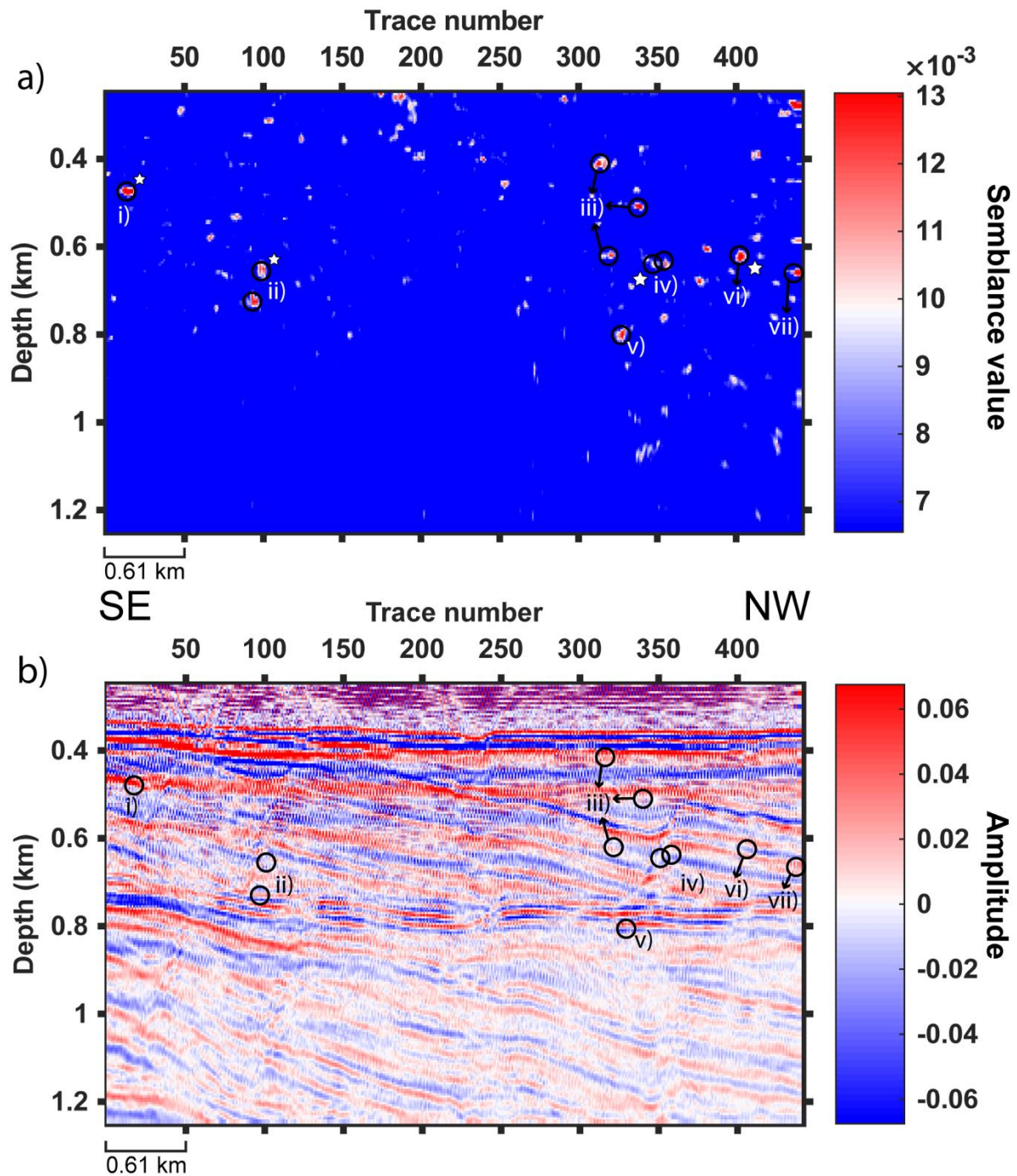
Figure 5.13: Results obtained from image area 3 (real seismic data from the Frøya High). a) Semblance plot obtained using a time window corresponding to a dominant frequency of 20 Hz. The most prominent semblance peak values are marked with circles and are numbered i-vii). Semblance peak values marked with a star (in region i, ii, iv and vi) are used for quality control in the subsequent chapter. b) Full-wave depth migrated section, whereas the results from the semblance plot (a) are transposed to their equivalent positions, marked with circles.

6 Discussion

The results and following observations made by testing the diffraction detection algorithm are analysed and discussed in this chapter, with the purpose of determining how well the algorithm performs. The value of performing this study lies in the experience and knowledge gained when analysing the precision and limitations of the applied methods, using both synthetic and real seismic data. Understanding the physical constraints on diffraction detection is important prior to further development of the method. Consequently, factors that influence the diffraction detection are discussed and evaluated in this chapter. Finally, an analysis of whether future development of the method is recommended or not is provided.

6.1 Factors influencing the diffraction detection

Several factors influence the output results which need to be addressed in order to evaluate the functionality of the diffraction detection algorithm.

6.1.1 Velocity smoothing

In order to pursue a ray-based tomography method, we are dependent on a robust velocity model with a certain degree of smoothness (see section 4.3.5). The smoothing process performed in NORSAR-3D alters the velocity models, preventing the original traveltime between all pairs of points in the model from being preserved (Vinje et al., 2013). This results in traveltime errors, which are particularly significant at structural discontinuities with large offsets in the velocity models. The Kirchhoff pre-stack depth migrated seismic sections are consequently affected by these errors, slightly reducing its accuracy and causing a depth shift in the resulting sections. Nevertheless, the diffraction detection algorithm is quite robust when it comes to detecting diffractions, so we will generally still be able to detect diffraction events despite a smoothed velocity model. A smoothed model does however affect the positioning of these detected events in the resulting semblance plots. Thus, there is no reason to believe that the smoothing performed in NORSAR-3D will affect diffraction detectability, other than the fact that it might result in a depth shift within the migrated sections.

6.1.2 Velocity errors

The effects an inaccurate velocity model has on diffraction imaging remain an important issue. The velocity model related to the Frøya High real seismic data, obtained from processing made by Veritas DCG, has not been inspected in terms of quality as this is a task

beyond the scope of this study. No information on how the velocity model was made is provided. Velocity estimations are challenging when dealing with structurally complex media, thus there might be a risk of undetected errors within the given velocity model.

For example, if the velocity model is based on a one-dimensional isotropic assumption (velocities varying only as a function of depth), the resulting spatial position of the detected diffractions may be significantly affected. This is due to the fact that the migration algorithm require the parameters to be in their true subsurface locations (Jones, 2014), which would not be true in media with lateral velocity changes. Such lateral changes are clearly present in the synthetic and real seismic data examples of this study. An inaccurate input velocity model for depth migration will thus affect the positioning of reflections and diffractions (Pon & Lines, 2005). However, as with velocity smoothing, this solely affects the spatial positioning of the detected diffractions, and not our capability of detecting them. An accurate velocity model is however vital, as the main goal of developing a diffraction detection method is to position small-scale geological structures as accurately as possible.

6.1.3   Depth of structural discontinuities

The depth of which structural discontinuities are located may influence diffraction detectability. In general, increased subsurface depths lead to increased velocities. In a study by Bashir et al. (2016a), diffraction imaging in a high velocity area is pointed out to be more challenging than in a low velocity area. They discovered that in the case of high depth, the Kirchhoff summation is not summed correctly because of troubles determining which energy that belongs to the diffraction. This discovery will likely also affect the algorithm's ability to detect diffractions. The fault zones studied in this thesis are however positioned at relatively shallow depths, especially within the real seismic data (100 - 500 m depth below the ocean floor), making it difficult to study this effect on our data. However, almost no semblance peak values are observed below a depth of 0.8 km within the seismic section from the Frøya High (Figure 5.13a), despite the presence of fault plane multiples. The lack of detection below this depth is most likely due to the quality of the input data or the associated velocity model rather than the depth of the discontinuities. Nevertheless, the effect of decreasing imaging capabilities with increasing depth on the detection of diffractions should be taken into account if future development of our method is carried out.

6.1.4 Coherent and incoherent noise

The effect of coherent noise (e.g. multiples) was briefly addressed in chapter 5. Diffractions are in fact detected around multiples from overlying discontinuities in the synthetic data from Gullfaks (see Figure 5.7 and Figure 5.8) - despite the fact that a multiple attenuation process was carried out on the seismic input data. This observation illustrates that the presence of coherent noise greatly impacts the results. Consequently, a thorough noise reduction process is recommended in order to reduce the amount of coherent unwanted noise.

The diffraction detection algorithm enables an option of adding random, incoherent noise. If we can demonstrate that diffractions are stable and detectable despite adding a wide range of noise, this would undoubtedly motivate the use of our method. By adding incoherent noise to the seismic input data, we might be able to quantify the robustness of the method against incoherent noise by evaluating its effect on diffraction detection. A signal-to-noise ratio of 10 and 5 is added to the Gullfaks synthetic seismic input data, using image area 1. The results are presented in Figure 6.1 and Figure 6.2. A signal-to-noise ratio of 5 almost completely disguises the seismic reflections in the image area (Figure 6.1c). Figure 6.2 clearly illustrates that, although incoherent noise is added, the method remains robust when it comes to detecting diffractions - as the detected semblance peak values are located in more or less the same positions in all three results (marked with circles in Figure 6.2a, b and c). However, the accuracy of the results is significantly reduced when adding a signal-to-noise ratio of 5.

With an increase of noise, an increase of erroneously detected diffractions is observed (Figure 6.2c). Thus, there is no doubt that the seismic data with the least amount of noise (Figure 6.1a) gives the most accurate result (Figure 6.2a). These tests demonstrate, however, that the diffraction detection algorithm is able to identify diffractions quite accurately, despite including a heavy amount of incoherent noise.
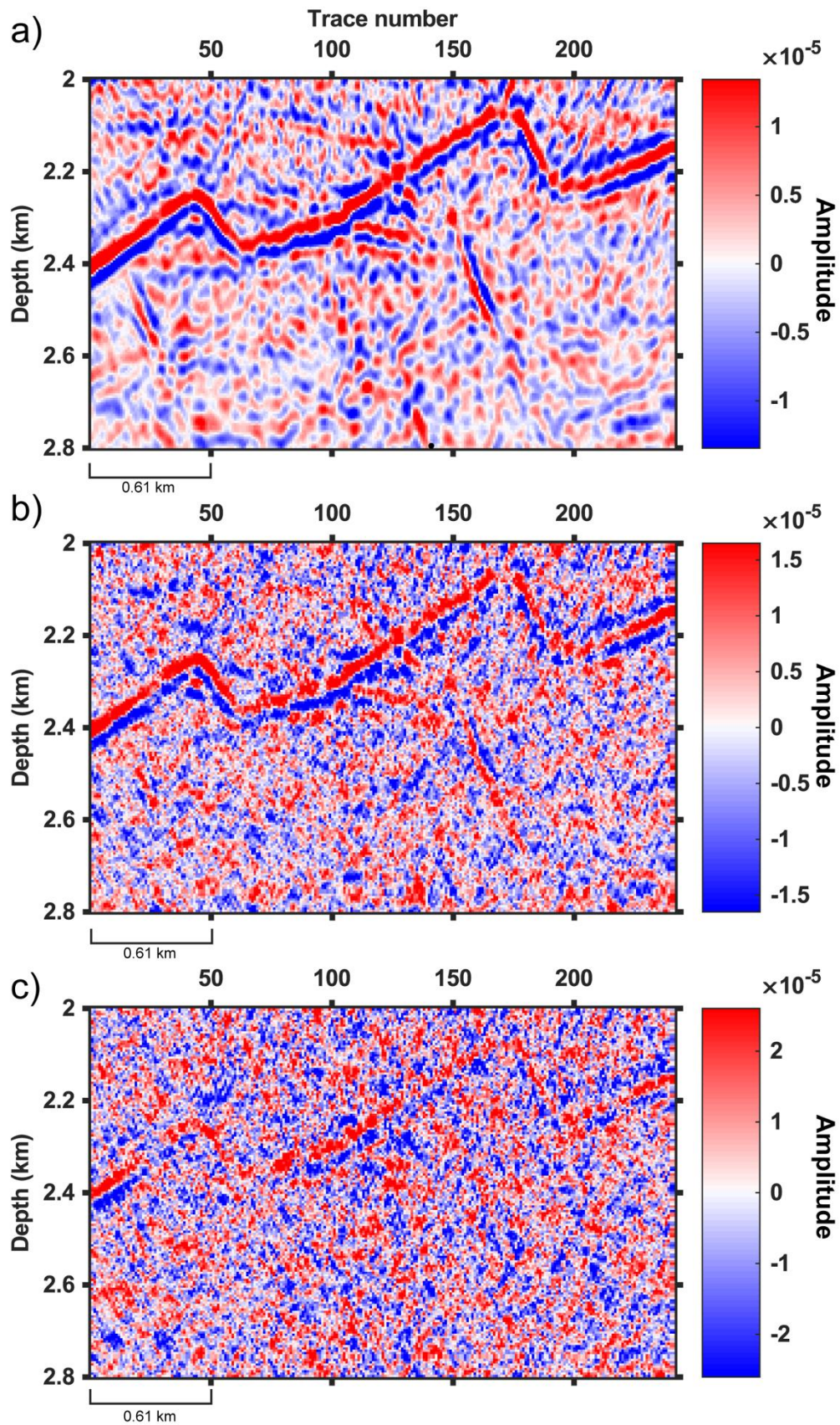
Figure 6.1: Full-wave depth migrated sections obtained from image area 1 (Gullfaks synthetic data) with increasing amounts of added white noise. a) Migrated section prior to adding white noise. b) Migrated section with an added signal-to-noise ratio of 10. c) Migrated section with an added signal-to-noise ratio of 5.
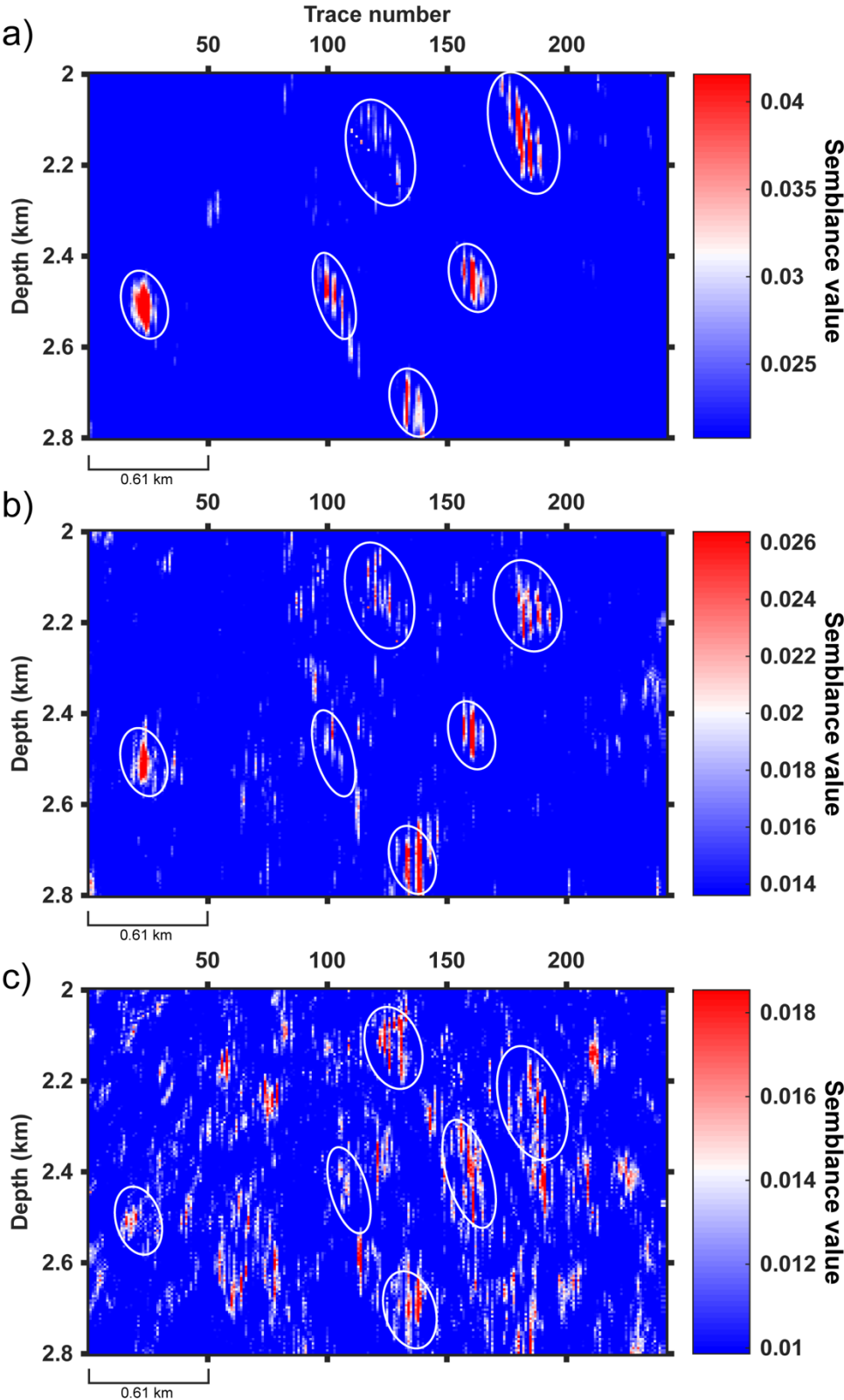
Figure 6.2: Semblance plots generated from image area 1 (Gullfaks synthetic data) illustrating the effect of increased amounts of white noise has on diffraction detectability. A time window corresponding to a dominant frequency of 20 Hz is applied. a) The resulting semblance plot obtained prior to adding noise. b) The resulting semblance plot after adding a signal-to-noise ratio of 10 to the input data. c) The resulting semblance plot after adding a signal-to-noise ratio of 5 to the input data. Circles represent areas with prominent semblance peak values.

6.2 The functionality of the diffraction detection algorithm

From the results presented in the preceding chapter, it seems fair to say that the diffraction detection algorithm does indeed function, however with certain associated uncertainties. Diffracted energy is generally detected in regions where such energy is expected (e.g. around normal faults) and even for the reflected multiples of the target discontinuities. Testing the algorithm on both synthetic and real seismic data seismic also reveal detection of diffractions in unexpected regions, which must be analysed further in order to properly evaluate the functionality of the algorithm.

6.2.1 Gullfaks synthetic seismic data

The results from the diffraction detection at Gullfaks are mostly very accurate. Most semblance peak values are found in expected positions around fault zone regions, including the seismic multiple response of these fault zones. Diffractions that originate from multiples are detected, despite the multiple attenuation process that has been carried out. Reducing the contamination of multiples in seismic data is a major challenge in seismic processing. The fact that we detect diffractions around multiples in a seismic dataset that have previously passed through a multiple attenuation process demonstrate that the deconvolution module has not been successful in removing all signs of multiples. As such, poorer results due to the detection of diffractions in multiples are not caused by the diffraction detection algorithm itself, but rather by the quality of the pre-processing sequence prior to using the algorithm. The pre-processing sequence truly becomes a trade-off between removing coherent unwanted energy, such as multiples, and preserving the energy of diffracted waves. The latter is more important in this thesis. By examining the semblance plots obtained using the synthetic seismic dataset before and after multiple attenuation (see section 5.1.3, Figure 5.6), we see that the detected diffractions are more prominent in the attenuated section. This demonstrates that the multiple attenuation process performed on the synthetic dataset did not significantly suppress the diffracted energy.

In image area 2, there is a substantial increase of unexplained detected diffractions (see Figure 5.8), compared to the results from image area 1. We detect diffractions in all of the three predicted regions (around faults, and multiples of faults), but despite this, the final result is somewhat disturbed by the amount of uninterpretable values in the rest of the plot. This may lead to misinterpretations in further studies. It seems unlikely that these unexplained values

originate from primary reflections of structural discontinuities below the seismic wavelength, as the geological model is known. More likely, the unexplained values are a result of poor noise attenuation, causing the diffraction detection algorithm to erroneously interpret noise as diffracted waves. As discussed and demonstrated in section 6.1.4, we observe that an increase of incoherent noise results in an increase of erroneously detected diffractions. The result of running the diffraction detection on image area 2 could thus potentially benefit from additional noise attenuation (filtering); to see if that reduces the amount of unexplained detected values without compromising the detection of real diffraction events.

6.2.2   Frøya High real seismic data

The quality of the results from the diffraction detection at Frøya High is somewhat uncertain, due to a number of factors. First of all, as we have no other way of identifying small-scale structural discontinuities below the seismic wavelength than by inspecting the diffracted wavefield, a correlation cannot be established in order to clarify if the origin of the unexplained values derive from such small-scale discontinuities or not. In other words, the unexplained values obtained from the diffraction detection algorithm might encode valuable information about the location and geometry small-scale subsurface events below the Rayleigh limit. Secondly, semblance peak values are detected shallower than the depth of the ocean floor, indicating that noise reduction is not sufficiently carried out on the input data, and that the diffraction detection algorithm erroneously detects and extracts certain events and interprets them as diffracted waves. This detection represents a major flaw of the results from the real seismic dataset. However, the erroneous detection is most likely due to the quality of the input data rather than the detection algorithm itself.

As an attempt to test the validity of the results, four prominent semblance peak values (marked with stars in the semblance plot of Figure 5.13) are used in order to simulate traveltime curves. The spatial positions of the four diffraction events are used as shot points, performing wavefront tracing towards receivers positioned on the surface (with an increment of 24 m). The resulting traveltime curves simulate the detected diffraction hyperbolas and are subsequently mapped onto the unmigrated input data in the time-domain. Hopefully, this will allow us to understand the origin of the detected diffractions, as the apex of each traveltime curve should coincide along fault planes or at the edge of any other structural discontinuity. Thus, the simulated diffraction hyperbolas should be tangent to the reflection event that terminate at the diffracting point. It is worth noting that we cannot interpret fault planes in

unmigrated seismic sections in the same way as we can with migrated sections, as the recorded events are placed at their recorded location rather than their correct spatial location.

The results of simulating the diffraction hyperbolas from these four semblance peak values are presented in Figure 6.3 and Figure 6.4. The abrupt intervals of the traveltime curves represent receiver positions with no associated traveltime event. In Figure 6.4b and c, black lines illustrate how the traveltime curves tangents adjacent fault planes.

The simulated diffraction hyperbolas in Figure 6.4b and c seem to perfectly tangent the adjacent fault planes. This indicates that the detected diffractions are the seismic response of these faults. In Figure 6.4, the simulated diffraction hyperbola is observed near a prominent normal fault, but does not tangent the terminating reflections in this region. The structural source of this detected diffraction is thus uncertain. However, the fact that the apexes of the hyperbolas are not placed directly at the fault plane does not necessarily indicate that the spatial positions of the detected diffractions are incorrect, as the true subsurface positions of faults are generally unknown. No apparent discontinuity is observed in relation to the simulated diffraction hyperbola of Figure 6.4 d. A minor fault (marked with circle in Figure 6.4d) is however observed approximately 200 ms (TWT) shallower than the apex of the simulated diffraction hyperbola, but the fault plane does not extend down to the detected semblance peak value. Consequently, the associated diffraction event either reflects an incorrectly detected diffraction value or a structural discontinuity below the seismic wavelength. Determining the origin of this diffraction event is beyond the scope of this thesis - but is however possible. If the detected diffractions are explicitly used to estimate the velocity model, seismic resolution has potential for improvement and might lead to the identification of small-scale discontinuities. This would make it possible to determine whether the unexplained diffraction events originate from small-scale discontinuities or noise.

Conclusively, despite a semblance plot (Figure 5.13a) that seems hard to interpret, we are able to pick selected semblance peak values for further inspection in order to prove that the algorithm also functions with the real seismic dataset and that it delivers reliable results. Surely, the amount of uncertainties is expected to be greater when dealing with a real seismic dataset compared to a synthetic one, but the detected results definitely indicate that the method has potential. Further development in order to decrease the amount of unexplained semblance peak values is however recommended.
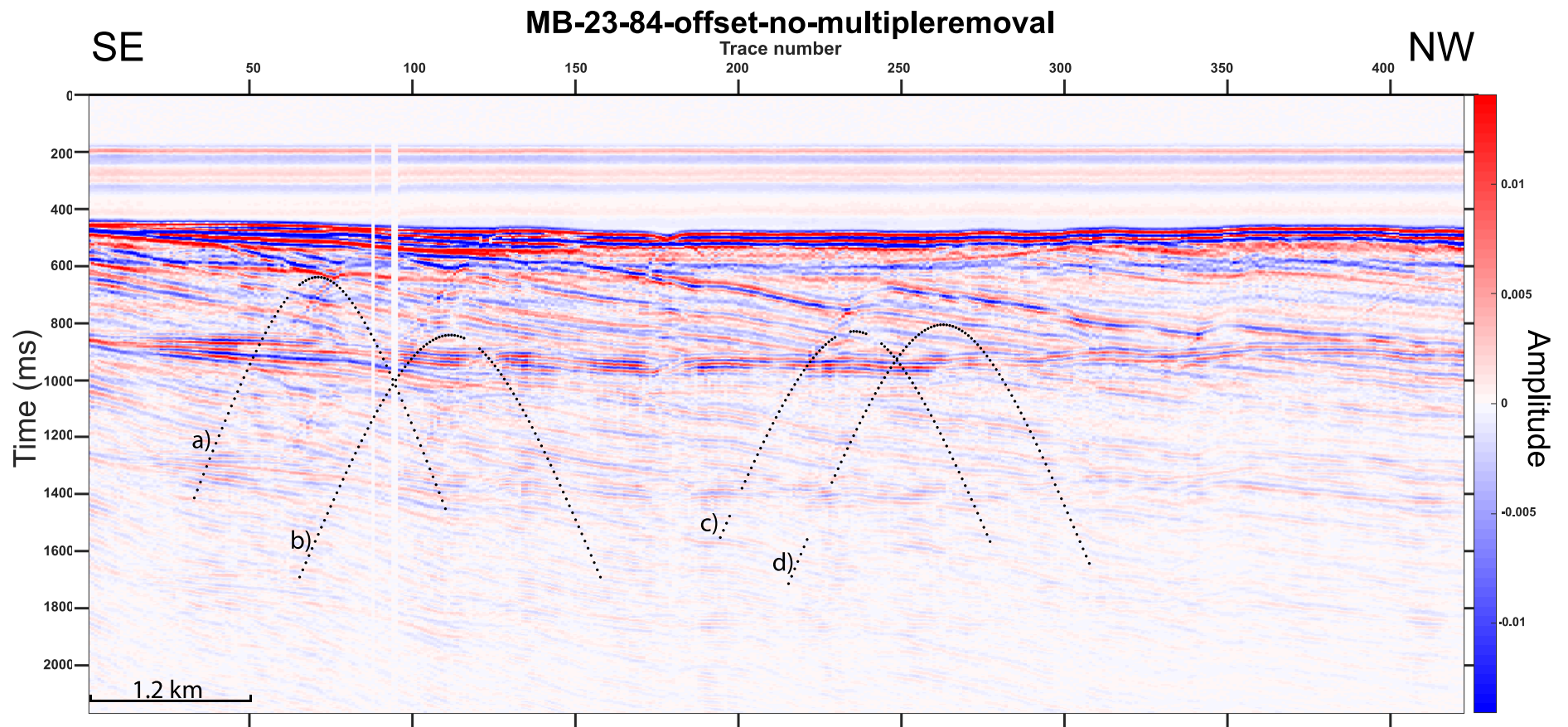
Figure 6.3: Simulated traveltime curves, marked a)-d), from detected diffractions mapped on the real seismic offset section in the time-domain. The abrupt intervals of the traveltime curves represent receiver positions with no associated traveltime event. Each simulated curve is respectively presented in Figure 6.4.
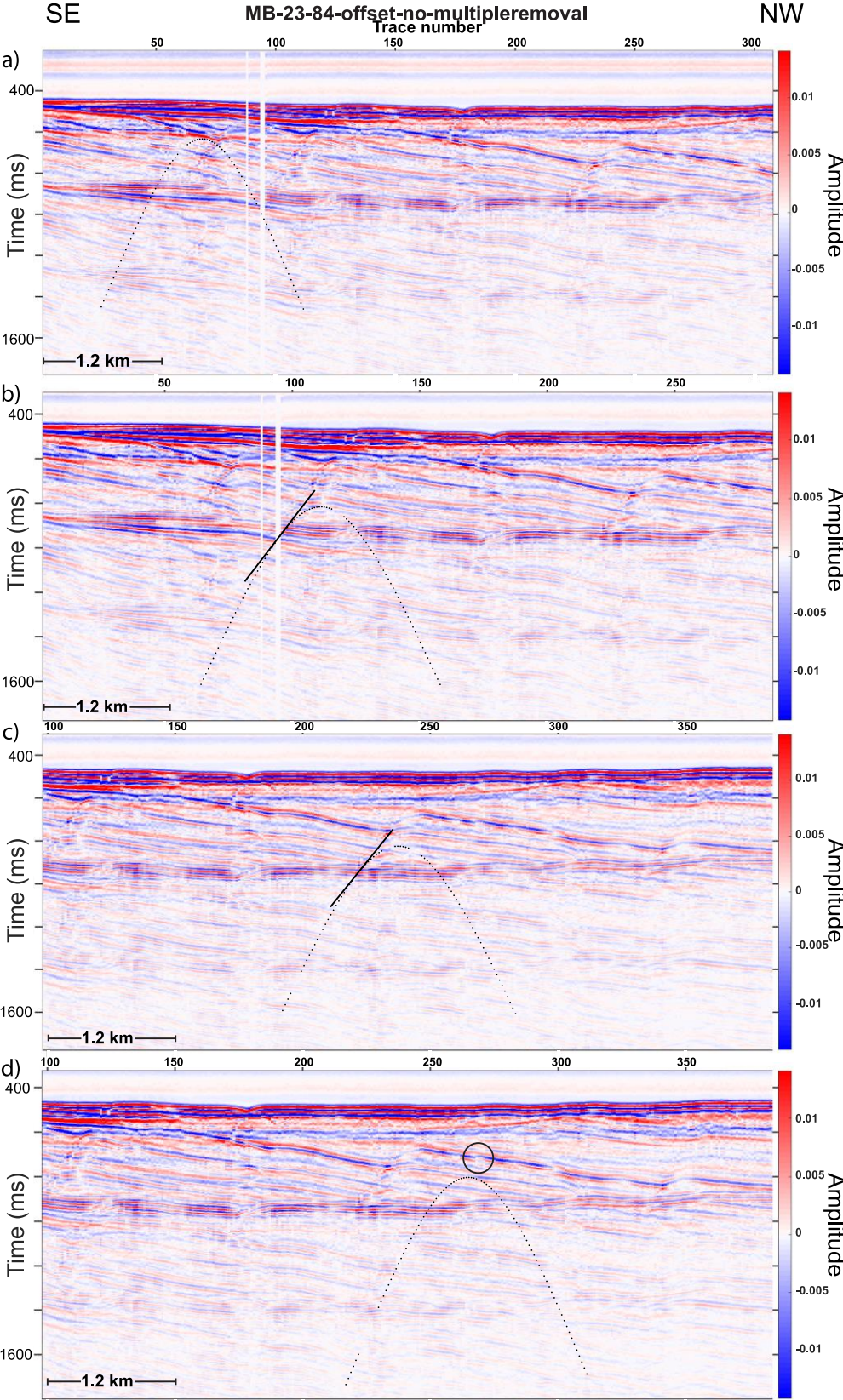
Figure 6.4: Simulated traveltime curves from 4 individually detected diffractions, marked a-d), on top of the real seismic offset section in the time-domain. Black lines in b) and c) illustrate how the traveltime curves perfectly tangents the adjacent fault planes. The circle marked in d) represents a minor fault.

6.2.3   Summary

The diffraction detection algorithm successfully detects diffractions using both synthetic and real seismic data, despite some occurrences of unexplained values. It is likely that further reduction of coherent noise (e.g. multiples) executed during the pre-processing sequence will improve our results. The impact of incoherent noise on the algorithm is also evaluated by performing a test on the synthetic dataset. Despite an increasing amount of incoherent noise, the method is proven robust in detecting diffraction events.

One of the major issues with the method in this study is that only two datasets with relatively similar fault structures were used when testing the method. Ideally, we would use datasets containing different structural discontinuities for testing the methods, but this proved to be difficult due to the availability of pre-stack data in the DISKOS database. Thus, there is a chance that the detection algorithm could encounter new challenges that have not been considered when testing the algorithm on datasets from other geological settings. In order to implement the diffraction detection algorithm on a wider range of structures (e.g. pinch-outs, karsts and fractures), modifications might be required. Future success cannot be guaranteed prior to testing the method on other structural features.

Several attempts have been made to detect diffractions, using various methods to separate diffractions from the reflected wavefield (e.g. Landa et al., 1987; Landa & Keydar, 1998; Khaidukov et al., 2004; Fomel et al., 2007; Moser & Howard, 2008; Berkovitch et al., 2009; Lin et al., 2018). This study implements the reflection focusing method, proposed by Khaidukov et al. (2004), together with a semblance calculation process. Semblance is within the course of this study proven to quantitatively measure the algorithm's diffraction detection capability, as high semblance peak values indicate detected diffraction points.

In the study by Khaidukov et al. (2004), it is discussed that if the velocity model accurately focuses diffractions to diffraction points, the velocity model should also be capable of focusing reflections to imaginary reflection source points. As the algorithm successfully detects diffractions on both synthetic and real seismic data, it is reasonable to claim that we are able to separate diffractions from spatial reflections by using the reflection focusing method. This finding supports the results obtained by Moser and Howard (2008), and the theory proposed by Khaidukov et al. (2004). The effect of velocity smoothing and velocity

errors on diffraction detection is analysed and discussed. Both factors are more likely to affect the spatial positioning of the detected diffractions rather than the capability of detecting them.

Despite some uncertainties, the results obtained from testing the method on synthetic and real seismic data are promising and indicates that the method has potential. Further development of the diffraction detection algorithm is thus highly recommended.

7 Conclusions

The main objective of this thesis has been to develop and investigate the potential of a procedure for detecting and verifying diffraction events in recorded seismic data. By testing the diffraction detection procedure on both synthetic and real seismic data, it was concluded:

· Semblance is successfully used as a quantitative measure of diffraction detection capability. Reflection focusing as a method for separating diffractions from specular reflections is proven effective.

· Diffractions were to great extent accurately detected for the Gullfaks synthetic dataset, where most semblance peak values were found in expected positions around fault zone regions, including the seismic multiple response of these fault zones. Some detections are made in unexpected regions, but these findings are most likely due to poor noise attenuation.

· The geological setting is more complex in the section from the Frøya High compared to in the synthetic dataset. The results from the real seismic data are thus far less accurate than the results from Gullfaks. However, diffractions are detected in most prominent fault zones, but a significant amount of unexplained diffraction events are detected. To improve these results, further attenuation of coherent noise and a quality assessment of the velocity model provided with the seismic data from the Frøya High is recommended.

· The diffraction detection algorithm is sensitive to velocity errors when it comes to positioning the diffracted energy to its true subsurface position. However, it seems that velocity errors will to little extent affect the algorithm's ability to detect diffractions. Thus, there is no reason to believe that the velocity smoothing performed in NORSAR-3D will affect diffraction detectability, other than the fact that it might result in a depth shift. An accurate velocity model is however of considerable importance as the main goal of developing a diffraction detection method is to position small-scale geological structures as accurately as possible.

- Coherent noise and unwanted coherent events, in particular multiple energy, has a significant impact on diffraction detection. In this study, diffractions have been detected in multiples originating from overlying primary reflections of structural discontinuities. As a result, a systematic noise attenuation process is recommended during the pre-processing sequence of the seismic input data.

- By testing the algorithm with increasing amounts of incoherent white noise, we observe that the algorithm still manages to detect diffractions, and this quite successfully.

- To test the validity of the results obtained from the diffraction detection algorithm, diffraction hyperbolas can be simulated using wavefront tracing on the velocity models in depth. The spatial positions of the detected diffractions are used as shot points, and receivers are positioned close to the surface. The resulting traveltime curves can be superimposed on seismic input data in the time-domain in order to interpret and evaluate the validity of the detected semblance peak values.

- The diffraction detection algorithm shows great potential for further research. Several issues remain to be investigated, but the experiences gained with developing and testing of the diffraction detection algorithm suggests that the approach is worth further development.

8   Future work

Based on the results and experiences obtained from this study, these are my recommendations for further work:

- Test the diffraction detection algorithm on seismic sections, both synthetic and real, that includes a larger range of different geological small-scale scattering objects. In this study, testing was limited to image areas with identified normal faults. Possible future study areas include, but are not limited to, fractures, karsts, pinch-outs, reverse- and strike slip faults. As diffractions have the potential of identifying faults and fractures with zero displacements, it would be interesting to take into account such features in the diffraction detection algorithm.

- Traditional time-domain velocity models created using specular reflections are not suitable for diffraction imaging. However, the detected diffractions from this study can be used in order to accurately pick velocities for diffractions. The next step could thus be to develop an optimal velocity model suitable for diffraction imaging.

- In general, increased subsurface depths lead to increased velocities. Diffraction hyperbolas flattens out as an effect of increasing velocities (Bashir et al., 2016a). This effect has not been thoroughly investigated in this study. Further work could include testing the diffraction detection algorithm on structural discontinuities within a variety of depths in order to determine the algorithm's detectability vs. depth.

- If the above steps prove success of the diffraction detection method using 2D seismic data, a possible step forward could be to modify the algorithm in order to function with 3D seismic data.

References

Agustsson, H., Stroenen, L. K., & Solheim, O. A. (1999). *The Gullfaks Field: Creating Value by means of a Multidisciplinary Reservoir Management Approach*. Paper presented at the Offshore Technology Conference, Houston, Texas, 3-6 May 1999.

Bacon, M., Simm, R., & Redshaw, T. (2003). *3-D seismic interpretation*. Cambridge: Cambridge University Press.

Bansal, R., & Imhof, M. G. (2005). Diffraction enhancement in prestack seismic data. *Geophysics, 70*(3), V73-V79.

Bashir, Y., Ghosh, D. P., Moussavi Alashloo, S. Y., Sum, C. W., & Gaol, F. L. (2016a). Effect of frequency and migration aperture on seismic diffraction imaging. *IOP Conference Series. Earth and Environmental Science, 30*(1).

Bashir, Y., Ghosh, D. P., Moussavi Alashloo, S. Y., Sum, C. W., & Gaol, F. L. (2016b). Enhancement in seismic imaging using diffraction studies and hybrid traveltime technique for PSDM. *IOP Conference Series. Earth and Environmental Science, 38*(1).

Bashir, Y., Ghosh, D. P., & Sum, C. W. (2015). *Detection of Fault and Fracture using Seismic Diffraction and Behavior of Diffraction Hyperbola with Velocity and Time*. Paper presented at the EAGE Seismic Driven Reservoir Characterization and Production Management Symposium, Kuala Lumpur, Malaysia, 20-22 April 2015.

Belfer, I., Bruner, I., Keydar, S., Kravtsov, A., & Landa, E. (1998). Detection of shallow objects using refracted and diffracted seismic waves. *Journal of Applied Geophysics, 38*(3), 155-168.

Berkovitch, A., Belfer, I., Hassin, Y., & Landa, E. (2009). Diffraction imaging by multifocusing. *Geophysics, 74*(6), WCA75-WCA81.

Blystad, P., Brekke, H., Færseth, R. B., Larsen, B. T., Skogseid, J., & Tørudbakken, B. (1995). Structural elements of the Norwegian continental shelf. Part II: The Norwegian Sea Region. *The Norwegian Petroleum Directorate, NPD-BULLETIN No.8.*

Brekke, H. (2000). The tectonic evolution of the Norwegian Sea Continental Margin with emphasis on the Vøring and Møre Basins. *Geological Society London Special Publications, 167*, 327-378.

Brekke, H., Larsen, B. T., Skogseid, J., Blystad, P., Færseth, R. B., & Tørudbakken, B. (1995). *Structural elements of the Norwegian continental shelf*. Unpublished illustration (provided by Harald Brekke). The Norwegian Petroleum Directorate.

Brekke, H., Sjulstad, H. I., Magnus, C., & Williams, R. W. (2001). Sedimentary environments offshore norway — an overview. *Norwegian Petroleum Society Special Publications, 10*, 7-37.

References

Braathen, A., Nordgulen, O., & Andersen, T. (2000). Devonian, orogen-parallel, opposed extension in the Central Norwegian Caledonides. *Geology, 28*(7), 615-618.

Braathen, A., Osmundsen, P., Nordgulen, O., Roberts, D., & Meyer, G. B. (2002). Orogen-parallel extension of the Caledonides in northern Central Norway: an overview. *Norwegian Journal of Geology, 82*(4), 225-241.

Bukovics, C., & Ziegler, P. A. (1985). Tectonic development of the Mid-Norway continental margin. *Marine and Petroleum Geology, 2*(1), 2-22.

CGGVeritas. (2008). Geocluster 5.0 User's Manual.

Decker, L., & Klokov, A. (2014). *Diffraction extraction by plane-wave destruction of partial images*. Paper presented at the 84th Annual International Meeting. Society of Exploration Geophysicists, Expanded Abstracts, 3862-3867.

Decker, L., Merzlikin, D., & Fomel, S. (2017). *Enhancing seismic-diffraction images using semblance-weighted least-squares migration*. Paper presented at the 87th Annual International Meeting. Society of Exploration Geophysicists, Expanded Abstracts, 5294-5299.

Doré, A. G., Lundin, E. R., Fichler, C., & Olesen, O. (1997). Patterns of basement structure and reactivation along the NE Atlantic margin. *Journal of the Geological Society, 154*, 85-92.

Doré, A. G., Lundin, E. R., Jensen, L. N., Birkeland, O., Eliassen, P. E., Fichler, C., Fleet, A. J., & Boldy, S. A. R. (1999). Principal tectonic events in the evolution of the Northwest European Atlantic margin. *Petroleum Geology Conference series, 5*, 41-61.

Evans, B. J. (1997). *A Handbook for Seismic Data Acquisition in Exploration*. Geophysical Monograph Series, no. 7. Tulsa, Oklahoma: Society of Exploration Geophysicists.

Faleide, J. I., Bjørlykke, K., & Gabrielsen, R. H. (2010). Geology of the Norwegian Continental shelf. In Bjørlykke, K. (Ed.), *Petroleum Geoscience : From Sedimentary Environments to Rock Physics* (2nd ed., 467-499). Berlin, Heidelberg: Springer Berlin Heidelberg.

Faleide, J. I., Tsikalas, F., Breivik, A. J., Mjelde, R., Ritzmann, O., Engen, O., Wilson, J., & Eldholm, O. (2008). Structure and evolution of the continental margin off Norway and Barents Sea. *Episodes, 31*(1), 82-91.

Fomel, S. (2002). Applications of Plane-Wave Desctructor Filters. *Geophysics, 67*(6), 1692-2041.

Fomel, S. (2009). Velocity analysis using AB semblance. *Geophysical Prospecting, 57(3)*, 311-321.

Fomel, S., Landa, E., & Taner, M. T. (2007). Poststack velocity analysis by separation and imaging of seismic diffractions. *Geophysics, 72*(6), U89-U94.

References

Fossen, H., & Hesthammer, J. (1998). Structural geology of the Gullfaks Field, northern North Sea. In Coward, M. P. et al. (Eds.), *Structural Geology in Reservoir Characterization* (Vol. 127, 231-261). London: Geological Society Special Publications.

Fossen, H., & Rørnes, A. (1996). Properties of fault populations in the Gullfaks Field, northern North Sea. *Journal of Structural Geology, 18*(2), 179-190.

Gabrielsen, R. H., Færseth, R. B., Hamar, G. P., & Rønnevik, H. (1984). Nomenclature of the main structural features on the Norwegian Continental Shelf north of the 62nd parallel. In Spencer, A. M. et al. (Eds.), *Petroleum Geology of the North European Margin* (41-60). London: Graham and Trotman.

Gabrielsen, R. H., Odinsen, T., & Grunnaleite, I. (1999). Structuring of the Northern Viking Graben and the More Basin; the influence of basement structural grain, and the particular role of the More-Trondelag Fault Complex. *Marine and Petroleum Geology, 16*(5), 443-465.

Hagedoorn, J. G. (1954). A process of seismic reflection interpretation. *Geophysical Prospecting, 2*(2), 85-127.

Halland, E. K., Johansen, W. T., & Riis, F. (2014). CO2 Storage Atlas Norwegian Continental Shelf. *The Norwegian Petroleum Directorate*.

Harlan, W. S., Claerbout, J. F., & Rocca, F. (1984). Signal/noise separation and velocity estimation. *Geophysics, 49*(11), 1869-1880.

Iacopini, D., Butler, R. W. H., Purves, S., McArdle, N., & De Freslon, N. (2016). Exploring the seismic expression of fault zones in 3D seismic volumes. *Journal of Structural Geology, 89*, 54-73.

Jones, I. F. (2014). Estimating subsurface parameter fields for seismic migration: Velocity model building. In Grechka, V. & Wapenaar, K. (Eds.), *Encyclopedia of Exploration Geophysics*: Society of Exploration Geophysicists.

Kearey, P., Brooks, M., & Hill, I. (2002). *An introduction to geophysical exploration* (3rd ed.). Oxford: Blackwell Science.

Khaidukov, V., Landa, E., & Moser, T. J. (2004). Diffraction imaging by focusing-defocusing: An outlook on seismic superresolution. *Geophysics, 69*(6), 1478-1490.

Klokov, A., Fomel, S., & Klokov, A. (2012). Separation and imaging of seismic diffractions using migrated dip-angle gathers. *Geophysics, 77*(6), 131-143.

Krey, T. (1952). The significance of diffraction in the investigation of faults. *Geophysics, 17*(4), 843-858.

Kumar, D., & Ahmed, I. (2011). Seismic Noise. In Gupta, H. K. (Ed.), *Encyclopedia of Solid Earth Geophysics (Encyclopedia of Earth Sciences Series)*. Dordrecht: Springer.

Kunz, B. F. J. (1960). Diffraction Problems in Fault Interpretation. *Geophysical Prospecting, 8*(3), 381-388.

References
_____

Landa, E. (2012). *Seismic diffraction: where's the value?* Paper presented at the 82nd Annual International Meeting. Society of Exploration Geophysicists, Expanded Abstracts, 1-4.

Landa, E., Fomel, S., & Reshef, M. (2008). *Separation, imaging, and velocity analysis of seismic diffractions using migrated dip-angle gathers*. Paper presented at the 78th Annual International Meeting, Society of Exploration Geophysicists, Expanded Abstracts, 2176-2180.

Landa, E., & Keydar, S. (1998). Seismic monitoring of diffraction images for detection of local heterogeneities. *Geophysics, 63*(3), 1093-1100.

Landa, E., Shtivelman, V., & Gelchinsky, B. (1987). A method for detection of diffracted waves on common-offset sections. *Geophysical Prospecting, 35*(4), 359-373.

Lin, P., Peng, S., Zhao, J., Cui, X., & Du, W. (2018). Accurate diffraction imaging for detecting small-scale geologic discontinuities. *Geophysics, 83*(5), 447-457.

Lines, L. R., & Newrick, R. T. (2004). *Fundamentals of geophysical interpretation*. Geophysical Monograph Series, no. 13. Tulsa, Oklahoma: Society of Exploration Geophysicists.

Marsh, N., Imber, J., Holdsworth, R. E., Brockbank, P., & Ringrose, P. (2010). The structural evolution of the Halten Terrace, offshore Mid- Norway: extensional fault growth and strain localisation in a multi- layer brittle–ductile system. *Basin Research, 22*(2), 195-214.

Mondol, N. H. (2010). Seismic Exploration. In Bjørlykke, K. (Ed.), *Petroleum Geoscience: From Sedimentary Environments to Rock Physics* (375-402). Berlin, Heidelberg: Springer Berlin Heidelberg.

Moser, T. J., & Howard, C. B. (2008). Diffraction imaging in depth. *Geophysical Prospecting, 56*, 627-641.

Mousa, W., & Al-Shuhail, A. A. (2011). *Processing of seismic reflection data using MATLAB TM* (Vol. 10). San Rafael, California: Morgan & Claypool.

Mussett, A. E., & Khan, M. A. (2000). *Looking into the earth : an introduction to geological geophysics*. Cambridge: Cambridge University Press.

Nadin, P. A., & Kusznir, N. J. (1995). Palaeocene uplift and Eocene subsidence in the northern North Sea Basin from 2D forward and reverse stratigraphic modelling. *Journal of the Geological Society, 152*(5), 833-848.

NORSAR. (2012). NORSAR-3D User's Guide (Version 5.5).

Ogiesoba, O., & Klokov, A. (2016). *Seismic diffraction imaging of lithology in fault zones and hydrocarbon sweet spots within the Maverick Basin, South Texas*. Paper presented at the Unconventional Resources Technology Conference (URTeC), San Antonio, Texas, USA, 1-3 August 2016.

Onajite, E. (2014). Understanding Noise in Seismic Record. In Onajite, E. (Ed.), *Seismic Data Analysis Techniques in Hydrocarbon Exploration* (63-68). Oxford: Elsevier.

References

Petterson, O., Storli, A., Ljosland, E., & Massie, I. (1990). The Gullfaks Field: Geology and Reservoir Development. In Buller, A. T. et al. (Eds.), *North Sea oil and gas reservoirs - II : proceedings of the 2nd North Sea Oil and Gas Reservoirs* (67-90). Dordrecht: Springer.

Pitman, W., & Talwani, M. (1972). Sea-Floor Spreading in the North Atlantic. *Bulletin of the Geological Society of America, 83*(3), 619-646.

Pon, S., & Lines, L. (2005). Sensitivity analysis of seismic depth migrations. *Geophysics, 70*(2), S39-S42.

Ramberg, I. B., Bryhni, I., Nøttvedt, A., & Norsk geologisk forening. (2013). *Landet blir til : Norges geologi* (2 ed.). Trondheim: Norsk geologisk forening.

Sheriff, R. E., & Geldart, L. P. (1995). *Exploration seismology* (2nd ed.). Cambridge: Cambridge University Press.

Skilbrei, J., Olesen, O., Osmundsen, P., Kihle, O., Aaro, S., & Fjellanger, E. (2002). A study of basement structures and onshore-offshore correlations in Central Norway. *Norwegian Journal of Geology, 82*(4), 263-279.

Surlyk, F. (1990). Timing, style and sedimentary evolution of Late Palaeozoic-Mesozoic extensional basins of East Greenland. *Geological Society London Special Publications, 55*(1), 107-125.

Taner, M. T., Fomel, S., & Landa, E. (2006). *Separation and imaging of seismic diffractions using plane-wave decomposition*. Paper presented at the 76th Annual International Meeting. Society of Exploration Geophysicists, Expanded Abstracts, 2401-2405.

Taner, M. T., & Koehler, F. (1969). Velocity spectra-digital computer derivation and applications of velocity functions. *Geophysics, 34*(6), 859-881.

Telford, W. M., Geldart, L. P., & Sheriff, R. E. (1990). *Applied geophysics* (2nd ed.). Cambridge: Cambridge University Press.

Vinje, V., Iversen, E., & Gjoystdal, H. (1993). Travel-Time and amplitude estimation using wave-front construction. *Geophysics, 58*(8), 1157-1166.

Vinje, V., Stovas, A., & Reynaud, D. (2013). Preserved- traveltime smoothing. *Geophysical Prospecting, 61*, 380-390.

Yilmaz, Ö. (2001). *Seismic data analysis : processing, inversion, and interpretation of seismic data* (2nd ed. Vol. 1 & 2). Tulsa, Oklahoma: Society of Exploration Geophysicists.

Zhu, J., Lines, L., & Gray, S. (1998). Smiles and frowns in migration/velocity analysis. *Geophysics, 63*(4), 1200-1209.

Ziegler, P. A. (1989). *Evolution of Laurussia: A study in Late Palaeozoic plate tectonics*. Dordrecht: Kluwer Academic Publishers.

Electronic references

Mjelde, R. (2011). Seismic Processing. Retrieved from http://buster.geo.uib.no/emodules/ [Accessed: 12.02.2019]